



F3

**Faculty of Electrical Engineering
Department of Radioelectronics**

Ph.D. Thesis

Radio Detection of Electromagnetic Phenomena in the Atmosphere

**Integrating Advanced Instrumentation and UAVs for
Enhanced Atmospheric Research**

Jakub Kákona

**P2612 - Electrical Engineering and Information Technology
3708V017 - Air Traffic Control**

June 2024

**Supervisor: doc. Dr. Ing. Pavel Kovář
Consultant: doc. Ing. Jan Mikeš, Ph.D.**

Draft: 27. 6. 2024

/ Declaration

Prohlašuji, že jsem předloženou práci vypracoval samostatně a že jsem uvedl veškeré použité informační zdroje v souladu s Metodickým pokynem o dodržování etických principů při přípravě vysokoškolských závěrečných prací.

V Praze dne 26. 6. 2024

.....

Abstrakt / Abstract

Tato disertační práce se zaměřuje na využití rádiové detekce pro zkoumání elektromagnetických jevů v atmosféře. Hlavní pozornost je věnována integraci nových meteorologických přístrojů, rádiových přijímačů, telemetrických systémů a bezpilotních prostředků (UAV) do výzkumu atmosférických jevů. Práce přináší detailní analýzu atmosférických dat získaných prostřednictvím leteckých a pozemních měření. Jejich přímé využití je potom nasměrováno k hlubšímu pochopení dynamiky bouří a atmosférických elektromagnetických událostí. Popisované experimenty demonstруjí, jak aplikace pokročilých měřicích technologií může zlepšit pochopení specifických atmosférických jevů.

Překlad titulu: Rádiová detekce elektromagnetických jevů v atmosféře (Implementace pokročilé instrumentace a bezpilotních prostředků pro atmosférický výzkum)

This dissertation explores the use of radio detection for studying electromagnetic phenomena in the atmosphere, focusing on the development and integration of advanced radio receivers, meteorological instruments, mobile measurement platforms, telemetry systems, and unmanned aerial vehicles (UAVs). It presents a comprehensive approach to capturing and analyzing atmospheric data, offering insights into the complex dynamics of storms and electromagnetic events. Through a series of experiments, including atmospheric flights and ground-based measurements, the research demonstrates the potential of novel technologies to enhance the understanding of atmospheric processes, contributing significantly to the field of atmospheric sciences.

Contents /

1 Introduction	5
1.1 Scope of the thesis	5
1.2 Problem Statement	5
1.3 Key radio signatures of lightning events	7
1.3.1 K-changes	7
1.3.2 Narrow Bipolar Events (NBEs)	7
1.3.3 Sferics	7
1.4 Literature Review and state-of-the-art	8
1.4.1 Summary of Initial Assumptions	8
1.5 Contributions	9
1.6 Outline of the thesis	11
2 Lightning triggered recording	13
2.1 Off-the-shelf lightning detection	14
2.2 Blitzortung network	17
2.3 Comparison of different triggering methods	17
2.4 Additional investigation of triggering methods	23
2.4.1 Using the oscilloscope to generate a recording trigger	23
2.4.2 Manual trigger method	25
3 Proposed Instrumentation	27
3.1 High-speed all-sky Cameras	28
3.2 Radiofrequency receivers	29
3.2.1 Recording trigger implementation	29
3.2.2 VLF signal receiver	31
3.2.3 UHF signal receiver	32
3.3 Ionizing radiation detectors	37
3.4 Electric Field Sensors	38
3.5 Meteorological instruments	41
3.5.1 Disdrometer	41
3.5.2 Anemometer	44
3.5.3 Thermometer and Barometer	45
4 Subsequent Experiments	47
4.1 Stratospheric Balloon Flights	47
4.1.1 The design of universal avionics	49
4.1.2 Instrument payload	50
4.1.3 Atmospheric phenomena Detectors	50
4.1.4 Results from the balloon flights	51
4.1.5 Outcome of stratospheric balloon flights	55
4.2 Autogyro Thunderstorm Flights	56
4.2.1 Autogyro airframe	57
4.2.2 Airspeed sensing	58
4.2.3 Telemetry system	60
4.2.4 Carried sensors	61
4.2.5 Takeoff technique	62
4.2.6 Test flights	65
4.3 Ground level measurements	66
4.3.1 Measuring Cars Infrastructure	67
4.3.2 Data capturing procedure	72
4.3.3 Ionizing radiation measurements	72
4.3.4 Visual Camera measurements	74
4.3.5 Radio signal measurements	76
4.3.6 Correlation of measured lightning with lightning detection network	77
4.3.7 Electric field measurements	78
5 Summary of results	80
5.1 Lightning duration	80
5.2 Lightning development/characterization	82
5.3 Conclusions	84
5.4 Future Work	85
A Index	87
B Dictionary	88
C FIK Flights Overview	89
References	91

Tables / Figures

2.1 Table of coincidence rates among detectors	20
2.2 AS3935 based detector PCB design	15
2.3 AS3935 based detector schematics diagram	16
2.4 AS3935 based detector block diagram	16
2.5 Lightning detection testing situation map.....	18
2.6 Comparison of Blitzortung.org with LIGHTNING01A.....	19
2.7 Map of detection coincidences between Blitzortung.org and LIGHTNING01..	21
2.8 Isofix mount of the triggering oscilloscope in the CAR1	23
2.9 STP based loop antenna prototype.....	25
2.10 Manual triggering button mounted on manual gear lever .	26
3.1 Measuring CAR0 with instruments mounted on the roof platform	27
3.2 High-speed all-sky camera	28
3.3 Lightning signal receiver's control software	30
3.4 VLF antenna array construction	31
3.5 An example of VLF lightning signal	32
3.6 UHF lightning signal receiver and its components	33
3.7 Block schematics of the UHF active antenna front-end	34
3.8 QFH antenna radiation pattern	35
3.9 UHF receiver RF filters	35
3.10 Active antenna analog front-end PCB.....	36
3.11 Example of the pulse from scintillator detector	38
3.12 EFM mounted on the CR-REAT car's roof.....	39
3.13 THUNDERMILL01 mounted on Lomnický Štít observatory	40

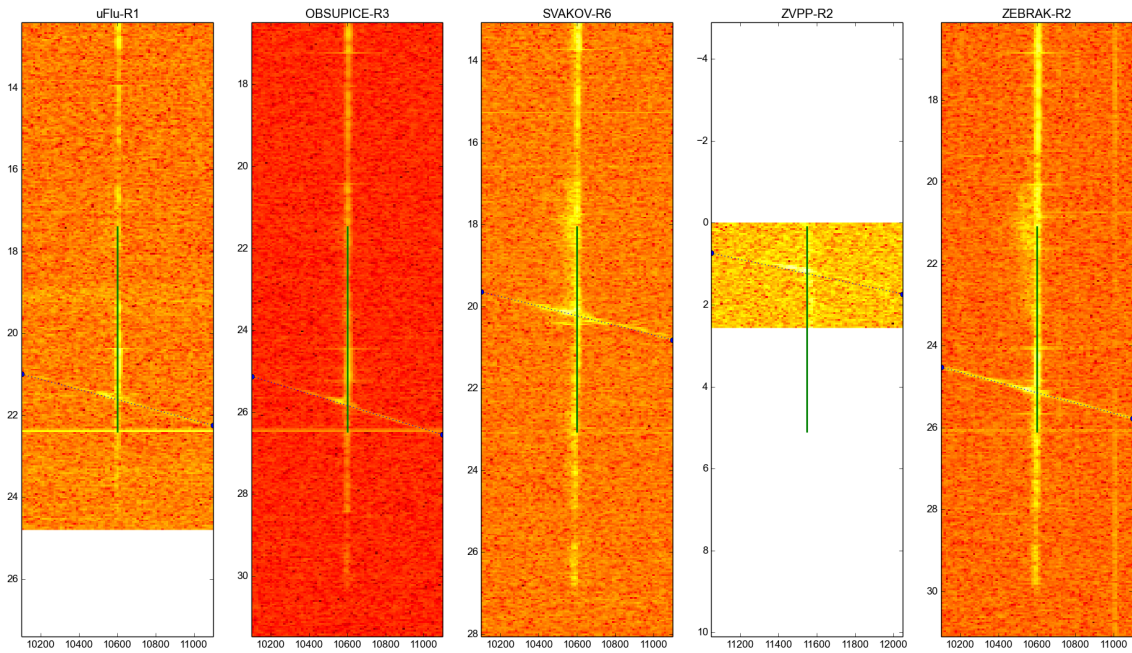
3.14	Comparison of Boltek and THUNDERMILL01	41
3.15	Radon progeny washout	41
3.16	Example of tipping bucket rain-gauge data.....	42
3.17	DISDROMETER01 internals ..	43
3.18	Hail and raindrop captured by DISDROMETER01.....	43
3.19	WINDGAUGE03 anemometer mounted on the car roof ...	44
3.20	Example of data measured by the designed anemometer ..	45
3.21	Example graph of temperature and pressure evolution during thunderstorm	46
4.1	FIK flight avionics	49
4.2	FIK-6 flight balloon setup	51
4.3	FIK-6 flight recorded data	53
4.4	Acceleration and Angular Speed balloon telemetry	53
4.5	Gondola recovery, based on trajectory prediction	54
4.6	Estimated Regener-Pfotzer maxima	55
4.7	Takeoff of the stratospheric balloon during high wind conditions.....	56
4.8	TF-G2 during flight	57
4.9	TF-G2 without rain cover	58
4.10	TFSLOT01 airspeed sensor design	60
4.11	TFSIK dual-antenna telemetry modem.....	61
4.12	EFM mounted on autogyro's rotor head	62
4.13	Example of data measured by EFM mounted on autogyro	62
4.14	UAV control panel	64
4.15	Autogyro takeoff platform	65
4.16	Lift and Drag measurement platform	66
4.17	CRREAT CAR0 instrumentation diagram	68
4.18	CRREAT CAR1 instrumentation diagram	69

4.19	CRREAT CAR2 instrumentation diagram	70
4.20	RTK antennas mounted on a vehicle	71
4.21	Ionizing radiation flux compared to registered lightning...	73
4.22	Individual registered particles of ionizing radiation of gamma spectrometer.....	74
4.23	A still image example from the all-sky camera.....	75
4.24	An example of luminosity curves	76
4.25	Example of VLF signal with the comparison to camera data	77
4.26	Correlation with less than 20 km lightning detections	78
4.27	Correlation with more than 20 km lightning detections.....	78
4.28	Example of EFM measurement	79
4.29	Comparison of EFM data with camera data in detail.....	79
5.1	Camera lightning events duration	81
5.2	UHF lightning events duration	81
5.3	Histogram of durations of observed lightning events	81
5.4	Lightning map based on VLF data	83

1 Foreword

I chose to write a relatively wide introduction to help explain the necessary context for understanding some of the trade-offs made throughout this work. I believe this approach will allow readers to grasp the broad spectrum of activities that, without explanation, might seem unrelated. At the beginning of my research, I focused on the Bolidozor network. Bolidozor is a forward-scattering radio meteor detection network that non-cooperatively uses signals from the French military radar GRAVES¹. This means that the signals transmitted by GRAVES are scattered by meteor trails in the atmosphere, making it easy to receive reflections across large parts of Europe, even with a simple ground plane antenna.

There are several reasons for focusing on this area. Firstly, unlike visual meteor observations using cameras, radar observations are independent of weather and day-light conditions. This advantage allows radio observations to overcome the limitations that visual observation networks face, which often experience impaired sensitivity for significant portions of time. Additionally, radio observation can enhance the precision of meteoroid velocity estimation due to the significant Doppler effect observed in the reflected signals 0.2. The existence of a Doppler-shifted head echo (fig. 0.1) in meteor reflections was a key focus, as I planned to use this phenomenon to estimate meteor trajectories from signals received by multiple stations. This approach appears feasible, as there have been successful attempts to calculate meteor vectors in the atmosphere based on these Doppler-shifted signals (M. A. Vallejo², 2016 et al.).



Bolidozor_head_echo]

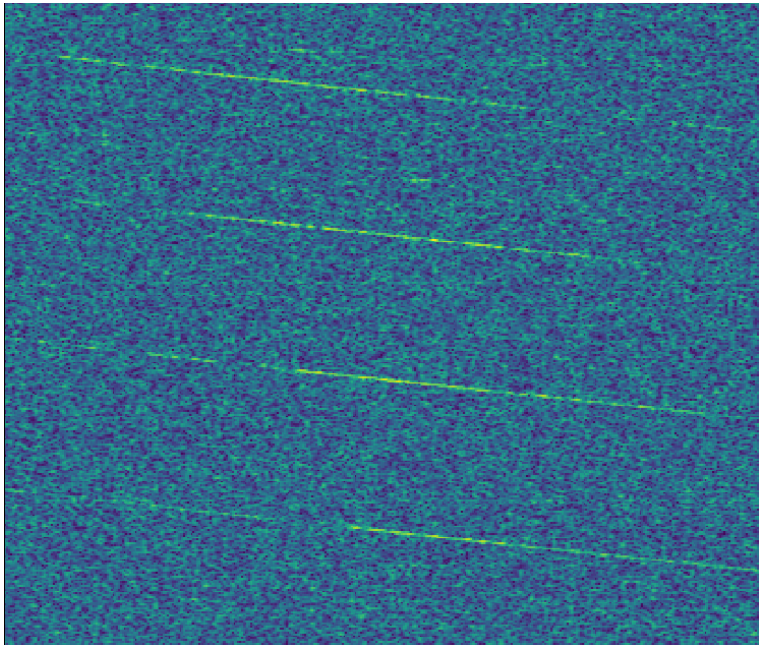
Figure 0.1. An example of a spectrogram from the Bolidozor network showing the head-echo (in the bottom of the image) Doppler shift on the two network stations.

The trouble begins with the fact that there is no easy way to verify that the calculated trajectory is correct or incorrect. The one issue roots in the situation is that radio signals received by the Bolidozor network have a detected meteor every few seconds which complicates the clear assignment of the specific visual observation to the

¹ <https://spp.fas.org/military/program/track/graves.pdf>

² Callsign: EA4EOZ

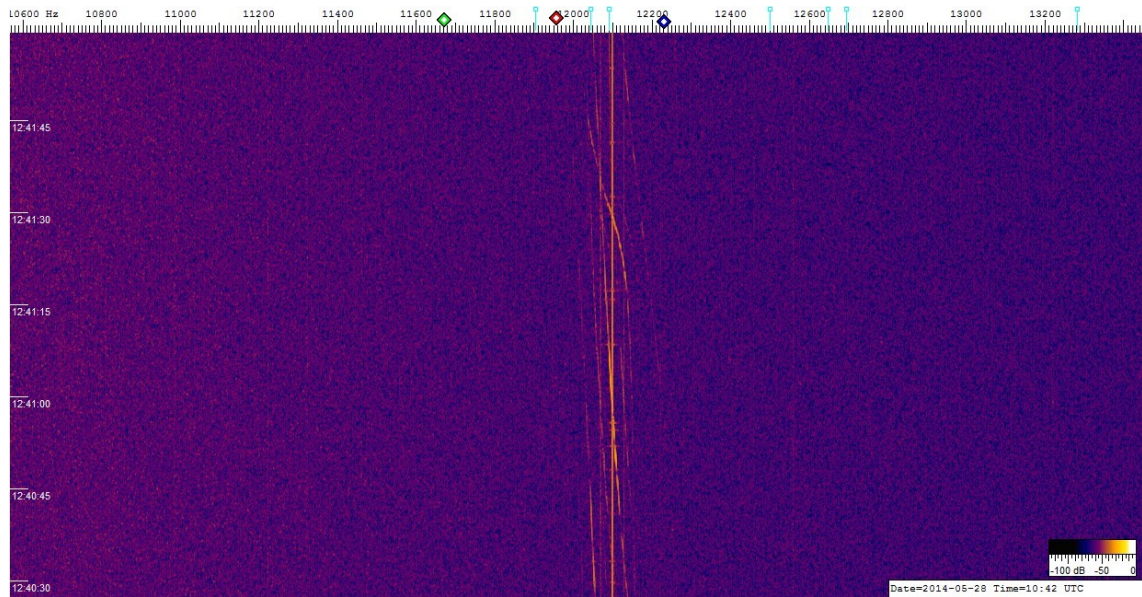
calculated trajectory. Especially in cases where a digital video camera occasionally has a few seconds of latency or inaccuracy. The second issue is caused by the situation that GRAVES radar guaranteedly lightens only a relatively small fraction of the atmosphere, but there are also side radiation lobes. The primary enlightened part is located above south Europe where there were little video detection networks at that time. The GRAVES radar also has a side transmission from its antenna, but these transmissions are not stable and there is not exactly a known enlightened area.



~~starlink_reflections]~~

Figure 0.2. An example of a spectrogram showing the Doppler-shifted reflections from Starlink satellites received on the Svákov Bolidozor station.

That results in very few meteor events, which could be used for trajectory verification by using the local video-based meteor detection networks here in the Czech Republic. To resolve this problem I decided to switch from GRAVES radar transmission to the local transmitters which are more suitable for local meteor detection. I selected the VOR beacons for airplane navigation. These beacons have reduced transmission power compared to GRAVES, but according to the numerical model I constructed the meteor radar based on that transmitters could be feasible with the use of state-of-the-art radio components.



dozor_VOR_airplanes]

Figure 0.3. Reflection from airplanes visible at the received signal from the VOR transmitter (Prague OKL). The Doppler shift curves are related to the airplane trajectories.

Unfortunately, that new approach requires a complete redesign of the existing signal processing and construction of the new receiver. That receiver should be capable of receiving multiple VOR transmitters at once because the frequencies of VOR transmitters are allocated in such a way that neighboring transmitters have significantly different frequencies to enhance airplane navigation safety and reliability. That results in the requirement of processing the 10MHz of signal bandwidth instead of the previous 192 kHz including a wide dynamic range of signal input, because this bandwidth will be likely affected by the strong nearby signals like a reflection from the airplanes visible in Fig. 0.3. These requirements for the receiver redesign were way beyond the initial project funding available; it is also beyond my manpower. Therefore I had steeply realized that the newly developed instruments needed to have commercial applications to avoid reliance on unreliable and discontinuous systems of scientific funding. As a result, I had to search for possible commercial applications that required the new instruments. That also explains why the majority of the newly developed instruments described in chapter 3 are currently commercially available. For the case of the new radio receiver, I found the following areas of possible applications:

- Meteor trail detection and localization
- LEO satellites downlink ground station
- Atmospheric electrical and ionization events observation

Luckily there arose an opportunity to cooperate with the CRREAT project whose main aim was the study of high-energy atmospheric events, where electromagnetic events in the atmosphere (electrometeors) observations fit well and at the same time are vital requirements. In the frame of that project, I designed the new receiver (described in section 3.2) concept with all mentioned applications in mind. That allows the construction of the receiver could be implemented with significant assistance of other members of the CRREAT team or external collaborators and with the use of CRREAT funding. But at the same time, there is a threat that the observation of lightning has similar issues as Bolidozor's radio meteor observation, because computing a location of lightning occurrence is possible, but there is a non-trivial task to verify that the

result is relevant. The requirement to build the ability to verify the calculated results branched out in the broad range of different work packages, which needs to be solved to gather relevant information about lightning or more generally atmospheric electricity from multiple sources. I describe ground-based, airborne, and remote sensing instruments in detail in the chapter 3. But for the overview of the tasks, firstly the lightning should be detected, the antenna should be calibrated, and the electric field needs to be measured at the same time. The lighting also needs to be simultaneously captured on high-speed cameras for geometric triangulation etc. That is why I need to design and operate the multiple measurement systems carried by cars on the ground and also in airborne vehicles presented and used in the following thesis.

Chapter 1

Introduction

1.1 Scope of the thesis

The objectives of this dissertation are to address and clarify several unresolved phenomena related to thunderstorms, particularly the initiation and development of lightning. This research aims to develop and utilize new tools for the detection and scientific observation of lightning events within thunderstorms. The focus will be on understanding the relationship between ionizing radiation and lightning, as well as developing innovative mobile instruments required for detailed storm observation. The specific tasks to be undertaken are as follows:

- **Development and Implementation of Lightning Detection Apparatus:** Mobile experimental apparatus capable of radio detection and localization of lightning events and ionizing radiation, considering the expected spatial scales, will be designed and deployed. Data will be collected using radio detectors, high-speed cameras, and ground-based electric field measurements.
- **Analysis of Spatial and Temporal Characteristics of Lightning Discharges:** The propagation of lightning, emitted radio signals, and associated electric fields will be studied. Methods for visualizing lightning discharges that avoid misinterpretation as ground strikes and more accurately reflect the physical principles of lightning development and radio signal emissions will be developed.
- **Enhancement of Measurement Techniques with in-situ atmospheric monitoring:** New instruments such as stratospheric balloons and unmanned aerial vehicles (UAVs) (especially unmanned autogyro) for in-situ measurements of electric fields and ionizing radiation will be developed. The new electric field mill and a semiconductor-based ionizing radiation detector will be integrated into the UAV.

The results of this research are expected to provide a deeper understanding of lightning initiation and propagation. At the same time, it offers improved detection and observation techniques that can inform future studies, about the relation to ionizing radiation with direct practical applications in meteorology and atmospheric physics.

[problem_definition]

1.2 Problem Statement

The activity of storms is associated with many phenomena whose nature is not yet fully understood or clarified. This includes the process of thundercloud electrification and the subsequent electric discharges, which are the most prominent manifestation of thunderstorms. As a result, weather forecasting and nowcasting of storm activity and related dangers are often very unreliable.

As one of many related phenomena, storm activity is also associated with the generation of ionizing radiation[1–7]. It is assumed that the source of this radiation is bremsstrahlung generated by electrons accelerated by an electric field in the thunderclouds[6–10]. These electrons that are accelerated to relativistic velocities are called

relativistic runaway electron avalanches (RREAs), which are then interacting with the atmosphere [11–12]. This causes a phenomenon that is to be often called terrestrial gamma-ray flash (TGF) [13] or another phenomenon like thunderstorm ground enhancement (TGE) [14–15]. For both, the source of the radiation is thought to be somewhat associated with the RREA; the main difference is the time span in which they occur [11–12]. Although it has not been experimentally proven. Furthermore, recent experimental results show that there is evidence of other ionizing radiation manifestations generated by the thunderstorms. For example, there has been experimental evidence of the interaction of high-energy photons with the atmosphere causing nuclear reactions [16]. The ionizing radiation that is thought to be associated with storm activity was measured using satellites in orbit around the Earth (e.g. [17]), aircrafts flying inside or in the vicinity of storm clouds [18–20] or high mountain observatories e.g. [21–23]. Currently, there are only a few measurements that could confirm the existence of ionizing radiation at lower altitudes, except for special storms that occur during the winter season in Japan, where storm clouds emerge low above the ground [24].

One of the most interesting measurements performed until now is the combination of radio signal and ionizing radiation. That experiment includes the mapping of a radio signal emitted by lightning [25–26]. There also exist TGF observations with a simultaneous lightning mapping using radio signals [27]. Despite these very detailed observations, the exact location of the source of the ionizing radiation emergence as a result of electric fields within the storm cloud remains unknown [28]. Moreover, the TGFs were only rarely successfully measured at the ground level [29–31].

It also should be noted that lightning phenomena manifest not only in the familiar forms that could be observed from ground level but extend into near-Earth space, presenting phenomena such as sprites, elves, gigantic jets, and also TGFs. All of these are powered by the intense electromagnetic and quasi-electrostatic fields related to lightning discharges. However, the specific properties of lightning discharges that lead to these high-altitude phenomena remain a subject of ongoing research, with studies leveraging both ground- and satellite-based observations to map global occurrence rates [32]. At the ground level the lightning discharges that could be observed, are classified into negative, positive, and bipolar. The taxonomy of lightning includes a range of discharges: cloud flashes (intracloud, intercloud, and cloud-to-air) and cloud-to-ground (CG) discharges, the latter accounting for about 25% of global lightning activity. CGs predominantly consist of negative downward lightning, where a negative charge is transported from the cloud to the ground [33]. Observations in tropical regions have introduced further classifications, including intra-cloud discharges, cloud-to-cloud, cloud-to-air, and express the polarity of lightning by ground-to-cloud, and cloud-to-ground discharges, noting the significant damage caused especially by cloud-to-ground and ground-to-cloud flashes [34]. Research into specific phenomena like ball lightning, sprite lightning reveals the versatility and is out of scope of this thesis, opening possibilities for further exploration of these rare and unique events [35]. While the general mechanics of lightning—its initiation and propagation—have been linked to specific atmospheric conditions such as the presence of graupel, ice, and hail, highlighting the relationship between lightning types and the microphysical characteristics of the convective regions, many aspects, including the differential occurrence rates and damaging potential of positive versus negative discharges, still invite further investigation [36].

Intracloud lightning discharges are known for their characteristic radio pulses, which consist of a uniform burst pattern. These bursts are described as a distinctive waveform

characterized by a fast, large amplitude pulse followed by a smaller, slowly varying overshoot. The full width at half maximum of these pulses measures 0.75 s, with inter-pulse intervals of 5 s [37]. The compact intracloud lightning discharge (CID), a particular type of intracloud lightning, is described as a bouncing-wave phenomenon. This involves multiple reflections occurring at both ends of the radiating channel, contributing to its fine structure and accompanying high-frequency (HF) and very high-frequency (VHF) radiation bursts [38]. An interesting characteristic of radio frequency emissions during thunderstorms is their nature compared to weaker emissions. The strongest pulses typically occur in isolation or at the beginning of leader progression. These pulses are sometimes associated with rapid electric charge relaxation and are not necessarily accompanied by visible light emissions. In instances where these pulses initiate, they are followed by an upward-progressing leader [39]. The study of lightning-induced radio pulses has been also expanded by observations from the satellites, which identifies additional characteristics in these emissions. Some exhibit steep roll-offs of power within certain frequency ranges, while others demonstrate flat-spectrum behavior. This distinction indicates the somewhat varied nature of lightning's electromagnetic emissions [40]. For cloud-to-ground (CG) flashes, the structure typically includes a sudden start with a stepped leader, in contrast to cloud-to-cloud (CC) flashes that initially showcase a slower train of noise pulses. These RF radiation patterns from lightning display a distinct structure based on the type of lightning flash, differentiating between the abruptness of CG flashes and the gradual initialization of CC flashes [41].

[lightning_signals]

1.3 Key radio signatures of lightning events

1.3.1 K-changes

K-changes, or K-complexes, refer to a specific pattern of rapid waveform of electric field change observed. The term K-change is used today to denote relatively small step-like static field changes that occur in between and after return strokes, and also during intra-cloud flashes [42]. A return stroke is the high-current electric discharge in lightning, occurring when the downward leader connects with an upward streamer, rapidly neutralizing the charge between ground and cloud and creating a bright, intense flash. This process involves currents typically reaching tens of thousands of amperes, propagating upwards at one-third the speed of light [43].

1.3.2 Narrow Bipolar Events (NBEs)

NBEs are distinct, intense radio pulses with a very short duration, typically a few microseconds, and are considered the most powerful natural VHF (Very High Frequency) sources in the Earth's atmosphere. They exhibit a remarkably narrow bipolar pulse shape and are believed to result from a rapid discharge process within thunderclouds, possibly associated with the initiation stages of lightning [44].

1.3.3 Sferics

Sferics is short for atmospherics, the term used for radio waves emitted by lightning discharges. These signals, spanning a broad range of frequencies but most commonly observed in VLF and LF bands, represent the electromagnetic signature of distant lightning's return stroke. Sferics carry distinctive timing information, making them valuable for long-range lightning detection and location systems[45].

[literature_review]

1.4 Literature Review and state-of-the-art

Atmospheric electromagnetic phenomena have been identified as mandatory physical properties influencing atmospheric radiation processes. These phenomena, including lightning, sprites, and other events, are also a significant part of the formation of cloud structures and significantly impact the movement and characteristics of atmospherically relevant subsystems [46]. The evolution of radio transmission has been one of the earliest methods of regular observation of atmospheric electricity (e.g. sferics). Rapidly revealing the existence of atmospheric charge structures like the ionosphere and its variation, forming the atmospheric waveguide allowing propagation of radio waves produced by lightning over long distances. Research has also delved into the dynamics of geomagnetic pulsation regimes and their interaction with the Earth's magnetosphere, reflecting the interactions resulting from powerful solar flares [47]. In parallelly ongoing meteorological research, the integration of advanced technologies from aviation starting from balloons led to the discovery of cosmic radiation [48–49]. The balloon observations were combined with radio transmission to be automated in the form of radiosondes [50–51]. That technology has been improved and used for decades, until the most recent stage of evolution in Unmanned Aerial Vehicles (UAVs) [52]. A significant contribution of radio engineering in meteorology comes from the invention of the radars, which are used for remote sensing of atmospheric structures. Remote radio sensing and in-situ measuring methods are also combined to obtain multiple perspective views on electric phenomena. [53–55] The increasing requirements on lightning safety during space race significantly enhance the technology of ground-based equipment such as electric field mills and radio-based lightning detection and mapping systems [41, 56–57]. The state of art of this radio-based technology utilizes large area EFM arrays for observation in the form of non-intrusive methods to determine atmospheric electric fields and also mapping of lightning evolution and structure. Notable examples of these systems are New Mexico Tech's Lightning Mapping Array (LMA) [58], FALMA [59], community-based network Blitzortung.org [60] and also LOFAR radio telescope [61]. Based on the mentioned instruments which were originally developed directly for scientific purposes or safety engineering. There also emerges a lot of commercial products and services for civil lightning awareness. As examples, there could be mentioned the Vaisala lightning sensors [62], WWLLN [63] and LINET [64].

1.4.1 Summary of Initial Assumptions

The following scientific assumptions provide the foundation for the following research. While they represent the initial understanding in the field, this dissertation will critically examine and test these assumptions to enhance or refine the knowledge of thunderstorm phenomena:

- Research in phenomena in thunderstorms, such as ionizing radiation production has often focused on the peaks of electric fields associated with the initiation of lightning [Kolmašová, et. al., 2015]
- Lightning discharges are generally considered to be short-duration events typically ranging from tens of microseconds [Kolmašová, et. al., 2015], to up to 350 milliseconds [Rakov & Uman, 2003; López et al., 2017]
- The spatial extent of lightning discharges is believed to be limited to approximately 15 kilometers from the initiation point [Thottappillil et al., 1992; López et al., 2017] It is commonly accepted that ionizing radiation is generated before

or during lightning events, primarily in a vertical direction parallel to the electric field intensity vector [Enoto et.al., 2017]

- Much of the existing research on lightning discharges focuses on the return-stroke phase, a key phase of cloud-to-ground discharges [Uman, 1969; Berger et al., 1975; Dwyer et.al. 2012]

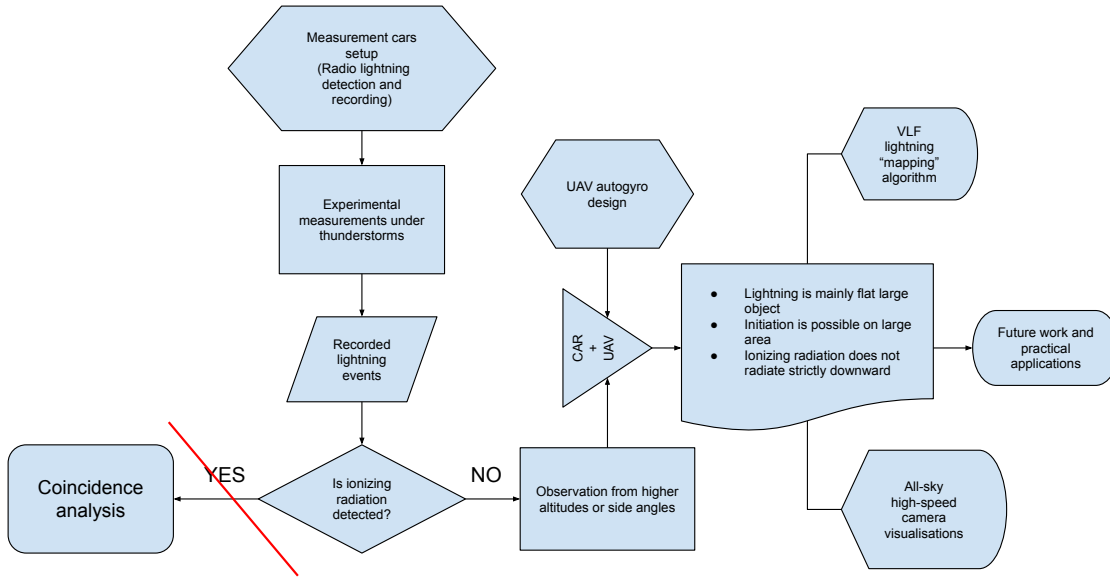
1.5 Contributions

Based on the theoretical framework and assumptions outlined in the 1.4 section, I developed a comprehensive research methodology. This methodology includes the use of measuring vehicles and unmanned aerial vehicles (UAVs) to improve the detection of radiation phenomena associated with thunderstorms. The primary objective is to position detection devices as close to or beneath the storm core as possible, thereby increasing the likelihood of capturing relevant radiation events.

The main research methodology is based on the following key components:

- **Utilization of Measuring Vehicles:** I use measuring vehicles equipped with specialized instruments for detecting radio signals and ionizing radiation. These vehicles also serve as mobile platforms, providing the necessary ground support for the UAVs. They are at the same time equipped with a range of auxiliary devices to capture the interrelationships between the measured data. For example, scintillation detectors for ionizing radiation must account for the influence of temperature changes on sensitivity, and disdrometers are used to measure the intensity and type of precipitation that can wash radon products from the atmosphere, causing increased radiation levels, which could easily be interpreted as TGE.
- **Deployment of UAVs for Radiation Detection:** The multiple UAVs, are equipped with detectors for ionizing radiation. The UAVs are tasked with locating and identifying sources of ionizing radiation in the atmosphere. This method leverages the strong presumption that the intensity of generated ionizing radiation diminishes with increasing distance from its source. The UAVs provide data on ionizing radiation that is difficult to obtain from ground-based measurements alone. Therefore UAVs are supposed to observe thunderstorms cooperatively with measuring cars.

The flowchart depicted in fig. 1.1 illustrates a high-level workflow of the research. It begins with the setup of measurement cars equipped with radio lightning detection and recording capabilities including an all-sky high-speed camera on the two cars. Experimental measurements are then conducted under thunderstorms, with recorded lightning events analyzed for the presence of ionizing radiation. These attempts lead to insights such as the flat, large object nature of lightning, the possibility of lightning initiation process over large areas, and the observation that ionizing radiation does not radiate strictly downward. Parallel to this, the UAV autogyro and other instruments are designed to aid in these measurements. Observations are then supposed to be made from higher altitudes or side angles to enhance data collection. Then the data from both the measurement cars and UAVs needs to be combined.



[workflow]

Figure 1.1. Simplified workflow for detecting and analyzing lightning radio signals and ionizing radiation using measurement cars and UAVs.

To address the general unavailability or limitations of commercially available instruments, as well as issues with data quality due to closed design and lack of transparency in internal data filtering processes, I developed several bespoke instruments. These custom-made tools were essential to ensure reliable measurements. Notably, the following instruments were developed to meet the specific needs of this research:

- **Lightning Radio Signal Receivers:** These instruments were used to implement a method for triggering data recording by lightning signals, ensuring high sensitivity to natural lightning while minimizing false positives from man-made signals. This innovative solution is detailed in the section 2.
- **Unmanned Autogyro for atmospheric measurements:** To address the lack of available unmanned systems capable of measuring ionizing radiation or electric fields within storm clouds, I developed an unmanned autogyro designed for atmospheric measurements under various weather conditions. Unlike traditional measurement balloons, which are unsafe and yield sporadic results due to limited control, the autogyro offers precise control and stability even in turbulent conditions.
- **Measurement Support Systems:** Design and integration of an instrument toolset that allows simultaneous detection and recording of lightning event signals, electric field distribution, ionizing radiation, camera recordings, and meteorological data. The detailed design of these instruments is presented in the chapter 3. Measuring vehicles are also equipped with systems for wind speed and direction measurement, and sensor orientation recording, necessary for UAV launch from the car platform, landing, flight control, and lightning localization.

The contributions of the designed instruments to the understanding of thunderstorm-related phenomena are demonstrated through various experiments. These experiments are described in detail in the chapters 4 and 5. The measuring vehicles and UAVs' ability to relocate flexibly and conduct ground measurements at storm sites significantly enhances the future capability to capture and analyze storm-related ionizing radiation events.

1.6 Outline of the thesis

The initial part of the thesis 2, describes the construction and test of a device engineered to automatically capture data from lightning events. The chapter has been one of the initial work packages because the described methods enable the recording of instruments synchronized with the lightning. That is the essential feature needed for every additional described step of the following research.

This is attributed to the fact that within the scope of storm evolution, lightning can be seen as occurring in relatively brief and sparse periods compared to the more extended spans of storm activity without lighting (and supposedly also without ionizing radiation), as discussed in the chapters 1.4 and 1.2. Simultaneously, the flow of individual ionizing radiation particles or photons during TGF or TGE spans a broad spectrum of possible energy levels. That does not permit the setting of an exact recording threshold at the individual instrument, given the sensitivity capabilities of available equipment. Therefore, ionizing radiation detectors, and the majority of other instruments, like radio receivers and high-speed cameras, are required to capture event data throughout its actual occurrence, and this data fragment should subsequently be analyzed to examine the underlying phenomena.

Therefore these instruments are at the same time examples of scientific devices capable of generating an enormous amount of data. Such volumes of data are (with the actual technology level) difficult to store within the intervals between events, e.g. lightning. That is the main rationale behind the need to create a reliable method of triggering the recording of all instruments depending on lightning activity to store event-based data fragments.

In the 3 chapter, are explored the exact designs of the innovative tools and devices engineered especially to improve the study of lightning in thunderstorms and the related atmospheric phenomena. The design and development of these instruments were initially guided by literature listed in the chapter 1.4, which suggested typical lightning properties that early experiments soon called into question. This suspicion led to multiple iterations in the construction of instrumentation, as the original assumption of lightning's brevity—thought to correlate the event data with the vertical development of lightning channels over tens of milliseconds—proved grossly underestimated, as the actual ranges of these events are several orders of magnitude greater. This situation also changes the requirement on examined electric field gradients, because the vertical gradient detection needs to be exchanged by a horizontal or more ideally the 3D space distribution. The chapter discusses the rationale behind the instrument development, its design principles, and how these advancements improve upon existing technologies. It also details the experimental setup and integration of these tools into broader research methodology, emphasizing their future potential to significantly advance the understanding of atmospheric electricity.

However, because it was necessary to first verify the developed instruments on more deterministic processes than direct measuring during a storm activity, a large number

of supportive experiments were conducted, which served to verify the properties of the instruments and their supporting subsystems. These experiments included flights of stratospheric balloons and UAVs as well as ground measurements with similar instrumentation either at stationary or mobile measuring stations. The chapter 4 therefore documents the extensive preparatory work necessary to validate the proposed instruments' efficacy before their direct application in thunderstorm research.

The chapter 5 synthesizes the insights gained from the application of the developed instruments in the field, reflecting on the contributions this research has made to the field of atmospheric sciences, particularly in understanding lightning phenomena. It evaluates the effectiveness of the newly developed instrumentation in capturing comprehensive lightning data, discusses the impact of these findings on existing theories, and considers their practical implications. Furthermore, it outlines future research directions, suggesting areas where further investigation could yield substantial advancements in the study of atmospheric electricity with the additional use of similar instrumentation. This final section underscores the thesis's role in enhancing scientific knowledge and its potential for real-world applications in weather forecasting and safety measures.

[triggered_recording]

Chapter 2

Lightning triggered recording

Because recording and then processing the large amount of data captured continuously over thunderstorm development is technically difficult (the technical difficulties are detailed in the chapter Proposed Instrumentation, specifically in sections describing radio and camera instruments), it is needed to have the ability to determine the precise time of the lightning event, with a low rate of false detections. That requirement is enhanced by the fact that data recording is triggered by every false detection, which takes several minutes. This interval creates a “blind” dead time during which the instrumentation is unable to capture another event. To solve that issue, multiple iterations of a mobile measurement system and detectors, which are triggered by electromagnetic emissions produced by lightning, have been developed. Although optical, radio-wave (electromagnetic), and infrasound-based lightning detection methods exist, the radio-wave detection method is considered to be the most suitable for the intended application, due to its detection range and relative insensitivity to meteorological conditions (hail, snow, rain, and sunlight) at the time of the lightning discharge. It is also considered suitable for the near-to-real-time detection of lightning. Another requirement of the proposed system is being capable of precise detects of lightning with precision in the order of several kilometers in position and better than milliseconds in time. The widespread method used for radio lightning detection is based on the detection of the magnetic part of an electromagnetic field generated by lightning. Examples of instruments using this method available for comparison in the Czech Republic include the use of the SLAVIA magnetic loop antenna [65] and the stations of the lightning detection system deployed in the Blitzortung.org network [66]. However, these systems are not designed to be highly portable, nor to be used as a measurement trigger source in offline and stand-alone operations, making it necessary for us to find a mobile, lightweight, and low-power consumption lightning detector. Based on the sources in the literature review section 1.4 the development and implementation of algorithms for real-time lightning detection in ground-based systems seems to be an already solved problem. The used solution is only a part of more sophisticated lightning location and mapping systems. Unfortunately, lightning detection in these systems is based on signal-level detection. The signal level is set to individual stations based on the analysis of the data stream coming from the station by the network server. That simple solution is not suitable for detecting lightning in generic electromagnetic noisy environments and requires station placement in electromagnetically quiet areas. There also exists a conference paper [67] introducing an adaptive signal detection algorithm based on short-time energy detection and Constant false alarm rate (CFAR) for real-time VHF intracloud lightning signal detection. This adaptive approach is promising to enhance the performance of lightning detection systems in ground-based setups by dynamically adjusting to varying signal characteristics, but unfortunately, the statistics of noise background need to be known. Therefore that could be hardly used for mobile measurements. Therefore there is not an existing solution that could be used for the planned research.

[LIGHTNING01A_trigger]

2.1 Off-the-shelf lightning detection

Initially, I investigated the lightning-triggering device based on the AMS AS3935 integrated circuit and used a coil antenna. The device meets the requirements of mobility and low power consumption. For measurements of coincidence between ionizing radiation and lightning aboard aircraft, for example, the compact physical size of the device is also a considerable advantage, therefore the solution seems to be promising. Then I compared the performance and reliability of the detector with the Blitzortung lightning detection network. I chose Blitzortung as a network that has a good deployment in central Europe where the mobile measurements were performed. Therefore two detection systems were selected for atmospheric discharge detection in this study: the device based on the AMS AS3935 integrated circuit and a coil antenna and the Blitzortung.org lightning detection network [60]. Both of these lightning detection systems use radio emission reception at VLF frequencies. The devices differ in the design and realization of the antennas and implementation of the lightning detection algorithm. The device equipped by AMS AS3935 uses LIGHTNING01A MLAB module [68] with a coreless coil antenna connected as a resonant LC circuit (Figure 2.2). The resonant frequency of the coil antenna (MA5532-AE) with temperature-insensitive C0G ceramic capacitors is matched at $500 \text{ kHz} \pm 3.5\%$. This strict matching requirement is required by the IC datasheet [69] and is quite constraining and effectively limits the possible application of the circuit. According to the manufacturer's description, the integrated circuit processes signals based on the signal level threshold detected by a comparator. If the comparator triggers, the proprietary signal processing unit algorithmically analyzes the signal. The output of the signal processing algorithm implemented in the AS3935 circuit consists of a classification of signal relevance: lightning discharge (8), artificial disturbance (4), or high noise level (1). The algorithm also determines the approximate distance and the estimated energy of the lightning discharge based on signal shape. The internal registers configuration for a measurement described below was set to "outdoor mode" by the AFE_GB control register. All other registers are kept with implicit values. The circuit diagram including the AS3935 is shown in Figure 2.3. The integrated circuit is powered by a 3.6 V from one primary lithium-thionyl chloride cell without the usage of an integrated LDO (low drop-out) stabilizer. An I2C (Inter-Integrated Circuit) bus is used for communication with a data logger that also records data from pressure and temperature sensors. A GPS (Global Positioning System) receiver is used for logging of the precise time. The data is stored on an SDcard in a module [70]. A block diagram of the interconnections is shown in Figure 2.4. The used firmware for the device is available at [71].

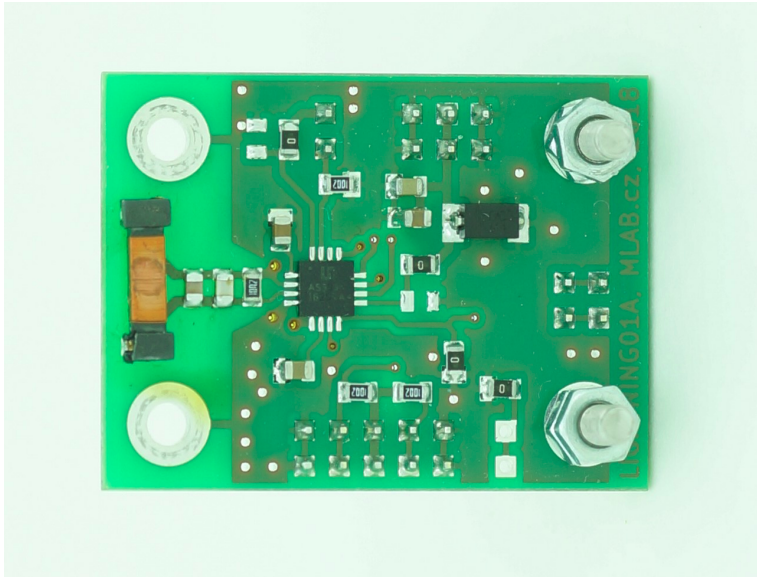
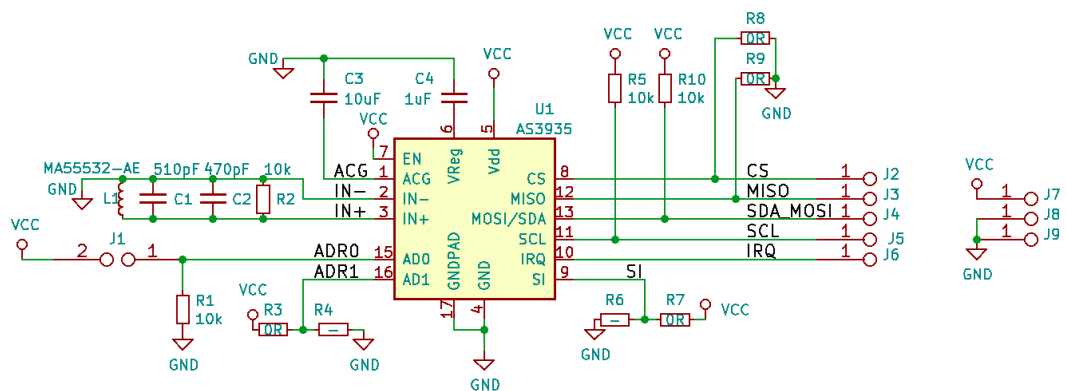


Figure 2.1. The bottom side of the newly designed LIGHTNING01A module [68]. The antenna coil is visible on the left. The tuning capacitors and Q-limiting resistors are mounted on the right side of the antenna.



[DIVISEK01_PCB]

Figure 2.2. Schematic diagram of the lightning sensor based on commercially available AMS AS3935 IC (used in LIGHTNING01A [68]).

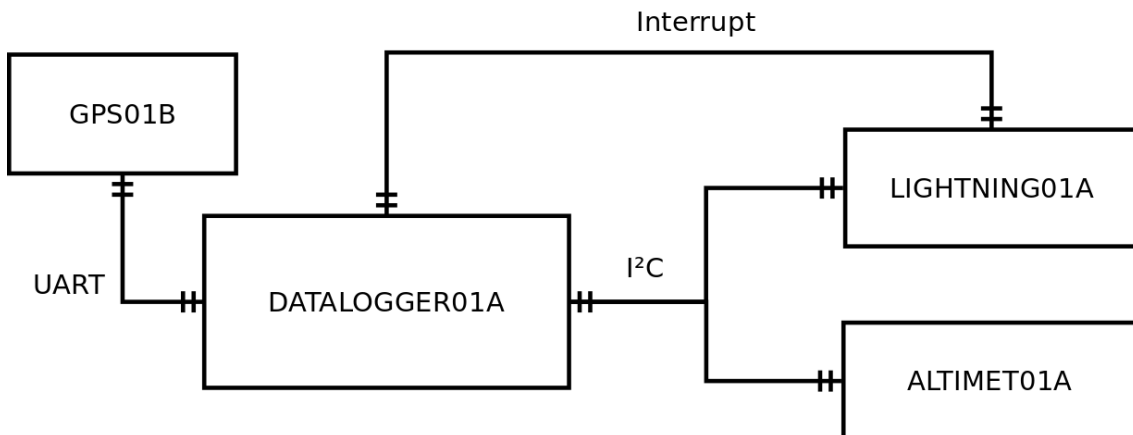


Figure 2.3. Schematic block diagram of the examined lightning detector. Detailed schematics of modules are available at [70, 72, 68, 73].

The time response of the lightning detector was tested in the laboratory before field measurements using a power signal generator with a wire loop of 60 mm diameter. The wire loop was placed at a distance of 30 mm from the antenna. The interrupt output was captured by an oscilloscope. Response time to a rectangular signal was 93 ms (± 1 ms). The rectangular signal pulse was classified by the internal algorithm as a disturbance (“DIVIS4” output in the log file). The response time to the received signal was found not to be constant for each signal. Some pulses were classified as lightning (“DIVIS8” in the log file) by the proprietary algorithm where the response time was only a few milliseconds. Due to the time delay introduced by the algorithm, the device could be potentially used for triggering other measuring devices by using a pretrigger recording buffer of maximal algorithm latency plus lightning duration. For a lightning event duration of less than 900 ms, a one-second pre-trigger buffer was found to be suitable.

The proposed system, powered by one LS33600 cell, can operate continuously for five days. Power consumption is dominated by the GPS receiver. The lifetime of the system without GPS is approximately three months. For measurements in the field, the instrument is mounted on the roof of a measurement car inside a waterproof plastic box as shown in figure 2.2.

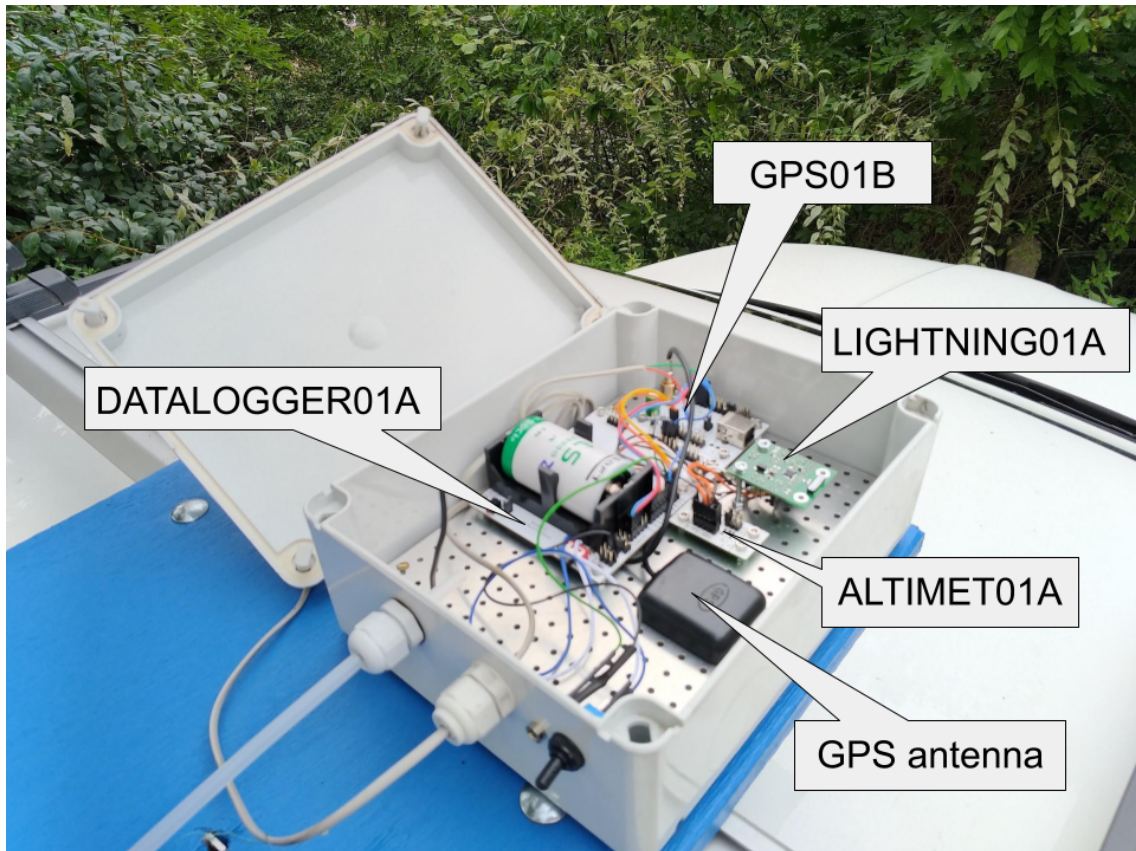


Figure 2.4. The examined deployment on the roof of a car. The module LIGHTNING01A [68] with antenna is located in the upper right corner of the box. Module with battery is DATALOGGER01A [70]. GPS receiver [72] is located in the upper left corner with a connected black GPS antenna. Rest module beside LIGHTNING01A is ALTIMET01A [73].

[DIVISEK01_Deployment]

2.2 Blitzortung network

The second investigated option of triggering was the use of the Blitzortung.org network. Blitzortung.org is a World-Wide Low-Cost Community-Based TDOA Lightning Detection and Lightning Location Network [66, 60]. Blitzortung.org collects signals that are received by a combination of multiple magnetic loop antennas and electric monopoles deployed at network stations [60]. The configuration, implementation, and sensitivity of stations are not uniform. There are multiple causes for these differences. e.g. - the network members have different hardware versions, and different quality of maintenance, and the antennas are mounted at different locations¹.

Such variance of network parameters could be considered as beneficial because it increases sensitivity to different lightning signal types. The most common implementation of the magnetic loop antenna in Blitzortung.org network sites consists of several loops of shielded coaxial cable, where the inner conductor is used for the magnetic loop itself, and one end of the shield is connected to the antenna amplifier ground. The antenna is not tuned to the specific resonant frequency. However, the goal of the station operators is to maintain the highest achievable resonant frequency [60].

The Blitzortung controller outputs a 256-byte signal fragment covering the pulse with a time resolution of 1.95 s along with the timestamp of the trigger and metadata of the station location, GPS signal quality, and validity of data. Detailed signal processing is carried out on the network server. The final result of the data processing in the Blitzortung network is the approximate location of the sources of each captured pulse. The signal processing is carried out in two steps. In the first step, a starting point is computed by a time of arrival algorithm [74] from the first four-time stamps corrected for time of group arrival [75]. In the second step, a numerical method is used to minimize the sum of squared distances to the hyperbolic curves.

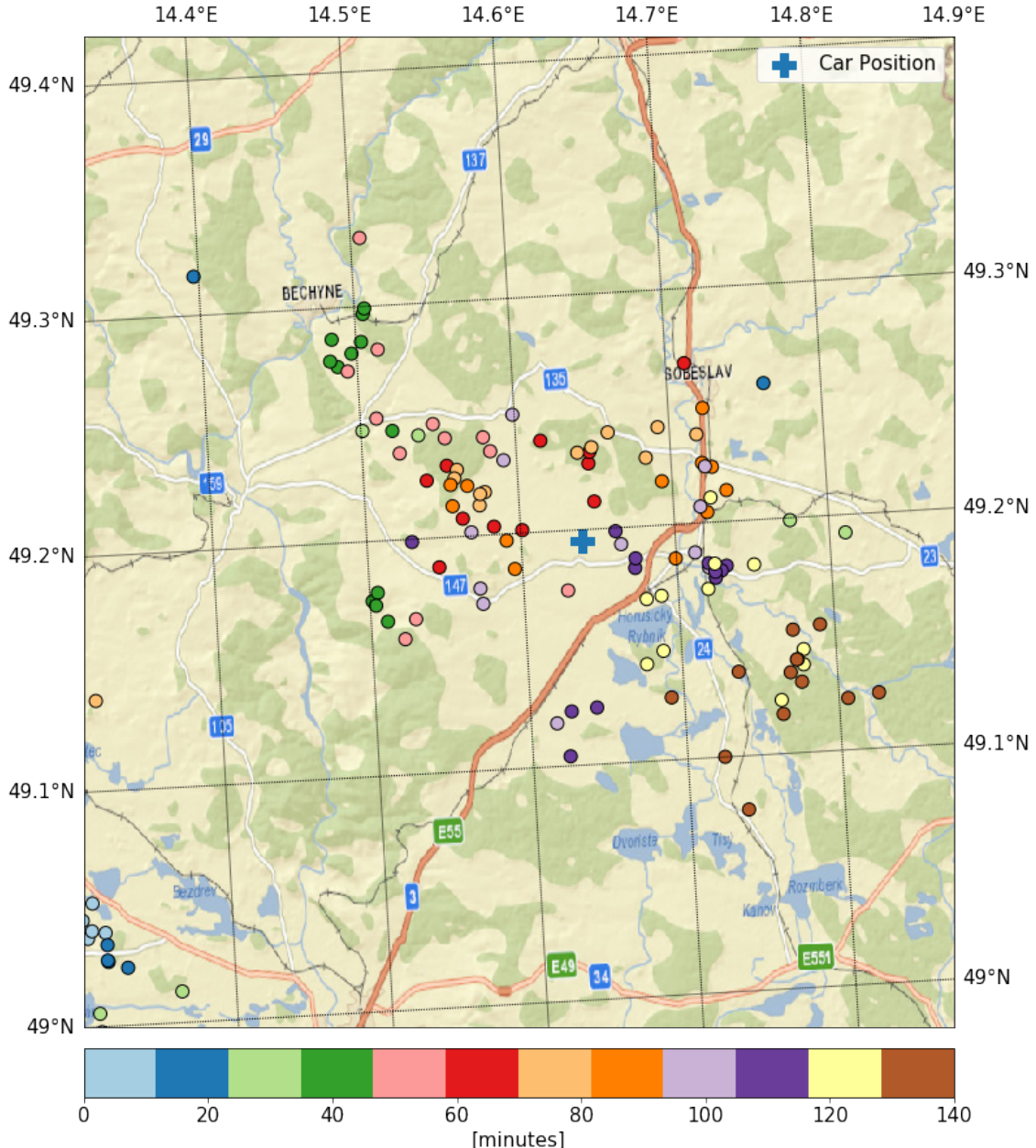
To use Blitzortung.org as a recording trigger both the processed data from the server and the use of the station itself were investigated. The usage of the Blitzortung station hardware was relatively quickly abandoned because the station is not constructed to trigger lightning signals in proximity to the thunderstorm. Therefore the station usually reaches something like an “overage” which is called an “interference mode” in Blitzortung.org terminology². The practical result is that the station is not able to generate relevant triggers for lightning. Instead, it triggers very frequently. Sometimes the opposite situation arises - the Blitzortung.org station can detect lightning far away but is not able to trigger lightning in a near vicinity. The situation is dependent probably on the storm development and the terrain. However, in both cases, the station trigger output is not usable for triggering other devices. There is a possibility that the situation could be resolved by changing the Blitzortung station firmware, unfortunately, the firmware is closed source, similar to the exact implementation of location algorithms used on the servers.

2.3 Comparison of different triggering methods

During the triggering method development, the devices were regularly tested by a car measurement campaign. There could be shown an example of data captured during a thunderstorm near the village of Borkovice, Czechia (car position 49.1949915 N, 14.639835 E, at altitude 427 m a.s.l.) on August 3, 2019, as shown in figure 2.5.

¹ https://www.blitzortung.org/en/station_list

² <https://info.lightningmaps.org/doku.php?id=en:hardware:red:operation:interference>

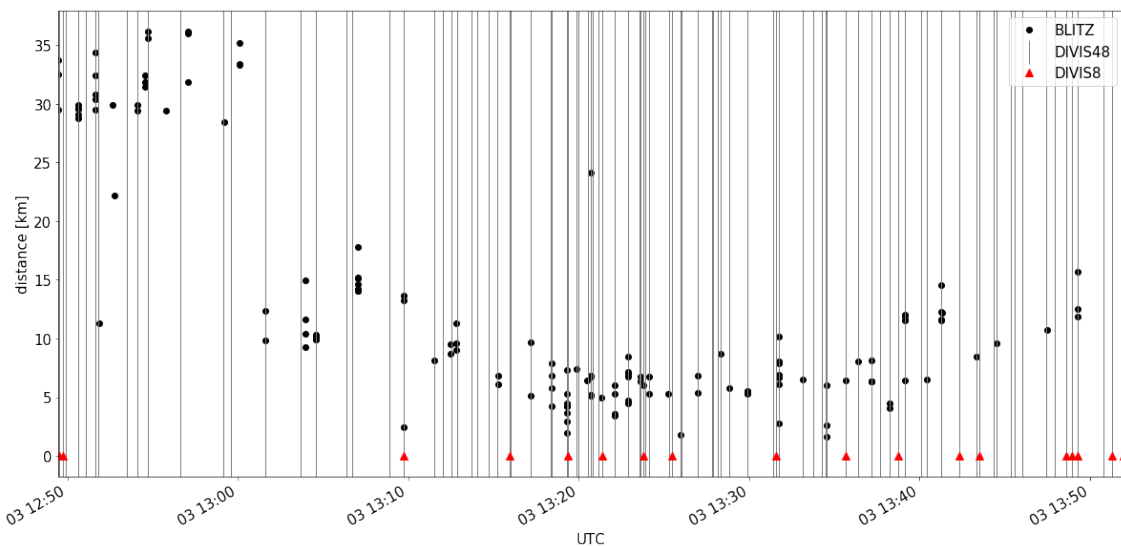


[lightning_times]

Figure 2.5. The position and timing of a thunderstorm at Borkovice. The circles are positions of lightning registered by the Blitzortung network. Color depends on the relative time of lightning after a measurement car stops. The car position is marked as a blue cross.

The timestamp of lightning detected by LIGHTNING01A was recorded with a 1 s accuracy. The Blitzortung network provides timestamps down to a 1 μ s accuracy. Fig. 2.6 shows all lightning-triggered signals in all devices over a time period from 12:49 to 13:52 UTC, a time interval during which the car did not change position. LIGHTNING01A distinguished between artificial discharges (depicted in the Fig. 2.7 as DIVIS4) and natural lightning (depicted in the figure as DIVIS8). Coincidences between LIGHTNING01A and Blitzortung.org detections are shown in Tab. 2.1. The nearest detections around the measurement car are depicted on the map in Fig 2.5. Tab. 2.1 and Fig. 2.7 are generated by algorithms realized by Jupyter notebooks [76].

The final assessment of binary time events data was done by a similar approach as described in a work [77].



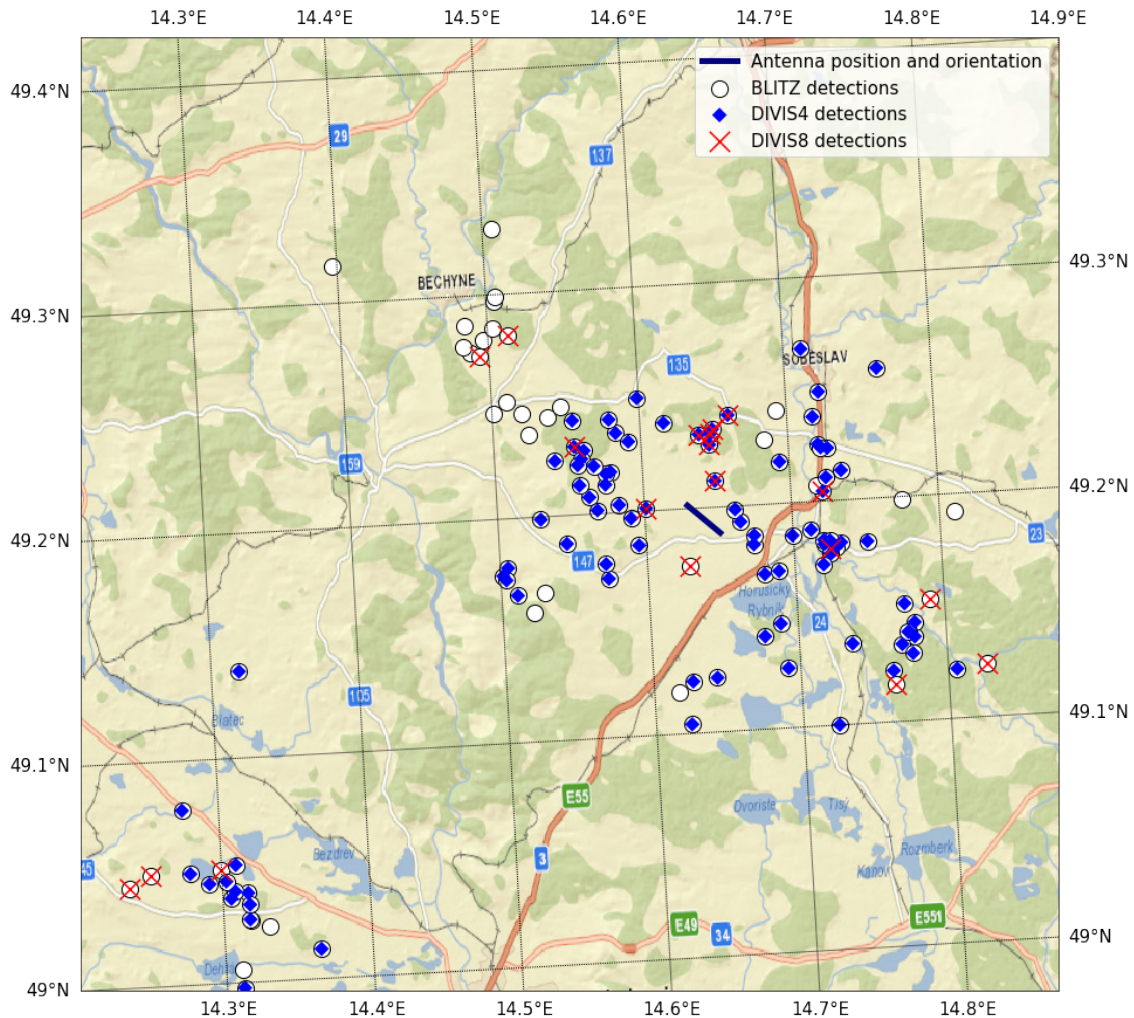
`detection_timeseries]`

Figure 2.6. Detections of the two studied methods. For Blitzortung.org there are detections labeled as BLITZ, the vertical axis corresponds to the distance between the Blitzortung.org location and the fixed position of the LIGHTNING01A deployment. Vertical lines represent all LIGHTNING01A's detections (DIVIS48). Triangles point to detections recognized by LIGHTNING01A as lightning (DIVIS8). For LIGHTNING01A the vertical axis is not relevant, because the sensor does not provide a precise distance.

	Count	BLITZ5	BLITZ10	BLITZ20	BLITZ30	DIVIS48	DIVIS4	DIVIS8
BLITZ5	19	1.000	1.000	1.000	1.000	0.947	0.895	0.368
BLITZ10	78	0.462	1.000	1.000	1.000	0.872	0.846	0.141
BLITZ20	109	0.358	0.844	1.000	1.000	0.798	0.734	0.147
BLITZ30	123	0.317	0.756	0.894	1.000	0.797	0.732	0.138
DIVIS48	128	0.164	0.453	0.492	0.539	1.000	0.875	0.156
DIVIS4	110	0.173	0.491	0.527	0.573	1.000	1.000	0.018
DIVIS8	18	0.111	0.222	0.278	0.333	1.000	0.111	1.000

[t1]

Table 2.1. Table of coincidence rates among detectors. The presented values are the proportion of detections in the row-labeled detector for which there is at least one coincident detection of the column-labeled detector. The Blitzortung network is represented by virtual detectors BLITZ5, BLITZ10, BLITZ20, and BLITZ30, which are considered triggered upon registered lightning in a 5 km, 10 km, 20 km, and 30 km radius respectively around the LIGHTNING01A deployment. DIVIS48, DIVIS4, and DIVIS8 are the LIGHTNING01A detector with different filtering of candidate detections, with DIVIS48 having the most lenient filtering. The count represents the absolute number of events measured for the detector/conditions in each row.



`ection_coincidences]`

Figure 2.7. Map of Blitzortung.org detections with LIGHTNING01A coincidences displayed. White marks show the positions of all Blitzortung.org detections in the region and time period of interest. If a Blitzortung.org detection coincides with a DIVIS4 or DIVIS8 detection, an additional blue or red mark, respectively, is placed.

The records produced by LIGHTNING01A allow for recording of the absolute time of the detected event within a ± 1 s window. As a basic evaluation of LIGHTNING01A's fitness to trigger other measurement instruments, where coincidences were counted among LIGHTNING01A detections and detections from Blitzortung.org in multiple predefined radii. The coincidence rates obtained are presented in table 2.1. Events were considered coincident if they fell within a ± 1.5 s time window. This value for the window width was selected such that the absolute time uncertainty of LIGHTNING01A records, the latency of LIGHTNING01A response, and the duration of lightning phenomena, which may conceivably be in the order of hundreds of milliseconds, were accounted for. For window widths in the range of ± 1.2 s to ± 2.0 s, the coincidence rate between any pair of detectors does not differ by more than 0.05 from the table value, which corresponds to the window width of ± 1.5 s.

For illustration, those of Blitzortung.org detections that were coincident with LIGHTNING01A detections were picked out, and these are plotted on a map in figure 2.7. It should be noted that none of the systems compared here has 100% detection efficiency [78].

If Blitzortung.org is postulated as a reference system, it can be seen that LIGHTNING01A (see column DIVIS48 in the table) covers 94.7% of Blitzortung detections in the range of 5 km (BLITZ5) and more than 79% in the range of 30 km (see the line BLITZ30 in the table). The detection of long-distance lightning is possibly influenced by the directional characteristics of the antenna. The sensitivity of the antenna (measured in the number of coincident lightning) is higher in the direction perpendicular to the antenna orientation (see figure 2.7; compare the sector around 49.0° N, 14.3° E with 49.3° N, 14.5° E).

It can be seen from table 2.1 that the proprietary lightning detection algorithm implemented in the AMS chip, which is supposed to distinguish lightning from man-made disturbance, cannot be relied upon. Only 36.8% of lightning detected by Blitzortung.org are considered as lightning by LIGHTNING01A (DIVIS8). Therefore, all DIVIS8 and DIVIS4 events (DIVIS48) have to be considered. However, 42.7% of DIVIS4 detections are not registered by Blitzortung at distances up to 30 km. These are likely to be false detections or detections beyond the evaluated range of 30 km. Blitzortung.org network and LIGHTNING01A detector differ not only in sensitivity, but also in usability due to issues of network connectivity, power requirements, device size, and noise filtering capabilities. For most of these parameters, the LIGHTNING01A device was found only partially suitable as an electromagnetic lightning detector used in this work for terrain measurement. Blitzortung.org is designed to filter noise signals (false detections) by a network of detectors. Consequently, Blitzortung.org gives a useful trigger after the signal has been processed by a network server. It is done in seconds and it is too slow for mobile measurement purposes. LIGHTNING01A has limited ability to reject autonomously noise signals which is important to avoid filling a memory of other instruments by data captured by false trigger signals, but this ability is not sufficiently robust.

However, the findings looked initially promising, because LIGHTNING01A is a lightweight, highly mobile, battery-operated lightning detection system based on the AS3935 integrated circuit with possible application of radiation measurement in thunderstorms on board aircraft.

This LIGHTNING01A is suitable only for triggering terrain measurement devices (lightning discharge mapping device, ionizing radiation detectors, electric field measurement, etc.) with the presumption that triggered devices are capable of recording the data in intervals at least from one second before the trigger to one second after the trigger, which is caused of the uncertainty of lightning trigger output from the AS3935 chip.

Additionally, for applications like ionizing radiation measurements, the sensitivity is considered too high, since lightning more than 10 km away from the ionizing radiation measurement venue is not of interest. The sensitivity of the AS3935 device can be decreased by increasing the level of the lightning detection threshold. This can be done by setting the internal SREJ or WDTH registers of the AS3935, as shown in figure 20 or 21 in the datasheet [79], but this also affects the overall sensitivity of the device. Therefore, the false negative rate for near lightning is increased.

Only a slight directional sensitivity of the antenna was observed. This could theoretically be compensated by pointing the AS3935's antenna (or the whole measurement car) towards the thunderclouds; however, for close lightning within a 5 km radius, this effect is negligible. In conclusion, I found out that a detector based on the currently widely used detection chip AS3935 has limited usability for purposes of lightning recognition and is not able to detect some discharges. Further search is therefore necessary

to find a more reliable way of lightning detection and triggering during thunderstorm development.

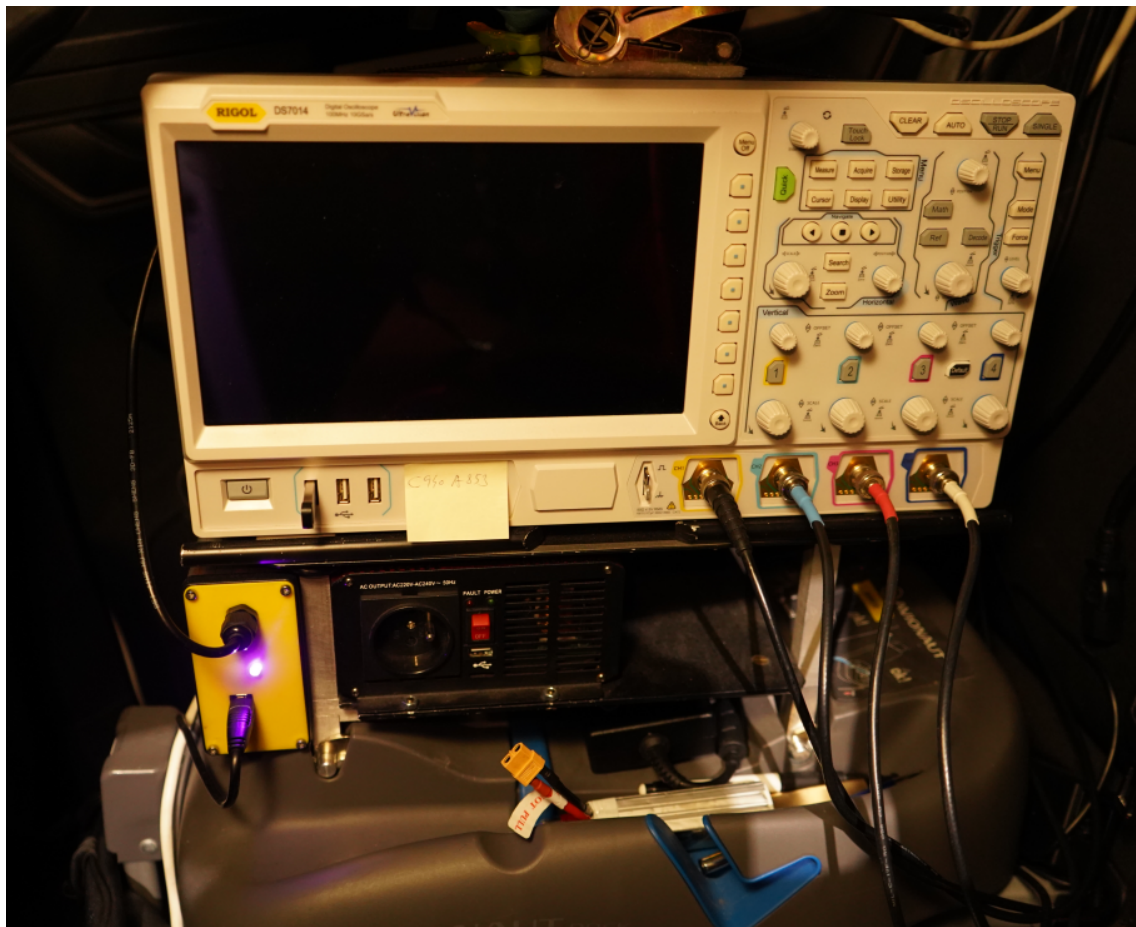
2.4 Additional investigation of triggering methods

Since the previously mentioned method using existing commercially available solutions for triggering recordings proved to be insufficient during actual measurements, it was necessary to explore further possibilities. From the signal detection theory, if the signal is known and determined, the signal can be detected by using the signal replication and correlation method or the matched filter method. However, the lightning signal is time-space random and mostly uncertain (see typical lightning pulse description in the section 1.3). Therefore there is only the option to use the signal energy to detect the lightning. That approach is examined in the following paragraphs 2.4.1 and 2.4.2.

[oscilloscope_trigger]

2.4.1 Using the oscilloscope to generate a recording trigger

Because the initial use of a VLF antenna or magnetic loop seemed to be suitable for capturing lightning signals in the required quality. The additional search for trigger methods was focused on suitable signal-analyzing methods.

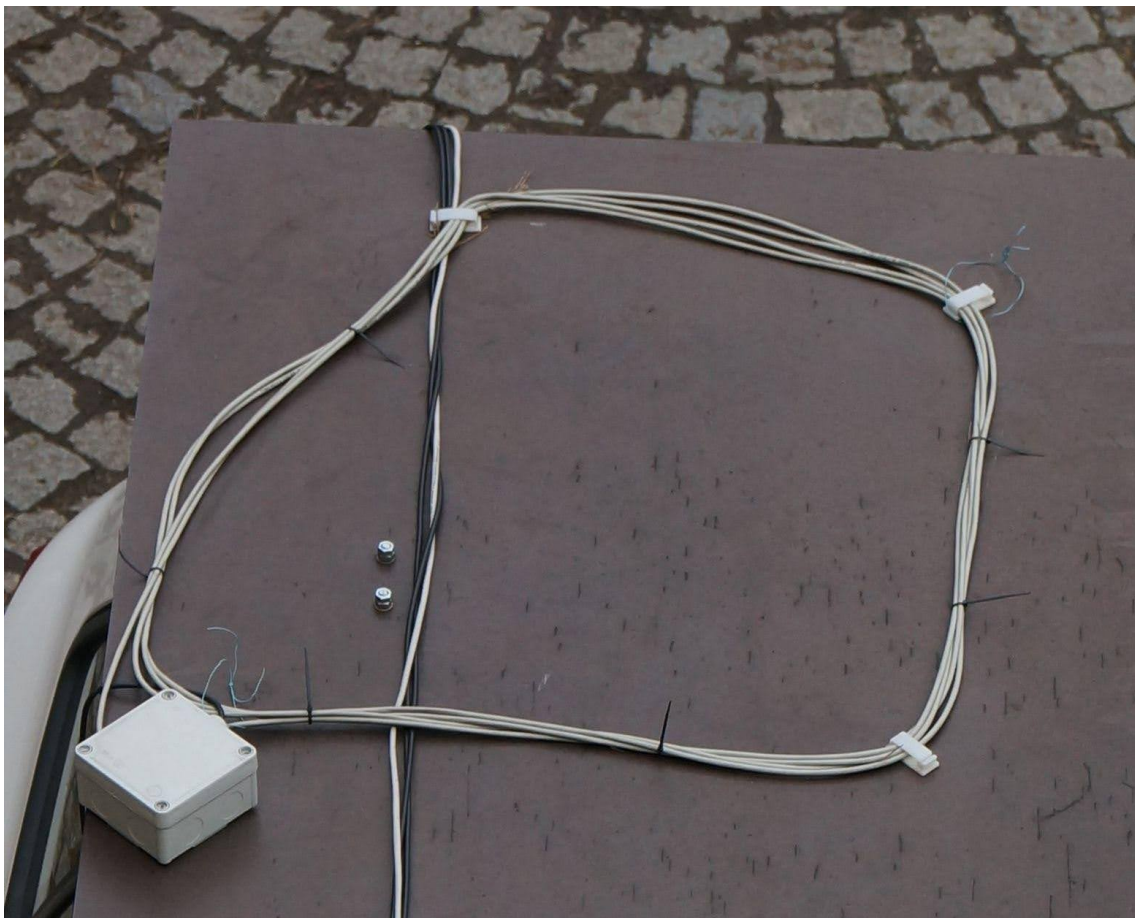


[mounted_oscilloscope]

Figure 2.8. Oscilloscope used for lightning-triggered recording on board of CAR1.

To address this challenge, a full-featured, fast desktop oscilloscope equipped with deep memory and sophisticated trigger settings based on signal characteristics was utilized. Initially, a simple VLF antenna made of UTP cable loop, originally developed

for the Ionozor project, was connected to one of the oscilloscope channels. The antenna design was based on the use of a VLFANT01 module, with the 10 m length, STP cable coiled into four loops (STP antenna). The STP antenna loops were placed horizontally directly at the plywood base mounted on the car roof. See Fig 2.9. for details. The oscilloscope was mounted on the back seat of the car by an ISOFIX base and directly powered by a stack of Li-pol batteries totaling 96 V. That solution was selected to completely avoid the possibility of noise generated from the onboard 230 V switching power supply in the testing car. Subsequently, various trigger settings on the oscilloscope during thunderstorms were tested. The most effective setting turned out to be one that activated the recording (oscilloscope trigger output) based on a combination of threshold level and pulse length. This result is logically justified by the fact that a lightning discharge is a high-energy event involving charge transfer over a significant duration. In a basic explanation, the height of the observed pulse corresponds to the rate of change in the magnetic field, and the duration corresponds to the charge being transferred. That trigger setup proved itself immune enough that the oscilloscope could be also later powered by 230 V power generated from 12 V car onboard power by switching the power supply, despite the fact the signal recording itself was heavily affected by interference coming from that power supply. Another advantage of that oscilloscope-based setup was this trigger setting ultimately allowed for the recording of the full length of the lightning discharge signal for up to a few seconds. However, the price for such a possibility was a long storage time corresponding to many minutes of dead time. The information gathered from these experiments and subsequently obtained from the recorded signals led to questioning of the assumptions stated in the introductory chapter. According to the structure of the signal, it was clear that the event was neither temporally nor spatially limited as described by assumptions based on literature and described in section (Introduction). To confirm this suspicion, however, it was necessary to obtain further supporting data, which led to the need to use an additional range of instruments and to mitigate the large dead time introduced by oscilloscope recording.



[loop_antenna]

Figure 2.9. The one of initial variants of STP loop VLF antenna mounted on the measuring car CAR1 has a resonant frequency of 100 kHz. Its signal was directly sampled by an oscilloscope placed inside the car.

[manual_trigger]

2.4.2 Manual trigger method

Although the trigger solution implemented with an oscilloscope proved relatively effective, it has certain drawbacks. One of the main limitations is the necessity to set the pulse level and pulse length parameters for each storm, and sometimes even for each phase of the storm. This characteristic resulted in the omission of some visible lightning events, which the operator in the car was able to see, but the oscilloscope did not trigger. Although this disadvantage can be theoretically eliminated by using the **force trigger** button on the oscilloscope, such a solution was uncomfortable and also assumed that the oscilloscope was already booted up and set to the appropriate mode at the time. It thus appeared that a probably more suitable solution would be to add a button for manual trigger operation for all devices, regardless of oscilloscope state. That was achieved by adding a button to the car's gear lever as is depicted in the photo 2.10. This manual approach not only allows the triggering of instruments before the oscilloscope is set, but it is also a comfortable solution for the driver to trigger while driving in a storm, where the driver often sees lightning in the storm, but resetting the oscilloscope while driving is not possible, as it would also have to dynamically change with the approaching storm.

Experimentally was also tested on a solution where multiple people sat in the vehicle, each visually monitoring their sector for the occurrence of lightning with a button in hand. That experiment has the result that the increase of sensitivity of multiple people

is not proportional to the increased manpower required. However, this visual-based manual approach has multiple effects on recorded data. One of them is the significantly decreased sensitivity of the human-generated trigger during daytime storms. There are even daytime storms where a person is unable to detect the occurrence of lightning discharges, but the trigger from the oscilloscope is recorded. Another effect, or perhaps more accurately a characteristic, is that such an implemented trigger is selective and lightning detected by this method contains a higher proportion of return strokes.



[Manual_button]

Figure 2.10. Manual triggering button mounted on manual gear lever suitable to be operated by the car driver during the thunderstorm.

The exploration of the manual and oscilloscope-based triggering methods has concluded that the most suitable solution is a combination of an algorithmic approach based on comparing the pulse height to a threshold and measuring its minimum duration before a trigger is executed. Additionally, a manual trigger is required to cover edge cases where the algorithmic trigger is not yet well-calibrated, but there is clear evidence of lightning. The specific implementation of the algorithmic trigger is discussed in subsequent chapters 3.2. It also takes into account the fact that the time delay incurred by using a manual trigger is less significant than the overall duration of the lightning. Therefore the resulting delay is not predetermined by a specific phase of the lightning, where the trigger will respond to.

[instrumentation]

Chapter 3

Proposed Instrumentation

To be able to record the different processes occurring during thunderstorms, the three cars were equipped with specialized measuring equipment. The aim is to verify the hypotheses considering the relation between thunderstorms and ionizing radiation stated in the 3.3 section because these cars were able to move to locations with predicted storm activity and thus flexibly react to specific storm developments, and perform ground measurements directly at the lightning site.

To determine the necessary parameters of lightning activity (lightning events' timestamps, lightning type, and location), the measuring cars, see Fig. 3.1 (CAR0 and CAR1), was equipped with high-speed all-sky camera and radio receivers. The cars were used to transport and power the instruments in proximity to thunderstorms, and the car cabin also served as partial protection for the instrument operator.

The equipment of cars is not uniform as it is gradually improved and also the purpose of each car slightly differs.



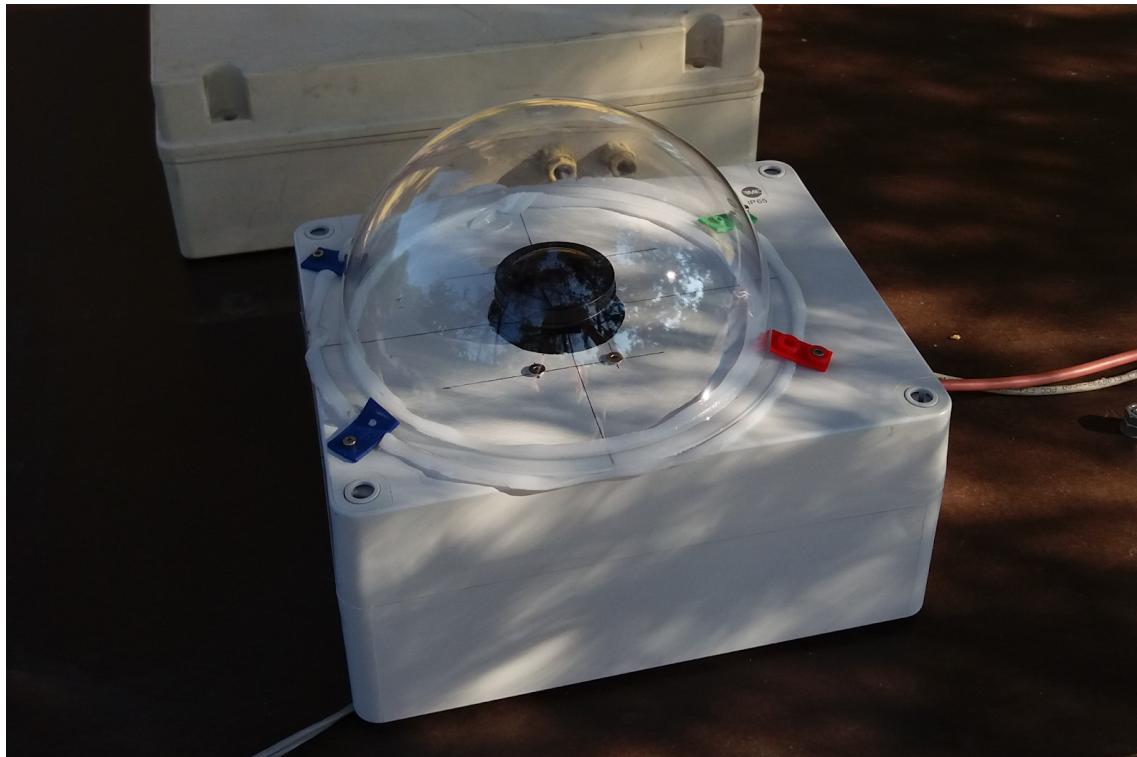
[CRREAT_CAR0]

Figure 3.1. Measuring CAR0 with instruments mounted on the roof platform. Other cars were equipped similarly. The differences in instrumentation are depicted in diagrams.

3.1 High-speed all-sky Cameras

The two cars were equipped with high-speed all-sky cameras. Their purpose is to capture the lightning event evolution in parallel with recording from the other instruments, especially radio receivers.

Chronos 1.4 camera CR14-1.0-16M [80] was mounted in a waterproof SolidBox 69200. The box is covered with a plexiglass dome with the manufacturer designation Duradom 200mm depicted in Fig 3.2.



`speed_allsky_camera]`

Figure 3.2. The camera has a wide-angle CS camera lens and is equipped with an IR blocking filter mounted in front of the LUX1310 CMOS sensor¹. The IR filter is mandatory, to avoid the adverse effect of sunlight coming into the camera lenses.

The video resolution of the camera was set to 928x928 pixels with 1612.33 FPS and a constant shutter in the range of 4.9 to 34 μ s during daytime thunderstorms and a maximum time of 614.6 μ s for nighttime thunderstorms. The shutter time was set by the instrument operator depending on current weather conditions and the available brightness dynamics of the high-speed camera. The video-saving length of the camera was set to 2 or 3 seconds. The video save format was initially H.264 resulting in MPEG-4 (.mp4) video, which sacrifices a bit of the quality for better compression. Lately, I found a method to record the 12-bit raw data from the camera without significantly increasing the data recording time.

The camera lenses used were FE185C057HA-1 [81]. The high-speed camera is therefore mainly sensitive to visible light. That spectral baseband was selected to minimize the absorption of light generated by lightning in the atmosphere.

¹ https://www.luxima.com/product_briefs/PDF/LUX1310_brief_v3.1.pdf

[radio Receivers]

3.2 Radiofrequency receivers

Radio receiver implementation has several iterations, from the initial overview recordings made with an oscilloscope to a dedicated solution utilizing an antenna array, allowing for a greater number of lightning strikes to be recorded. One of the compromises that had to be addressed in the design of the radio receivers was the choice of the received band. This is limited both by the physical properties of the lightning discharge and by the frequency band allocation table in the EU, as bands with continuous broadcasting are unsuitable for radio observations. At the same time, there are sizing restrictions on the car roof platform, which favors the use of a combination of VLF for detection and UHF for more precision mapping. The observational band is chosen according to the segment of interest in the lightning discharge. Broadly, the following bands that can be used for observing lightning discharges can be distinguished:

- VLF - Probably the most utilized from the view of the number of stations globally existing. The band is suitable for observing radiation generated by the main lightning channel. It is not well suited for measuring inter-cloud discharges.
- VHF - This band allows the reception of signals generated by initial breakdowns and some subsequent channels. On the contrary, it is not very sensitive to the main lightning channel [82–84].
- UHF - The band almost exclusively contains information about the initial breakdowns in the early phases of lightning development. The main lightning channel in this band is difficult to observe except at short distances.

That fact also favors the combination of VLF and UHF, because the primary interest was set to detection of lightning and then observing the lightning initiation point in coincidence with ionizing radiation.

3.2.1 Recording trigger implementation

As has been already stated, practically all current systems [57] detect and locate lightning based on the occurrence of a pulse signal above a specified threshold value. The absolute time of pulse detection is processed, using algorithms based on the Time Difference of Arrival (TDoA) possibly enhanced by a combination with directional findings. The calculated output is the most probable place of the pulse signal's origin. Only a minority of implementations consider the shape of the pulse or a sequence of pulses for a more detailed analysis of the signal's origin (excluding the correction of pulse dispersion to correct the TDoA value, which is quite common)².

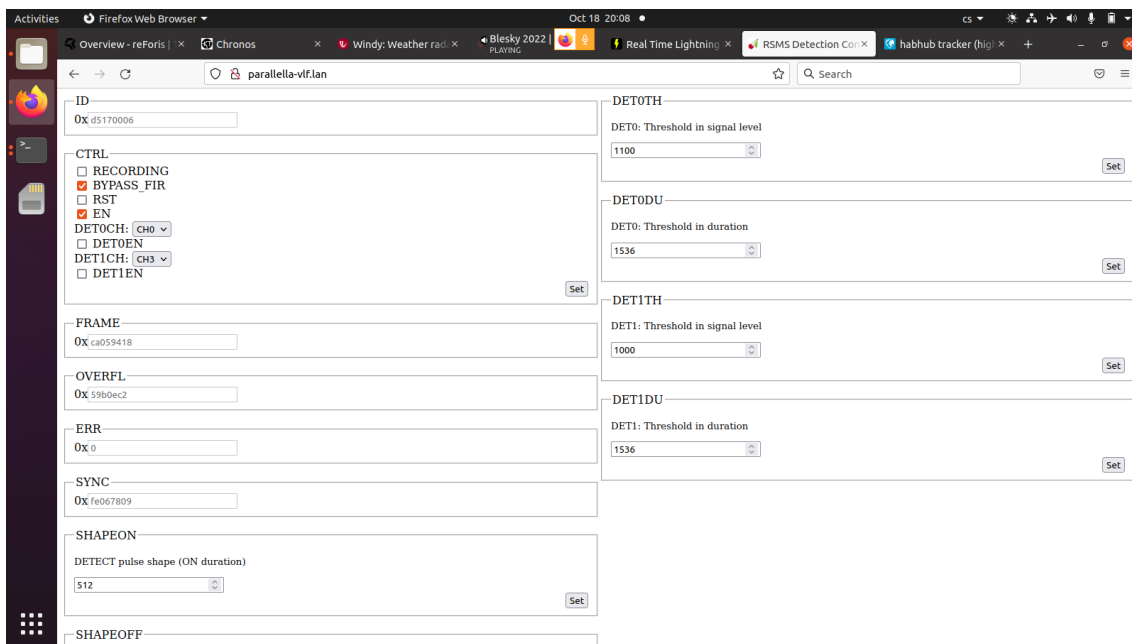
To clarify the phenomena occurring during a lightning discharge, it was necessary to adopt a different approach and implement a device with different properties from existing systems. The fundamental differences from other systems include:

- The entire segment of the lightning event signal with a bandwidth of 10 MHz is recorded, which is nearly double the bandwidth of the most of currently used solutions.
- Each station uses an antenna array, which can be utilized in the future for advanced signal processing, thereby making it possible to obtain directional resolution.
- Thanks to directional resolution, stations can spatially and temporally separate individual observed phenomena.
- Recording the entire signal segment allows for a more precise reconstruction of the lightning discharge structure.

² <https://www1.gifu-u.ac.jp/~lrg/falma.html>

- Lightning discharge can then be described by vectors in the future instead of the current most common description by a point cloud.

For the observation, the VLF receiver system was used simultaneously for detection of the lightning and triggering other instruments in the cars. The detection of the lightning was based on pulse width and the signal level; both parameters were set by the operator during the thunderstorm event. The range of these parameters is usually 5 to 20 μ s for the pulse width and 10 to 30 mV for the signal level. The values are set directly to the registers of the signal processing FPGA into the receiver. For convenience, the values could be set directly in the web-based UI shown in Fig. 3.3.

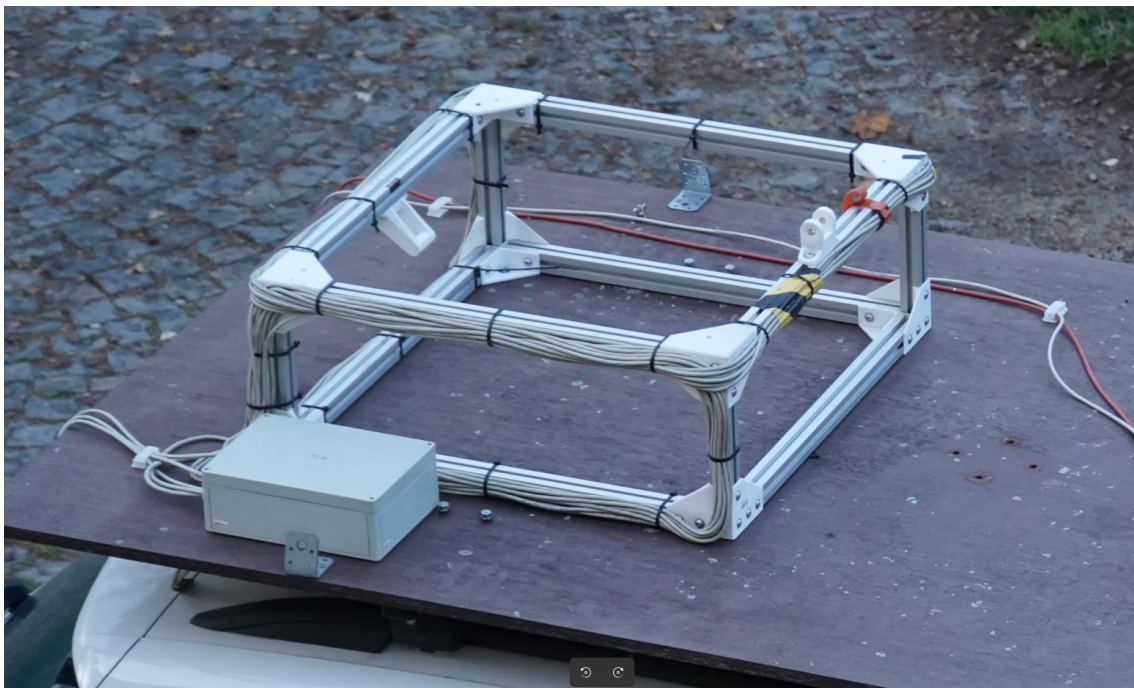


[RSMS_control]

Figure 3.3. Screenshot of the web-based interface to the VLF receiver used to set up the trigger and recording parameters.

[VLF_receiver]

3.2.2 VLF signal receiver



[VLF_antenna]

Figure 3.4. A detailed view on aluminum construction, that holds orthogonal magnetics loop antennas. The individual edges are isolated by 3D-printed corners.

The VLF signal receiver is based on a magnetic loop antenna and initially on a storage oscilloscope with a control computer for data readout. For one lightning event, that setup could record 800 ms of 8-bit samples with a sampling rate of 250 MS/s taking several minutes of recording time. From that concept which uses the antenna mounted flat on the plywood as depicted in figure Fig loop_antenna. In the dedicated receiver, the antenna array design was introduced, although it is based on the use of the same VLFANT01 module, with the 10 m length, STP cable coiled into loops. The antenna loops were attached orthogonally to the structure made from 40mm aluminum profiles mounted on the car roof. See Fig. 3.4 for details.

And the oscilloscope was replaced with very similar hardware as the UHF signal receiver described in the 3.2.3 section. The main difference is that the VLF antenna is directly coupled to the ADC inputs.

An example of the captured lightning signal can be seen in Fig. 3.5.



[figur_VLFdata]

Figure 3.5. Data visualization obtained from VLF antennas placed on three measuring cars (each car has a set of three orthogonal antennas). The amplitude and quality of the signal differ significantly. In the first rows, clear interference in the signal on CAR1 caused by switching power supplies is visible. The mutual trigger delay, caused by triggering different signal signatures, is also noticeable, complicating the capture of the entire lightning discharge.

The use of this dedicated receiver decreases the data recording interval to about twenty seconds and allows recording of the 1.45-second long signal fragment with 12-bit ADC resolution. Those parameters increase was a significant step from the original oscilloscope-based experiments.

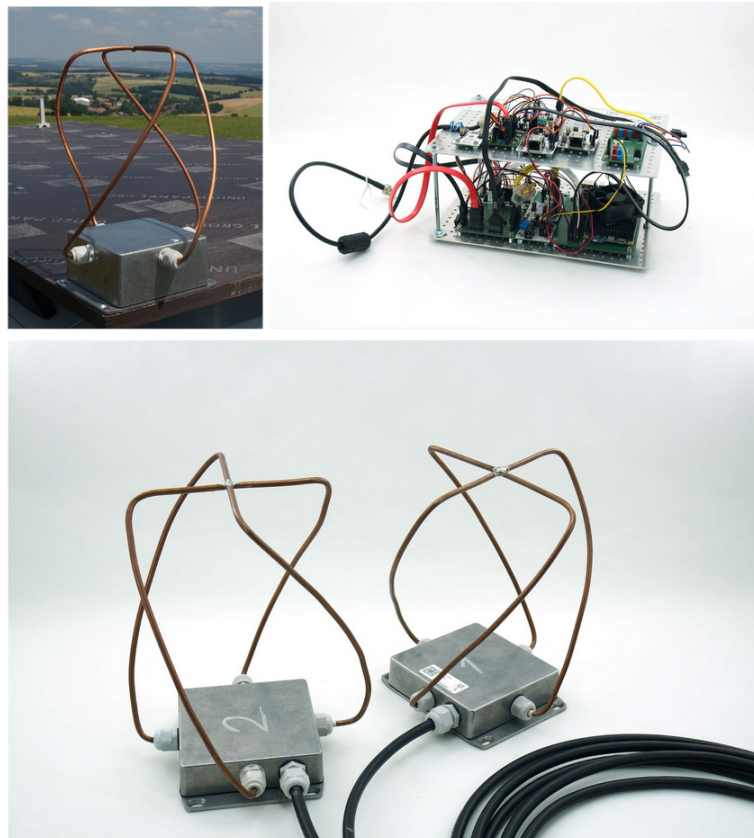
[UHF_signal_receiver]

3.2.3 UHF signal receiver

The construction of the UHF receiver is designed in a way that enables a phase processing of the signal from the antenna array with the aim of future detailed mapping of the lightning³. However, in the case of this experiment, only the scalar envelope of the radio signal is considered.

The UHF receiver operates approximately in the 370-406 MHz band, exact tuning depends on the local noise situation within the observation area. The receiver has 10 MHz bandwidth. The signal is received by an array of four QFH antennas mounted in a square-like configuration on the roof platform of the measuring car as is shown in the photos in Figure 3.6. The signal from each antenna is directly downconverted by an RF mixer to I and Q analog channels. Each channel is sampled by a 12-bit analog-to-digital converter with 10 MS/s.

³ <https://github.com/UniversalScientificTechnologies/RSMS01>



[UHF-QFH_receiver]

Figure 3.6. The platform mount of a QFH receiver antenna is shown in the top left corner. Detailed pictures of the antenna can be seen at the bottom and the receiver is in the top right.

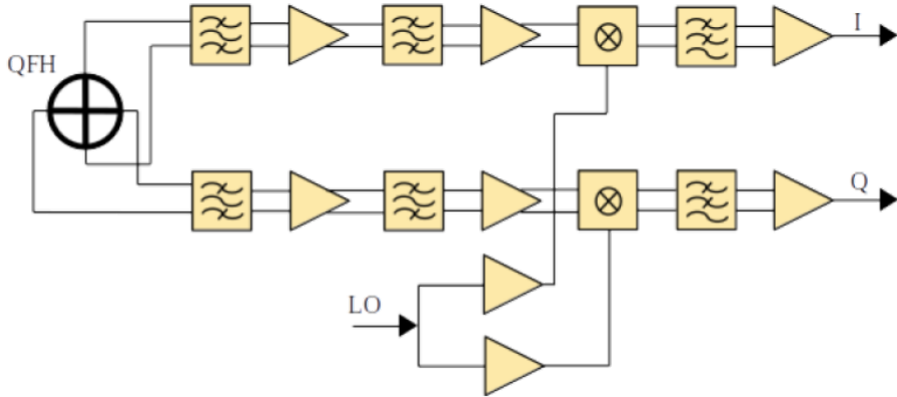
The block diagram of the receiver is shown in Appendix X

The UHF radio receiver is triggered by an external trigger (coming from the VLF receiver), then records a signal fragment with the configured number of pre-trigger and post-trigger blocks up to 1.45 seconds long in total. The radio signal is simultaneously sampled from all elements in the antenna array. This feature is achieved by using an internal ring buffer that stores the samples from the antenna array before the trigger. Time stamping is implemented by storing an array of sample numbers along with a few last-time marks created by a PPS signal from an external GNSS receiver. This metadata is then recorded in the resulting data record file for each trigger event. That mechanism allows precise restoration of the absolute time of each recorded signal sample.

The antenna array is mounted on an electrically non-conductive 18 mm thick plywood board attached to the roof of the measuring car by crossbars, located a few centimeters above the car's metal roof. Each element of the antenna array is based on the quadrifilar helix design. The Quadrifilar Helix Antenna (QFH) consists of two loops. Each loop end is connected in a manner that ensures a 90-degree phase difference between the loops, allowing it to receive signals from all directions without the need for orientation adjustments. This phase relationship is essential for achieving circular polarization, which is required for linear polarization orientation insensitivity (therefore typical application of that antenna is for satellite communication). The loops are arranged in a helical pattern to ensure that the received signal maintains a constant phase across the antenna's bandwidth. This design effectively enhances its performance for applications requiring consistent omnidirectional coverage, which is the situation of lightning detec-

tion. That technical feature at the same time allows the direct processing of the signal from the antenna as quadrature I/Q data.

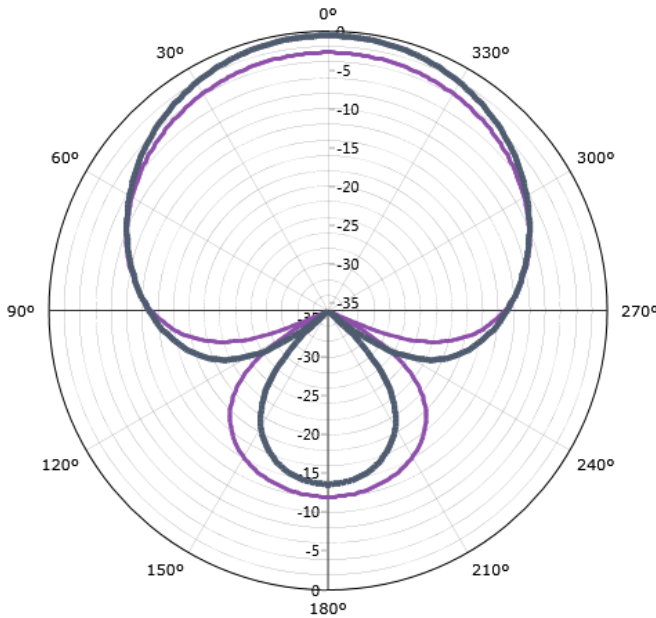
The phase difference of the QFH antenna is extensively exploited in the UHF receiver construction because the actual antenna realization used two loops, which are mechanically joined together on the loop midpoint (to achieve better mechanical rigidity), and loop ends connected to the active analog fronted PCB of the antenna (QFHMIX01) on the other side. QFHMIX PCB is mounted in a metal enclosure made from aluminum alloy. The antenna half-loops pass through the enclosure wall by waterproof cable glands. Each joint of the half-loop and QFHMIX01 PCB is considered to be a $40\text{-}50\ \Omega$ port. Therefore two single ports with 180° phase shift can be considered as one differential line of approximately $100\ \Omega$. In this case, the QHA antenna has two loops with $100\ \Omega$ differential output ports with phase shift 90° .



[IX_block_schematics]

Figure 3.7. Block diagram of active antenna RF-front end. In the left part, the phase-shifted terminals of the QFH antenna are connected, followed by the analog branches for processing I and Q signals.

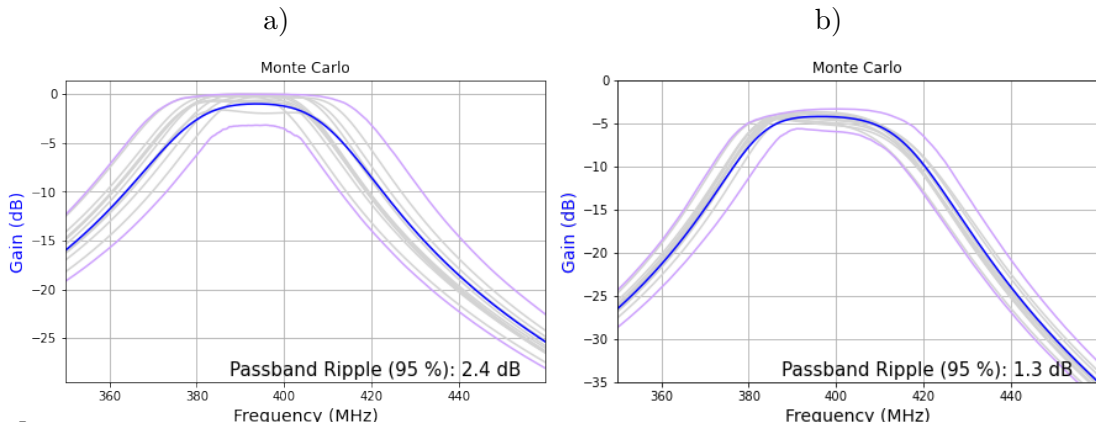
From that perspective, the QHA antenna itself functions the same as an I/Q demodulator. The signal on each port has a 90° signal phase shift in relation to the next port and QFHMIX01 is actually UHF analog front-end. The internally has two signal lines, one for I and Q signals. Each line contains LNA, mixer, and ADC buffer. The front end also contains a local oscillator amplifier (clock buffer) and power stabilizers. In total the PCB of the QFHMIX01 module has two differential 100Ω input ports for the antenna, one differential LVPECL input for the LO signal, and two 100Ω differential outputs for I and Q signals to ADC. It should be noted that LVPECL logic was selected for LO to minimize electromagnetic interference radiated back in antenna loops. The block schematics of the QFHMIX01 active antenna front-end are depicted in fig.3.7.



`a_radiation_pattern]`

Figure 3.8. Calculated vertical radiation pattern of the single QFH antenna in two perpendicular cross-sections (normalized).

The LNA structure contains the blocks concatenated from the antenna input port to the I/Q demodulator input in this way: first BPF, gain block, second BPF, second gain block. First BPF is the filter, whose purpose is to cut out the signals outside of the band of interest, and thereby protect the first gain block from overdriving to a nonlinear regime. The filter passbands are depicted in Figure 3.9.



`[input_RF_filter]`

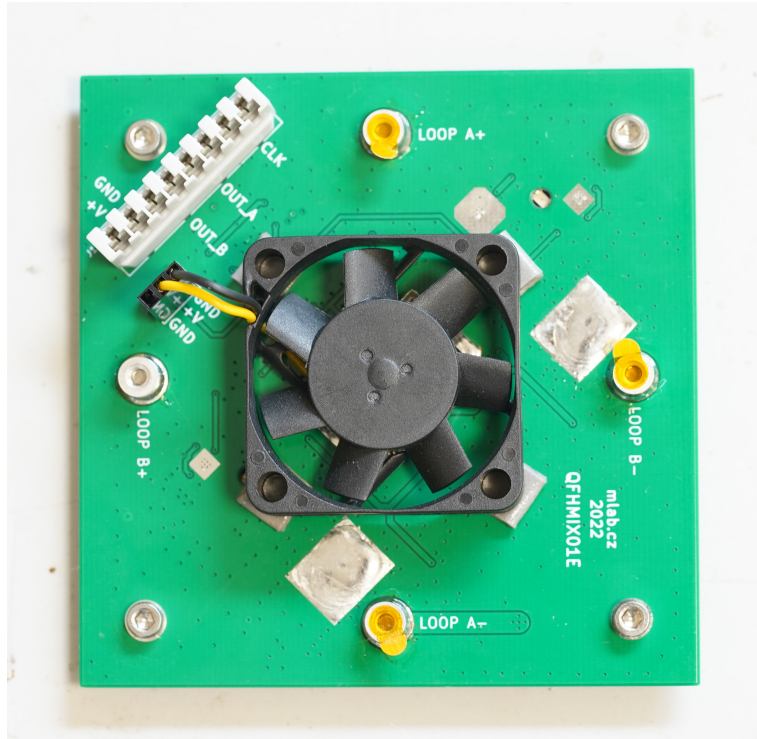
Figure 3.9. Monte Carlo analysis of two RF filters. a) The filter placed immediately after the antenna is a two-stage filter designed to maintain low insertion loss. b) The filter located after the first amplifier is a three-stage filter designed to limit the propagation of out-of-band signals further into the receiver. Both filters are designed using discrete E24 series components, which effectively minimize the possibility of detuning due to vibrations in mobile applications and enable the filters to achieve very compact sizes.

The first gain block is based on the MPGA-105 selected for minimal noise figure and high third-order intercept point, specifically, it has NF: 1.8dB, gain: 14.6 dB, and OIP3: 35.8 dB. The second filter is the band pass filter. The second gain block uses the MGVA-63 selected for acceptable noise figure and high gain while maintaining a wide dynamic range, it has NF: 3.6dB, gain: 21.5 dB, and OIP3: 34.3 dB. This sequence of components gives an RF path with approximately NF: 4.8 dB and gain: 32 dB.

The purpose of the mixer is to convert received signals into the ADC sampling bandwidth. The mixer is based on the AD8343 from Analog Devices. The local oscillator input of the mixer is connected to the clock buffer. The signal output is connected to the ADC buffer. A clock buffer is needed for the conditioning of local oscillator signals distributed by the antenna cabling from the UHF receiver base station. The used clock buffer is the Si53322 low-jitter dual output. Each output is used to feed Q and I line mixers separately. The I/Q signals, which are on the mixer output, need to be connected to the ADC input. To avoid aliasing on ADC it is necessary to pass signals through the LPF to cut off the higher frequencies. For that case, a 5MHz bandwidth LT6604-5 from Analog devices was chosen. It is also an amplifier for I/Q signals, which allows direct distribution by the UTP cable from the UHF RF front end to the base station inside the car. The output of the amplifier is the 100Ω differential pair, which perfectly matches a twisted pair from the UTP CAT 6 cable.

PCB is produced from the 1.6mm thick FR4. All components, excluding connectors, are SMD mounted from a single side. The RF blocks are carefully separated into different zones to avoid cross-talk. The RF parts are soldered on the bottom side of the PCB. The top side is a shielding GND layer with some signal jumpers and power voltage tracks.

The frontend outputs I/Q signals, local oscillator signal, and power supply are connected to the one IDC381-8-110 punch-down KRONE connector on the top side of the PCB. This connector is the main interface between the RF front end and the receiver base unit mounted in the car.



[QFHMIX01E_PCB]

Figure 3.10. Because the design of the QFHMIX01 is optimized for high dynamic range and low noise figure, these tradeoffs result in relatively high power dissipation. The PCB must therefore be equipped with a fan to provide cooling for the analog RF part.

It is worth noting that most of the available RF components were chosen to ensure that the design can operate across a wide range of frequencies without significant modifications. Specifically, to retune to a substantially different frequency, it is necessary to

replace the conductive structure of the antenna loops and retune the input RF filters in the QFHMIX01. This approach allows for the easy assembly of a system that can operate anywhere in the range of 40 MHz to 1 GHz. Additionally, these changes can be implemented on existing manufactured units, allowing the same equipment to be used in subsequent experiments without substantial investments.

ionizing_radiation_detectors]

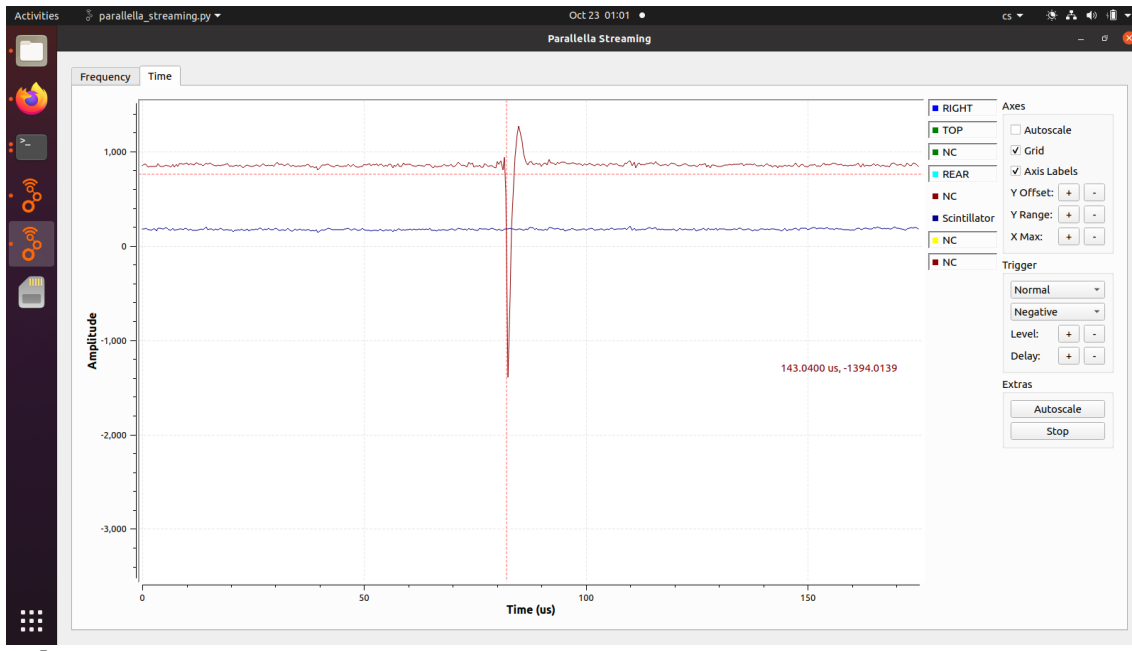
3.3 Ionizing radiation detectors

During the research, scintillation, and silicon semiconductor ionizing radiation detectors were primarily used. The scintillation detectors comprised a combination of NaI(Tl) scintillator and Silicon Photomultiplier (SiPM) sensors to eliminate the potential influence of magnetic effects from lightning discharges on the detectors. The detector's design was derived from the existing AIRDOS detectors in the case of semiconductor detectors and AIRDOS-C [85] for scintillation detectors. These detectors were an almost instant solution to cover a broad deposited energy range from 200 keV to 40 MeV with a time resolution down to 100 μ s for high-energy events ($>1\text{MeV}$), ensuring detailed temporal and spectral analysis of ionizing particles. For lower energies, only 15 s integration of events is provided.

Newly derived scintillation detectors GEODOS01 and GEODOS02 had scintillation crystals with a diameter of approximately 18 mm and a length of 30 mm. In addition to these newly developed detectors, the commercial RT-56 detectors were also operated on vehicles for a short period. However, due to their internal and unknown autocalibration, which is unsuitable for mobile measurements, they were subsequently moved to static observation sites. The identical construction of GEODOS01 detectors was then used at static observatories, similar to the RT-56 detectors. All these described types of detectors at static locations detected ionizing radiation related to thunderstorm activity. Specifically, the observation sites were Poledník and the Lomnický Štít observatory.

Unfortunately, the mobile deployment of these detectors in the measuring cars does not provide any significant detections of ionizing radiation, therefore the system was widened by the use of SPACEDOS with another silicon PIN diode to increase sensitivity. The G-M tube described in subsequent balloon experiments was also used for a short time, but none of these sensors were able to indisputably detect ionizing radiation associated with storm activity. The causes of this situation will be discussed in the 5 section, but one of the most obvious possibilities that could have been eliminated during the research was the fact that the NaI(Tl) crystal with SiPM and preamplifier was shielded in a metallic box made of steel sheet with a wall thickness of about 0.5 mm. Additionally, all these ionizing radiation detectors were placed inside a car, which also had a steel roof with a thickness of about one millimeter. This shielding was chosen out of concern that the detectors would be affected by electromagnetic or even acoustic manifestations of storm activity (as ionizing radiation detectors are known to have significant microphonic effects). On the other hand, such an approach could partially shield the ionizing radiation or worsen its detectability. For example, the interaction of gamma rays with metal parts could create electrons that might not have been detectable in background noise due to their relatively low energies. Towards the end of the research, this approach was reassessed, leading to the design of another ionizing radiation detector. In this latest design, a larger NaI(Tl) crystal was optically coupled with a USTSIPM01 module, whose electrical signal output is connected via a balun transformer to a spare ADC channel of the previously described VLF receiver. The result is a device capable of recording individual ionizing radiation interactions in the

NaI(Tl) crystal around the lightning discharge trigger. The maximum recording length is identical to the length of the recorded VLF signal fragment and it is also time-aligned. The image (fig scintillator_pulse) shows an example pulse resulting from cosmic radiation outside of storm activity. Unfortunately, this approach was implemented towards the end of the measurement season, during which cars were available. Consequently, there is very little experimental data, therefore this potential improvement of sensitivity was not adequately examined.



[scintillator_pulse]

Figure 3.11. Example of an analog pulse from a silicon photomultiplier (USTSIPM01 module) that is digitized by a free channel on the ADC of a VLF receiver. The pulse is probably caused by a muon from cosmic rays.

3.4 Electric Field Sensors

Electric field sensors were planned to be used as devices capable of indicating the potential for lightning discharges in clouds. For this purpose, Boltek detectors were initially acquired and Boltek detectors were used for ground-based measurements. Despite their widespread use, these detectors presented significant limitations for mobile measurements due to their bulkiness and less optimal design for mobile deployment. Seeking a more adaptable solution, the more compact Kleinwächter EFM 115 was transitioned to. This Electric Field Mill (EFM) offered an improved form factor for mobile applications, directly connecting its analog signal output to a data logger equipped with a GPS for accurate timestamping⁴, with a logging time resolution of 110 ms.

However, challenges persisted with the Kleinwächter EFM 115, as its mechanical and weather durability did not meet the demands of mobile fieldwork, and the quality of its data output sometimes fell under the required quality. These obstacles resulted in the necessity for an alternative solution, prompting the development of a new design for electric field mills. The new design also required increased versatility, because these custom mills were engineered to seamlessly integrate into stationary setups, mobile measurements utilizing vehicles, and even atmospheric assessments via Unmanned

⁴ <https://github.com/mlab-modules/FIELDMILL01>

Aerial Vehicles (UAVs), addressing both the mechanical robustness and data quality issues which were encountered with commercial alternatives.

For the construction of the new electric field mill (THUNDERMILL01), the initial design was first tested in a laboratory and then put on the measuring car roof, as shown in Figure 3.12. At that time, the mill was housed in a tin-plated can turned upside down to protect it from external weather influences. This solution proved ineffective, as the metal can rust through in approximately two months. Subsequent units intended for stationary placement at the Lomnický Štít observatory were therefore made with a stainless steel casing 3.13.



Figure 3.12. THUNDERMILL01 electric field mill housed in a tin-plated can, mounted on the roof of a car to test its performance and weather resistance in an outdoor setting.

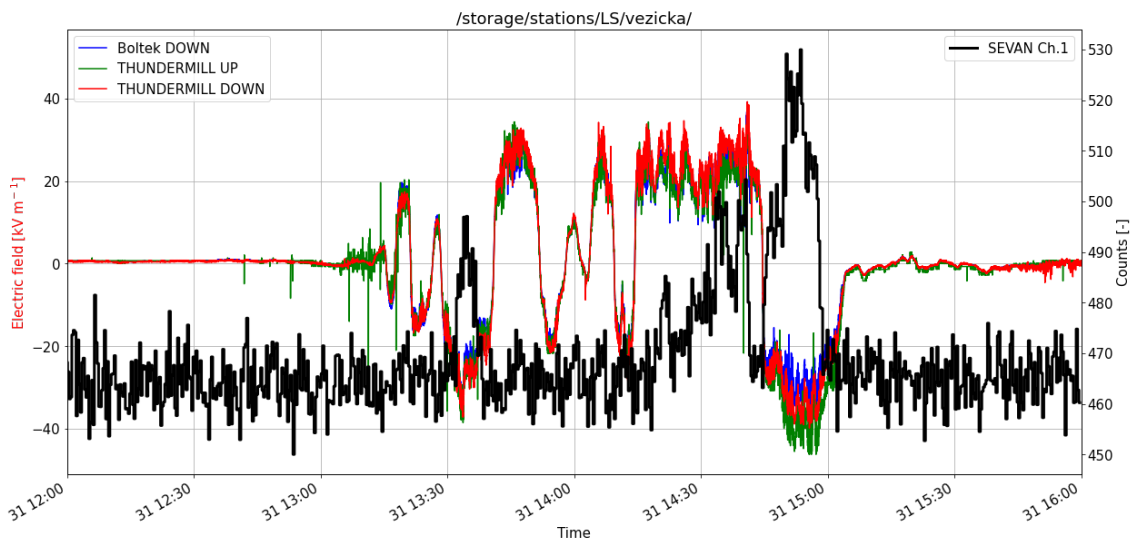
THUNDERMILL01_on_car]



[LS_THUNDERMILL]

Figure 3.13. Installation of THUNDERMILL01 at Lomnický Štit Observatory, the electric field mill is installed here in both down and up orientations. This experiment aimed to measure the charge of the hydrometeors to explain how the charge in the cloud is generated.

After testing on the car roof, there was a requirement to deploy the same electric field mill to the rotor head of the TF-G2 autogyro to measure the distribution of the electric field directly in the atmosphere. This placement can be seen in the image in the chapter 4.2, where the instrumentation is described in more detail.



JNDERMILL_LS_boltek]

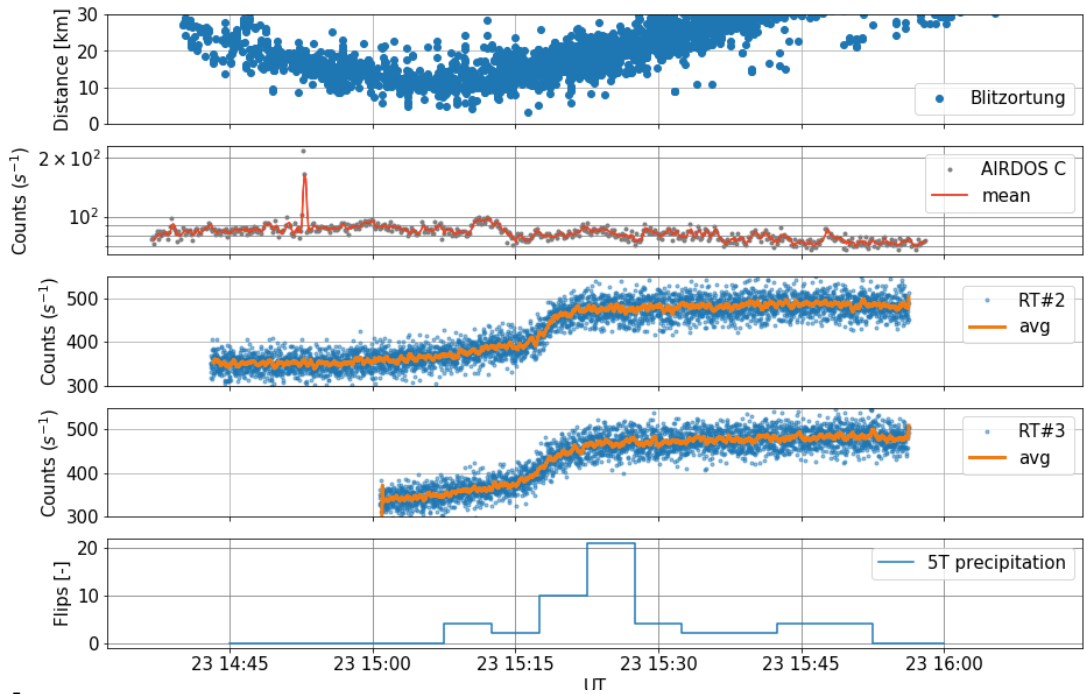
Figure 3.14. The graph shows a comparison of the UP and DOWN configurations of THUNDERMILL01 at the Lomnický Štit observatory. Additionally, it includes a comparison with the particle flux of ionizing radiation detected by the SEVAN detector, also located at Lomnický Štit. The electric field measurements are displayed for Boltek and THUNDERMILL instruments for comparison.

3.5 Meteorological instruments

To accurately assess the meteorological situation during thunderstorms, the measurement vehicles are equipped also with a set of standard meteorological instruments. These allow for the real-time monitoring of environmental parameters used for improved understanding of condition evolution. Below is an expanded overview of additional instruments, incorporating details from the provided references.

3.5.1 Disdrometer

The implementation of the disdrometer was necessitated by the need for high-time resolution measurement of precipitation patterns and their evolution. Precipitation is a key meteorological parameter for understanding the correlations between ionizing radiation and storm activity, because hydrometeors play a significant role in washing radon decay products out of the atmosphere, consequently creating a temporary increase in radiation background levels on the ground 3.15. High-rate precipitation data are necessary for distinguishing these events from occurrences of TGE.

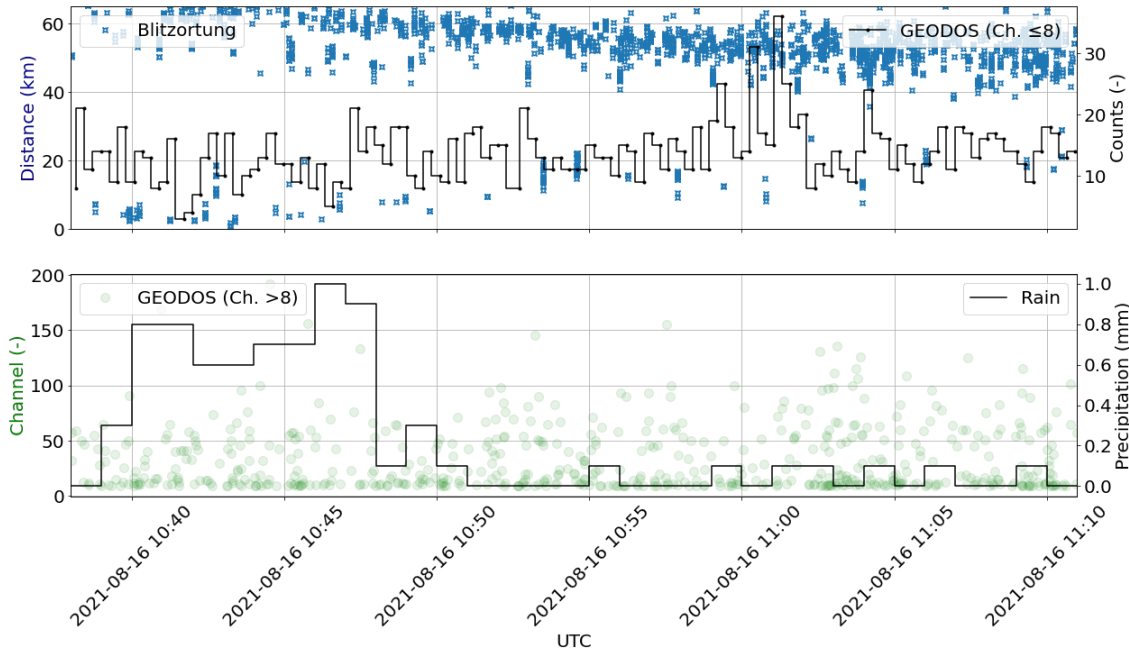


Radon_precipitation]

Figure 3.15. The graph demonstrates the impact of rainfall on ionizing radiation flux on the ground. The top panel shows the distance to lightning strikes (Blitzortung), while the subsequent panels display counts per second for different scintillation detectors (AIRDOCS C inside the car, RT#2 and RT#3 on the car roof). The final panel indicates precipitation intensity (5T precipitation). Notably, there is a clear increase in radiation counts following periods of rainfall, highlighting the washout effect of radon progeny from the atmosphere.

Traditional, widely used methods of precipitation measurement have their limitations. For instance, the commonly used tipping bucket rain gauge only provides data

resolution dependent on precipitation intensity and has a relatively narrow effective range where the collection bucket can tip and accurately measure rainfall.



`g_bucket_limitation]`

Figure 3.16. This graph illustrates the limitations of using a tipping bucket rain gauge. While there is a slight increase in radiation detected (around 11:00), the lack of detailed information on precipitation type and better temporal resolution makes it difficult to attribute this increase to a specific phenomenon.

Furthermore, the tipping bucket rain gauge does not differentiate between different types of precipitation^{3.18} (rain, snow, hail, graupels, etc.), which impacts the efficiency of radionuclide washout and also the electrification of storm clouds 3.16. It has a significant advantage in precise volume measurement of the precipitation, but it is a value that is not useful too much because rain intensity and hydrometeor type are more important. In contrast, the disdrometer—another type of instrument—is capable of identifying precipitation types but generally lacks precision in measuring volume. In the case of mobile measurement using cars, there is also a requirement to avoid optical principles, which most commercial disdrometers are based on, which are unsuitable for vehicle roof mounting due to their sensitivity to movement and vibration.

In response to these challenges, the (DISDROMETER01)⁵, was specifically designed for installation on a flat vehicle moving platform, enabling high-precision, real-time data collection during storm events. This instrument leverages SDR receiver technology previously utilized in the Bolidozor meteor detection network. It employs a piezoelectric element capable of detailed sensing of raindrop size distribution and intensity, from drizzles to heavy downpours.

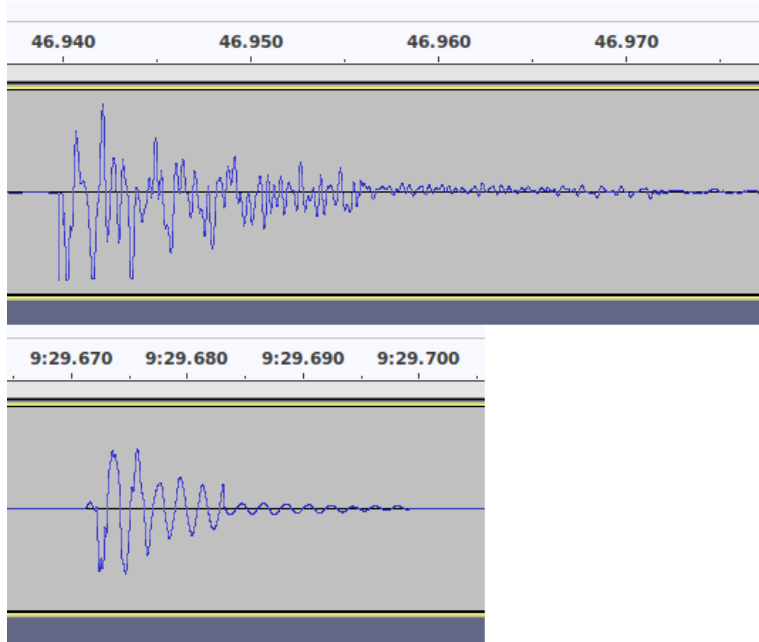
⁵ <https://github.com/UniversalScientificTechnologies/DISDROMETER01>



[DISDROMETER01]

Figure 3.17. Photograph of a DISDROMETER01 mounted on the roof of a car, featuring an open box that contains the piezo element, the primary sensing component of the device.

Technically the disdrometer captures sound waves generated by the impact of precipitation particles on the plastic enclosure 3.17, providing insights into the characteristics of rainfall during time.



[METER01_hyrometeors]

Figure 3.18. The graphs show the difference in signal responses between various types of precipitation, specifically illustrating the difference between rain and hail. The top image is a detailed view of the impact of a single hailstone and below a single raindrop.

■ 3.5.2 Anemometer

Given the necessity of knowing both the direction and speed of the wind during storm measurements, especially for launching unmanned aerial vehicles from the car rooftops and for overall safety in measurement, it was essential to equip the measurement vehicles with an anemometer capable of assessing these parameters in storm conditions. The development of the alternative anemometer was initiated in response to the failure of a standard cup anemometer during its first deployment on a highway drive. This unexpected failure highlighted the need for a device capable of enduring high-speed conditions (at least 130 km/h) in adverse weather, including wind and hail, without significant maintenance. Although the issue might have potentially been addressed by acquiring a high-quality professional anemometer, a more application-suitable design, with less aerodynamic drag was sought, given the intended use case. This pursuit coincided with efforts to develop a replacement for the Pitot tube for UAV applications (described in detail in section 4.2). Logical progression led to the use of similar technology for the anemometer mounted on a vehicle.

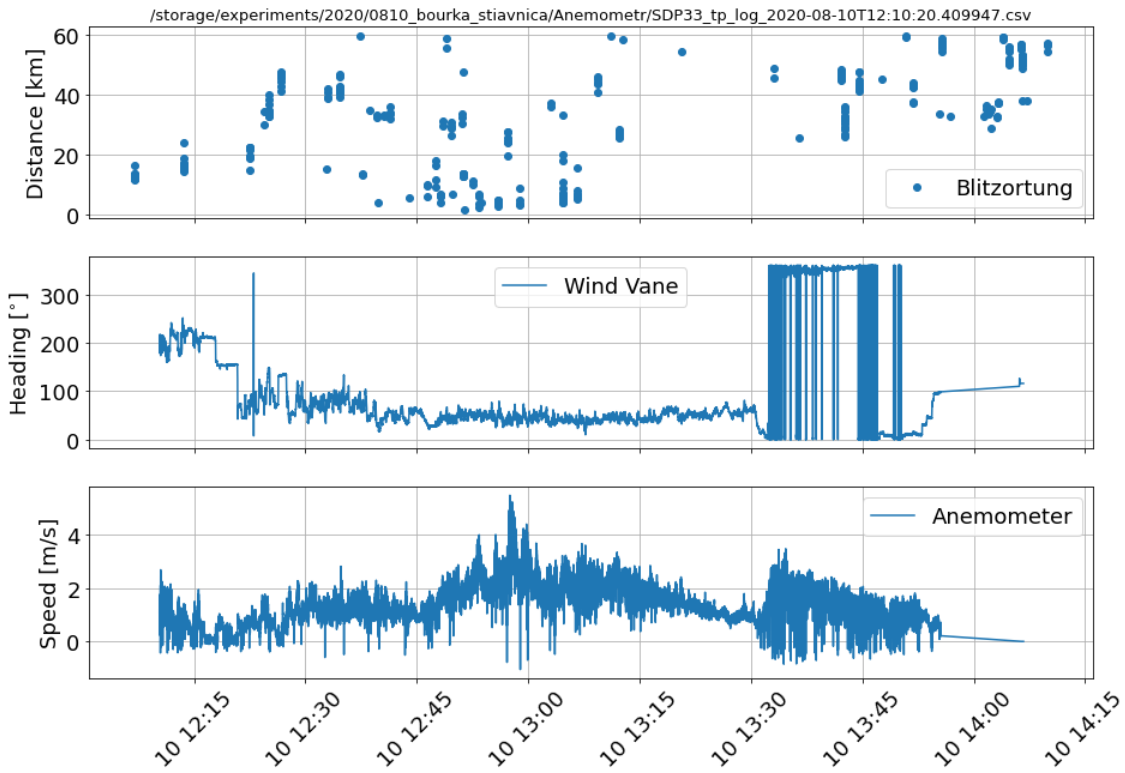


[WINDGAUGE03]

Figure 3.19. A photograph showing the installation of the WINDGAUGE03 anemometer on the car roof alongside a windsock.

The new anemometer's design benefits from the inclusion of a circuit board that not only accommodates a differential pressure sensor but also a magnetometer. This enables the measurement of absolute wind direction without the need for directional calibration against the actual vehicle's orientation, an advantage over conventional weather station setups that typically require fixed positioning relative to the north. Although the later integration of the RTK GNSS receiver in measurement car infrastructure (depicted in 4.20) partially reduces this requirement by eliminating the need for direction correction,

the WINDGAUGE03 anemometer has been used further due to its resistance to adverse weather conditions.

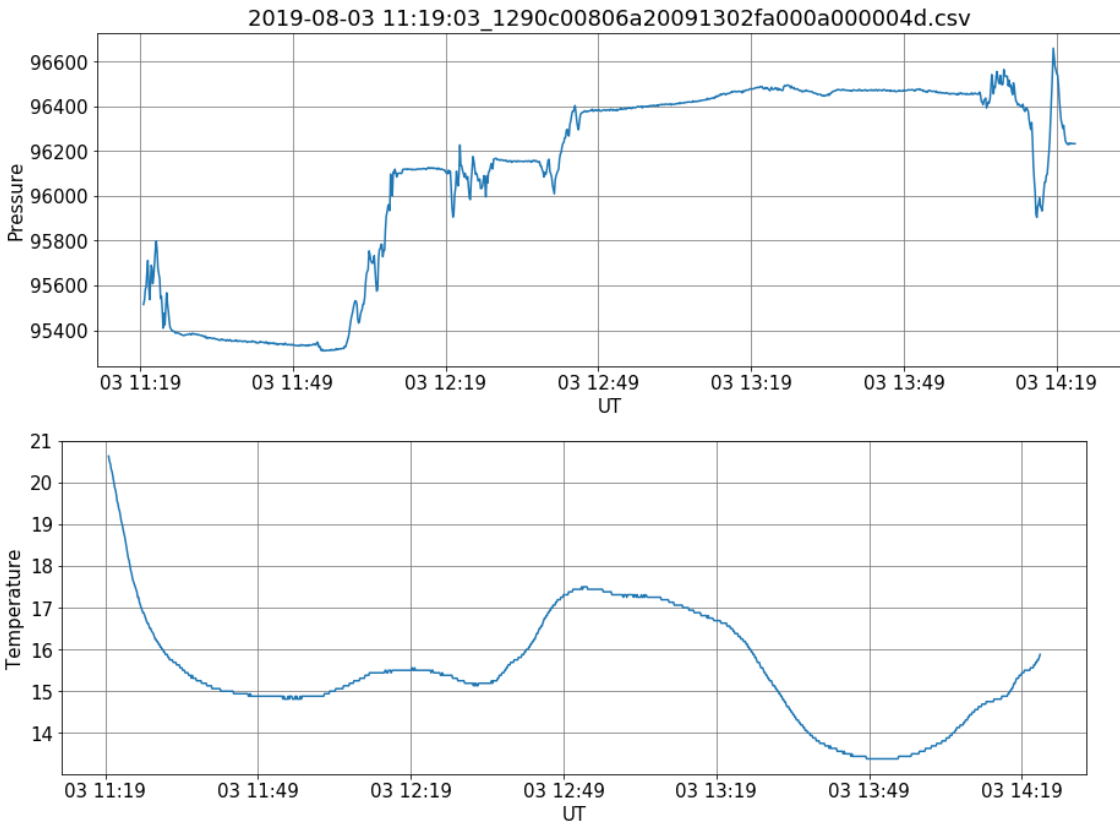


GAUGE03_measurement]

Figure 3.20. The graph illustrates data measured by the new anemometer WINDGAUGE03 at the edge of a storm. The top panel shows lightning strike data from Blitzortung.org, the middle panel presents wind direction measurements, and the bottom panel displays wind speed data from the anemometer.

3.5.3 Thermometer and Barometer

Temperature data is used in multiple ways, one of the most common is for eliminating possible temperature-dependent variations that might influence the sensors mounted on the car platform. For that purpose the MLAB ALTIMET01A module was used, which combines temperature and pressure sensing capabilities, providing an overview of the atmospheric conditions.



```
temperature_pressure]
```

Figure 3.21. The graphs illustrate the changes in temperature and pressure during the passage of a thunderstorm. As evident, both variables fluctuate throughout the atmospheric event, often in a discontinuous manner.

[experiments]

Chapter 4

Subsequent Experiments

After initial processing of storm activity records with the described instruments, it became apparent that some observations are difficult to explain solely with the data obtained so far. For instance, the finding of the extensive spatial and temporal scale of lightning discharges described in section 2 raised questions about the distribution of charges within storm clouds that the lightning connects. Similarly, ambiguities arose regarding ionizing radiation. The uncertainty lies in whether ground measurements missed ionizing radiation because the detectors were too far from the radiation source or because the radiation was emitted in a direction undetectable by ground-based detectors situated directly under the storm cell. To resolve these issues, spatial data on charge distribution and the radiation field are necessary, prompting the proposal of additional supportive experiments, which allow direct in-situ measurements in the atmosphere.

[balloon_flights]

4.1 Stratospheric Balloon Flights

Stratospheric balloon flights are conducted for several reasons related to the research of electromagnetic phenomena in the atmosphere associated with storm activity. They allow for the testing of instruments under various adverse conditions, enable the testing of data transmission methods over relatively long distances and in unfavorable weather, and provide a platform to lift additional instruments in the atmosphere. For example, they offer insights into the behavior of ionizing radiation in the upper layers of the atmosphere, where particles of primary cosmic radiation with sufficient energy interact and generate showers of secondary cosmic radiation. This phenomenon causes the situation, that with increasing depth of the atmosphere, the intensity of primary radiation decreases whereas the secondary component intensity increases. At an altitude of about 20 km, the intensity of secondary cosmic radiation reaches its maximum, called the Pfotzer-Regener maximum [Pfotzer, 1936; Regener, 1933; Regener and Pfotzer, 1935]. The maximum varies with geomagnetic vertical cutoff rigidity and with solar cycle and it is generally located at 15-27 km above sea level [Bazilevskaya and Svirzhevskaya, 1998]. Due to that physical phenomenon, Stratospheric balloons are a useful tool for the investigation of cosmic radiation at high altitudes (around and above the Regener-Pfotzer maximum region).

Since the composition of the radiation field varies with altitude [86] various radiation detector types should be used to measure the vertical profile of cosmic radiation in the atmosphere.

However, the radiation-measuring instruments need to be supplemented by other sensors measuring temperature, pressure, humidity, altitude, acceleration, etc. All these sensors should be continuously monitored during the launch and the flight of the balloon to verify their proper function and their values have to be recorded for further processing of all obtained data.

Therefore I proposed the development of the TF-ATMON¹ system, based on the use of existing tools of the open-source PX4 autopilot and supplemented with the new TFSIK01 telemetry transmitter. That enables on-ground monitoring of sensors and recording of data during the flight and at the same time real-time tracking of the balloon. This methodology was firstly used in full scale on stratospheric balloon flight FIK-6 4.2 and then improved in FIK-9 flight.

I have participated in the launch of multiple stratospheric balloons, the overview of flights is summarized in Table 1. At the beginning (until the FIK6 flight) the construction of balloon gondolas was designed for specific instruments used for particular flights. Balloon avionics was therefore built around the chosen detectors from scratch.

This concept led to a situation when every new flight meant a significant amount of work although many components were recycled every year and used for the next one. The reason was the need to adapt the avionics to the updated version of the detectors.

Due to a relatively high value of payload and measurement relied only on board data recording it was necessary to ensure the recovery of the gondola after every flight. Therefore the main criteria for the construction of the balloon experiment were as follows:

- Reliable transmission of information about the geographical location of the gondola
- Good resistance to impact
- Ensuring the function in temperatures far below zero

Despite the generally successful nature of all flights and the fact that the gondolas were always found, different technologies were tried to eliminate the partial shortcomings that emerged during the previous balloon flights. For example, the initially used GSM-based telemetry system was replaced by a significantly more robust IoT LoRa transmitter, making it possible to transmit the data necessary for tracing the gondola directly to TheThingsNetwork². This step enables a high reliability of finding the gondola and at the same time a basic recording of the experiment data transmitted to the ground. For the case of more advanced detectors, it was also necessary that the 3D flight trajectory including the orientation be recorded synchronously with the supplementary quantities. That is also ensured with the incorporation of the TF-ATMON system, which relies on PX4 autopilot firmware running on Pixhawk hardware equipped with IMU sensors. As can be seen from Table 1 in appendix C, flights conducted since FIK-5 implemented avionics using UAV technology. It is realized by the use of the Pixhawk-based autopilot hardware with PX4 firmware. Telemetry was implemented by a very reliable combination of the LoRa modem and SiK modem.

Apart from technologies used directly in balloon gondolas, many supplementary tools on the ground have undergone intensive development. For example, to find the balloon it was necessary to have an accurate real-time map of its position together with a prediction of the next stage of the flight and the location of touch down. For that case of the flights since the FIK-5 used the HabHub³ (lately the SondeHub⁴) was used to track and predict the movement of stratospheric balloons in real-time. In fact, in the beginning, the HabHub was used to manually run the prediction of flight, but the real-time calculation of trajectory predictions introduced in FIK-3 based on live telemetry data significantly decreased the time required for gondola recovery.

¹ <https://www.thunderfly.cz/tf-atmon.html>

² <https://www.thethingsnetwork.org/>

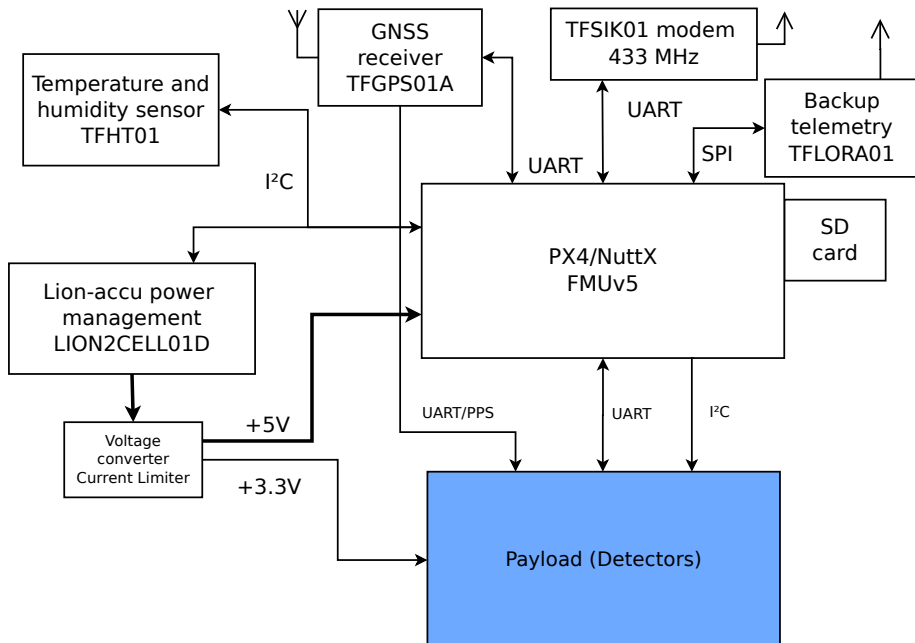
³ <https://tracker.habhub.org/>

⁴ <https://amateur.sondehub.org/>

4.1.1 The design of universal avionics

Based on the described experiences the concept of a universal avionics called TF-ATMON emerged. That technology makes it possible to connect different types of payloads and carry out various atmospheric measurements. Furthermore, it provides basic services such as power supply, time, position, and 3D orientation information to the payload instruments. That data is recorded in parallel with quantities that affect many types of measurements, including temperature, pressure, humidity, magnetic field, and acceleration. At the same time flight computer provide services for payload to record data from experiments in a common log file. Therefore the TF-ATMON onboard stratospheric balloons have become an extremely useful tool for testing instruments like cosmic radiation detectors and dosimeters at high altitudes.

The schematic diagram of the avionics hardware is summarized in the figure 4.1.



[avionics_schematics]

Figure 4.1. The schematic diagram of the new avionics concept used in FIK flights.

The concept, where the balloon-specific avionics are almost completely separated from the experiment set of detectors, simplified the realization of the next balloon flights. It reduced the complexity of connecting different types of detectors and at the same time, it improved the integrity of supplementary data measurements. Overall, the new features can be summarized as follows:

- Easy implementation of different payloads
 - Redundant telemetry links
 - Gondola orientation and spatial position tracking and logging
 - Reliable IMU sensor processing and calibration
 - Possible use of relatively high-power consumption payloads
 - Pre-flight continuous charging as an option

- Power monitoring and uptime calculation relevant to the actual temperature and available energy level
- Real-time pre-flight payload diagnostic

The detailed documentation of used electronics blocks can be found under the following names TFGPS01, TFSIK01, TFHT01, TFLORA01. It should be noted that the TFSIK modem has been designed after the long use of the MLAB electronic module ISM01, which has been its predecessor. In both cases, the SiK firmware used on the balloon has been altered to one-way (downlink) communication (therefore the modem on the balloon is not able to receive) for safety reasons.

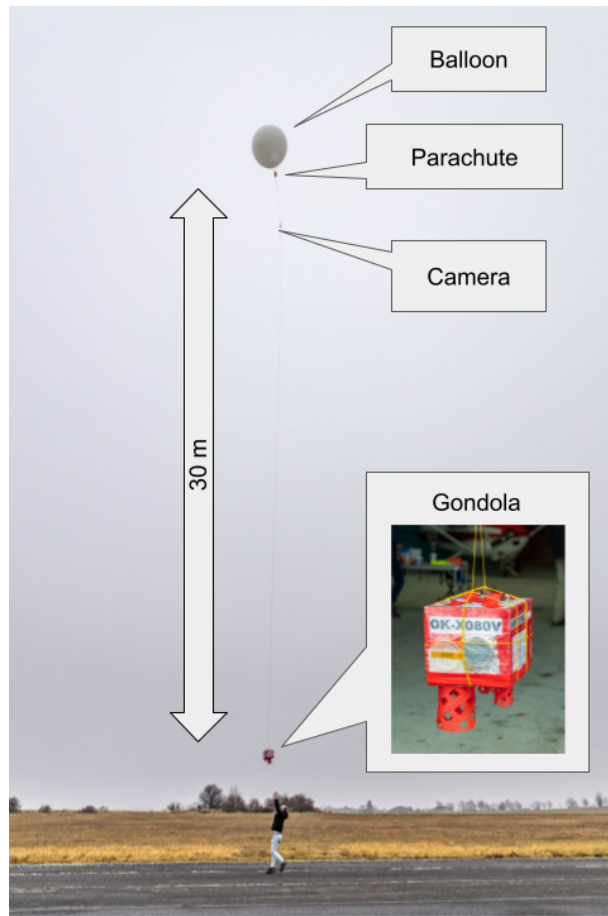
■ 4.1.2 Instrument payload

In the case of FIK-5 and FIK-6 flights that served as the test flights for the novel approach using TF-ATMON technology the payload was not fully relied on yet. All the detectors thus had their SD cards for data recording and some even had their power supply, therefore the payload weight was higher than theoretically required in case of full use of TF-ATMON and some lift was wasted. This situation originated in the conservative flight plan, which required a successful log and function of payload even in the failure of the new method.

■ 4.1.3 Atmospheric phenomena Detectors

The payload for example FIK-6 flight contained TF-ATMON and three different types of ionizing radiation detectors already mentioned in 3 section: SPACEDOS with silicon PIN diode sensor, AIRDOS-C with scintillation crystal and silicon photomultiplier and a G-M tube. The total payload mass was 2 kg.

SPACEDOS is a lightweight dosimeter intended for space applications and measurements onboard spacecraft. The detector has been described in [87]. AIRDOS-C is a scintillation detector with a small crystal. The detector has been described in [88]. The G-M tube STS-5 was used in the Geiger–Müller counter. This detector is capable of registering the flux only and is included, because it has high detection volume, which allows good resolution in flux. All detectors, together with other sensors and the TF-ATMON system were put inside a polystyrene box.



[FIK-6_setup]

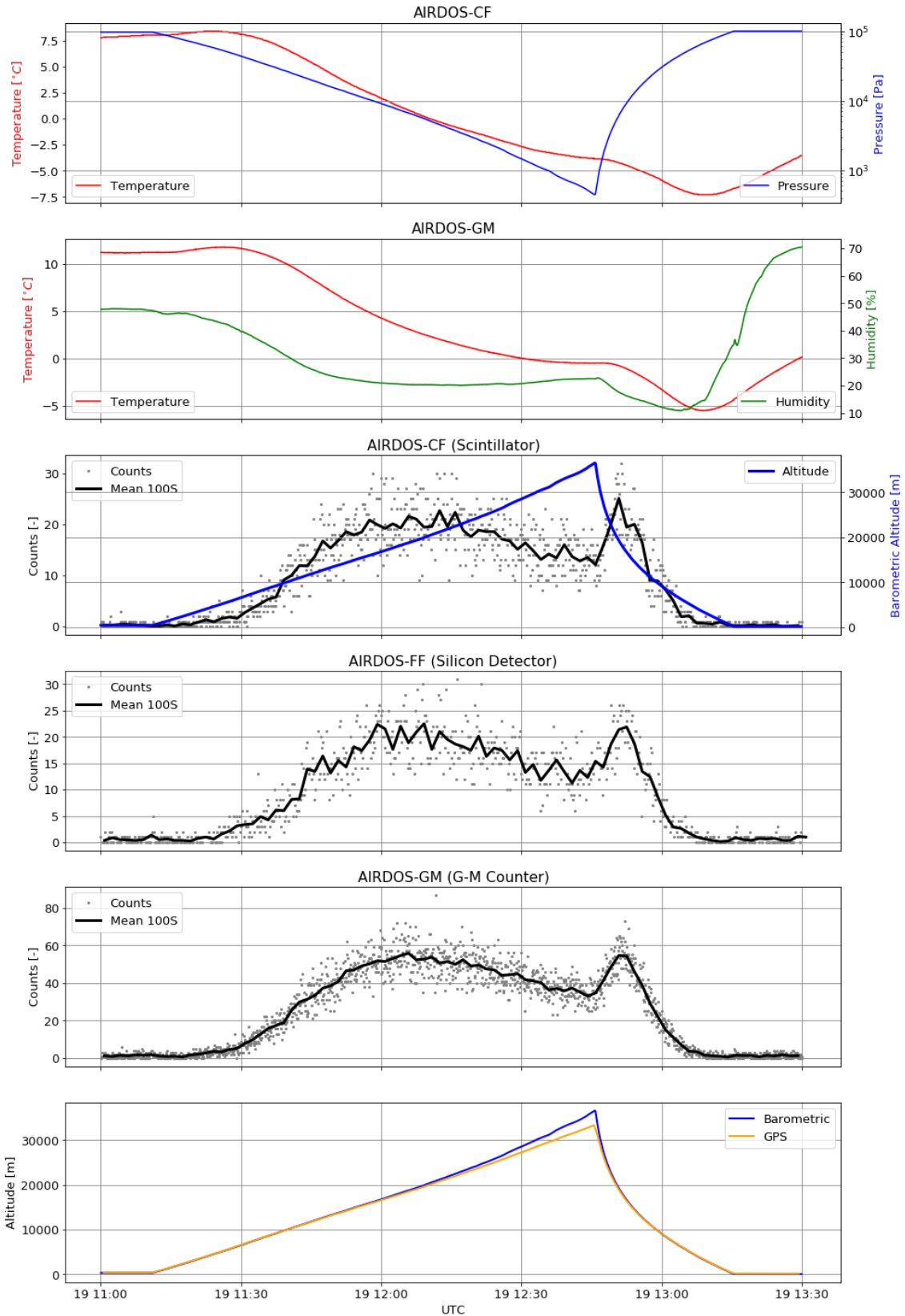
Figure 4.2. FIK-6 experiment setup using the Hwoyee Weather Balloon 1600.

■ 4.1.4 Results from the balloon flights

The flight FIK-6 took place on December 18th, 2020 and lasted 1 hour and 40 minutes. The balloon was launched from Příbram airport (LKPM) which is located around latitude 50° N. The balloon flight path continued in the eastern direction for about 80km.

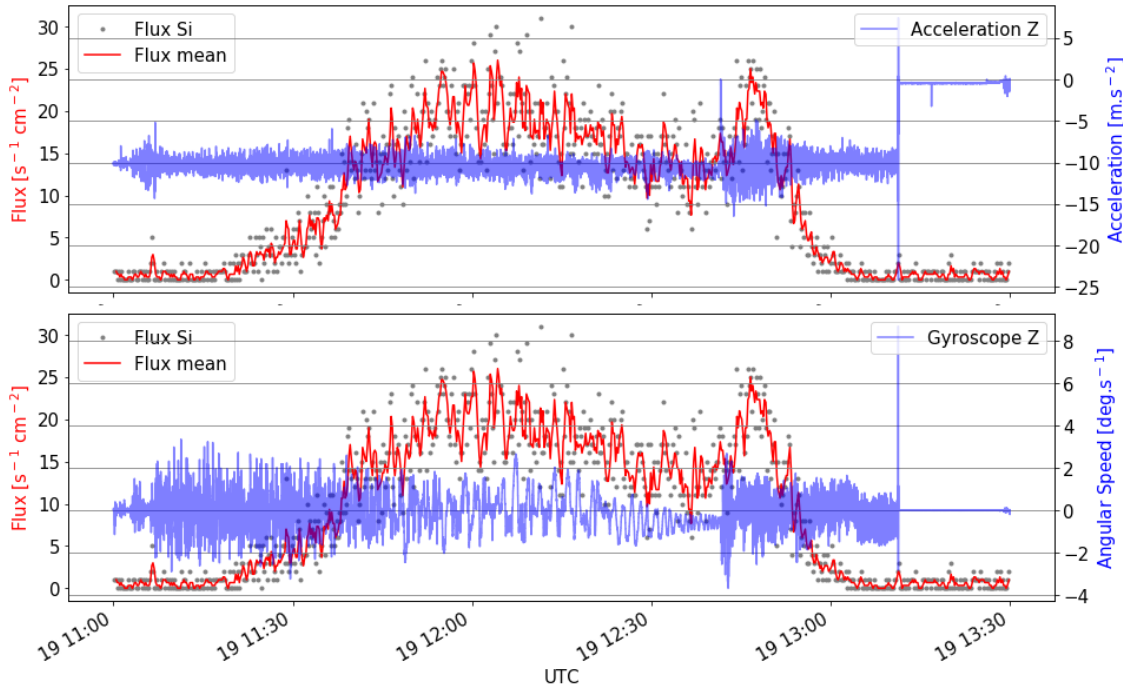
The system TF-ATMON recorded temperature, air pressure, humidity, and radiation characteristics as histograms of deposited energy of radiation events from all three radiation sensors in the gondola see Figure 4.3. The barometric altitude was calculated using the International Standard Atmosphere model 1976 [89].

4. Subsequent Experiments



[FIK-6_RAW_data]

Figure 4.3. Raw data measured during the flight. From top to bottom: temperature near scintillation crystal, air pressure inside the box of crystal, temperature inside the gondola, relative humidity inside the gondola, counts of radiation events per 10 seconds counted by scintillator, silicon detector, and G-M counter, barometric altitude, and altitude from GNSS.

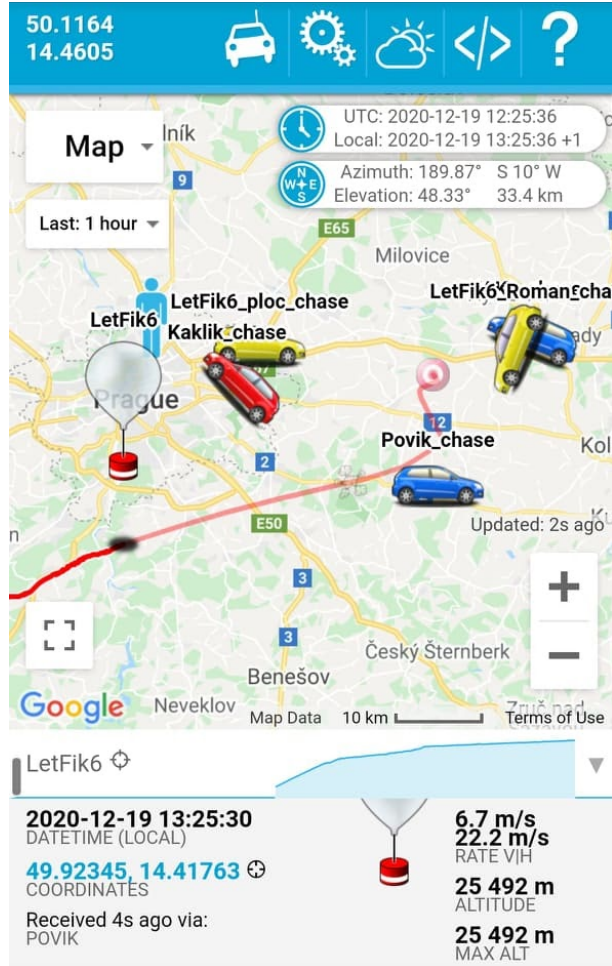


[FIK-6_telemetry]

Figure 4.4. Acceleration and Angular Speed in axis perpendicular to the ground combined with ionizing radiation flux measured by the silicon PIN diode detector.

Figure 4.4 demonstrates the importance of telemetry data from the TF-ATMON system during measurement processing. The graphs show an increase in the response of the silicon ionizing radiation detector at the times of take-off, burst, and landing when there was a rapid increase in mechanical stress. The effect is caused by the microphone effect of the silicon detector circuit. At the same time, it can be seen there are considerable vibrations, rapid changes in acceleration, and gondola rotation during the balloon descent. The increase in humidity is also observable in fig 4.3, which can even freeze on the instruments during some parts of the flight. All of them may affect the measurement of atmospheric quantities and for some types of instruments, they have to be compensated.

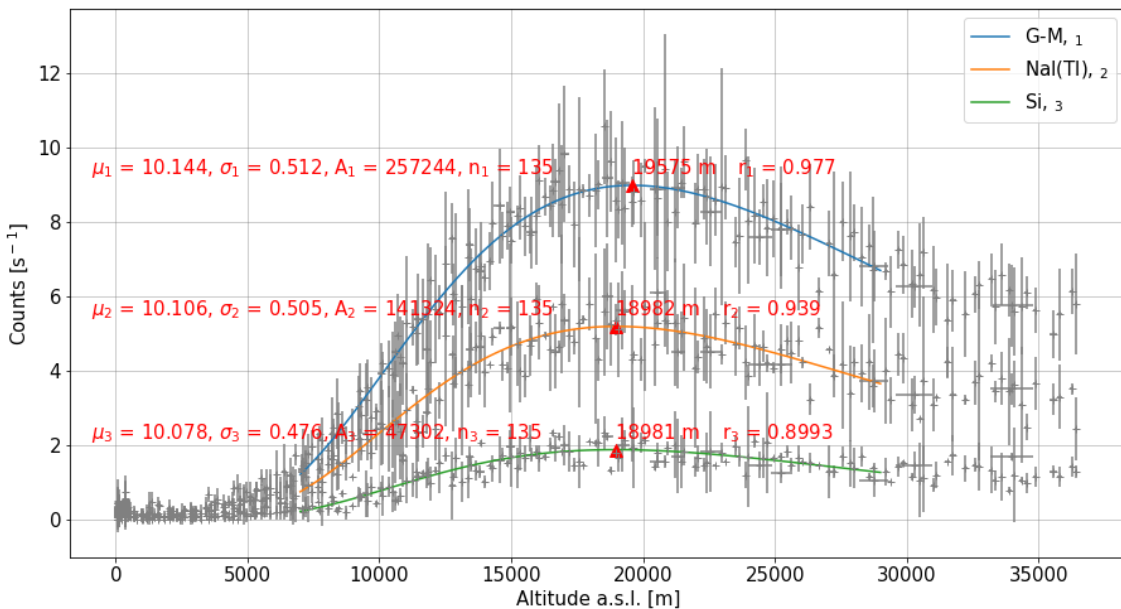
The graphs show that the maximum reached altitude was approximately 33 km above sea level. During the flight, the balloon passed the Regener-Pfotzer maximum twice. The rescue team followed the balloon along the whole flight trajectory. The precision of tracking allowed some participants of the rescue team to see the gondola touchdown visually. Therefore the gondola was successfully rescued within a few minutes after touchdown (Figure 4.5).



[FIK-6_rescue_team]

Figure 4.5. A screenshot from HabHub tracker. The CRREAT measurement vehicles, serving as stratospheric balloon chase cars, are equipped with telemetry receivers at the landing site. They are prepared for immediate gondola recovery, thanks to precise touch-down location predictions.

By processing the data a graph of detected altitude Fig. 4.6 was obtained. It shows that the measured altitude of the Regener-Pfotzer maximum was for all detector types around 19 km above sea level. As the measured data show in Fig 4.6, there is a very noticeable difference between a number of data points measured during the flight upwards and during the descent. This difference is mainly caused by the different values of vertical speed. In future balloon flights, this problem is planned to be overcome by a controlled descent, during which the rate of descent can be decreased in some phases of the flight so that it can be more comparable with the speed of the ascent.



[R-P_maximum]

Figure 4.6. Log-norm fit of ionizing radiation measured data with calculated Regener-Pfotzer maxima for different detectors (G-M tube, NaI(Tl) scintillator, and silicon PIN diode). Measured data are depicted with gray color as mean from 5 minutes of measurement with 2σ standard errors.

4.1.5 Outcome of stratospheric balloon flights

FIK flights were used to test different types of ionizing radiation detectors with the use of the Regener-Pfotzer maximum phenomenon.

The telemetric system TF-ATMON has been verified. It enables data recording, pre-flight instruments check, and their monitoring during flight. Thanks to the availability of different communication interfaces to the avionics, the use of various payload detectors is simplified. The technology at the same time improves the possibilities of the fast localization of a balloon gondola after its landing. It is therefore possible to carry out even experiments requiring a short time to recover the gondola after the flight.

As can be seen from Table 1 in appendix C, the last unsolved problem with the stratospheric balloon flights is the control of descent. Therefore, in future balloon flights and thunderstorm exploration, there exists a requirement to use the autopilot contained in TF-ATMON to control descent trajectory.

The descent should be controlled by using an airframe carrying a payload. Thus it would be possible to choose the landing site and reduce the possible risk of creating dangerous situations and at the same time with a possibility to control the descent rate and trajectory. Another unresolved challenge for use of the balloons for thunderstorm research is the difficulty of launching them in strong winds, which are nearly always present near storms, especially at times when the measurements are most critical 4.7. For these reasons, it became necessary to shift to other carrier platforms to be used for practical storm activity measurements. The logical alternative for this step is to employ UAS.



balloon_wind_takeoff]

Figure 4.7. The experimental stratospheric balloon takeoff (FIK-2) under increased wind conditions. The takeoff was partially successful; however, the gondola impacted me and then the ground, causing damage to the internal power supply and telemetry antenna.

[autogyro_thunderstorm]

4.2 Autogyro Thunderstorm Flights

Despite widespread efforts which could be found in the literature [90–93] to deploy measurement balloons into thunderstorms with various sensors, these attempts were often unsafe, and the results are sporadic because the balloon flight path is uncontrolled or control is very limited⁵. Therefore that technique seems to be outdated in comparison with the current UAV technology. This fact led to the exploration of using UAVs instead. Moreover, due to the spatial extent of lightning structures (see section 5 for details), it's required to experiment with multiple coordinated locations simultaneously, which is practically unattainable with uncontrolled balloons. Therefore better understanding of the phenomena can very likely be achieved by using specially equipped UAS, which enables measurement directly in or near the thunderstorms. UAS offer additional advantages, such as the ability to measure in specific atmospheric layers, where it is required to be actively held, which is useful for determining key parameters that influence cloud electrification, like radon and aerosol concentrations on the entry of LCL for example. The obvious requirement is to use a new unmanned airframe using TF-ATMON described in section 4.1 and employ the integrated flight controller to take control over the measurement procedure in the atmosphere.

⁵ <https://windbornesystems.com/>



[TF-G2_fly_clouds]

Figure 4.8. TF-G2 autogyro under the clouds, during one of many test flights.

The described idea resulted in the attempt to use an unmanned autogyro to carry measuring instruments to the vicinity of thunderstorms 4.8. The main goal of this experiment was to measure and locate the ionizing radiation presence together with the electric field and resolve the uncertainty of the source and direction of ionizing radiation produced in thunderstorms. For the investigation of thunderstorm activity, an autogyro presents several key advantages over other types of UAVs such as multicopters or fixed-wing aircraft, primarily due to its unique aerodynamic properties and operational capabilities. Autogyros, or gyroplanes, leverage the autorotation of their main rotor to stay airborne, which allows for safe flight at low speeds and in turbulent atmospheric conditions often encountered near thunderstorms. Compared to multicopters, autogyros are more efficient in terms of energy consumption for longer flight tracks, as they do not require power and control to spin multiple rotors for lift, relying instead on forward motion or wind. This efficiency is advantageous for conducting high-altitude atmospheric research missions that demand sustained presence in targeted areas to gather comprehensive data. Moreover, unlike fixed-wing aircraft that require higher speeds and runways for safety, autogyros can perform take-offs and landings in confined spaces, making them ideal for deployment in varied terrains and closer proximity to storm activities. Their inherent stability, even in gusty conditions, allows for more reliable data collection of meteorological parameters.

4.2.1 Autogyro airframe

Because there was not commercially available a suitable unmanned autogyro to perform atmospheric measurement in stormy conditions. The situation resulted in the design of TF-G2 autogyro which I developed in cooperation with the ThunderFly team. This step represents a significant advancement in the design and application of UAV technology for atmospheric research, specifically targeting the challenging conditions presented by

thunderstorms. The TF-G2 autogyro's airframe utilizes a lightweight yet robust and high-impact strength 3D printed material for the airframe and unique rotor design, which enables rotor blade shape modification. This technological decision gives the ability to easily replace parts, which is useful to quickly resolve damages as flights near thunderclouds often result in mishaps. Internal components are protected from the weather by a waterproof fabric cover, which enables easy service access and supports equipment variability with its shape adaptability. Furthermore, the airframe's design allows easy access to onboard instruments and maintenance. This capability is achieved by rack-style mount options, where the payload could be easily fixed to a grid of screw holes which can be seen in figure 4.9.



[TF-G2_hangar]

Figure 4.9. A development version of TF-G2 autogyro, waterproof fabric cover removed. The 3D-printed parts could be seen according to the grid of screw holes used for mounting of the experimental equipment.

The avionics design is largely identical to the avionics used in already described stratospheric balloon flights, with differences primarily in the power supply, because the autogyro includes components for propulsion, such as an electric motor and its ESC. To ensure robust pre-flight control, the ESC provides status information, including energy drawn from batteries via the UAVCAN bus. Another distinction is the use of special sensors, like an airspeed sensor, half-duplex telemetry system, and specific sensors used directly for atmospheric measurements.

■ 4.2.2 Airspeed sensing

In the case of autogyros, similar to airplanes, it is required to measure the IAS to safely perform takeoffs and in-flight maneuvers. Even though autogyros cannot be stalled in the traditional sense because their lift is generated by the rotor's rotational speed rather than directly by airspeed, they exhibit unique behavior. At insufficient forward airspeed, a gyrocopter begins to settle until it potentially impacts the ground — a

scenario that can be considered a survivable landing. Conversely, when the airspeed is excessively high, the rotor can easily exceed its critical RPM, leading to potential rotor disintegration. To mitigate these risks, the TF-G2 autogyro is equipped with an IAS sensor to accurately monitor and control airspeed, thus ensuring operational safety under varying flight conditions. Initially, a conventional Pitot tube was used for that purpose, but it proved very sensitive to clogging by snow, ice, or mud after complicated landings, necessitating disassembly and thorough cleaning. Thus, I proposed a solution named TFSLOT01, utilizing the Venturi effect. Where the velocity and pressure of the fluid are required to meet Bernoulli's principle(1).

$$\frac{1}{2}\rho v_\infty^2 + p_\infty = \frac{1}{2}\rho v^2 + p \quad [\text{Bernoulli}] \quad (1)$$

Then the velocities are in relation to cross sections (2) in the plane of pressure measurement ports

$$\frac{v}{v_\infty} = \frac{A_D}{A_d} \quad [\text{cross_section_areas}] \quad (2)$$

Therefore equations for pressure difference and airspeed velocity could be derived (3), which corresponds to the IAS.

$$\Delta p = \frac{1}{2}\rho v_\infty^2 \left[\left(\frac{v}{v_\infty} \right)^2 - 1 \right] \Rightarrow v_\infty = \sqrt{\frac{2\Delta p}{\rho \left[\left(\frac{A_D}{A_d} \right)^2 - 1 \right]}} \quad [\text{air_velocity}] \quad (3)$$

Where

- Δp : Measured pressure difference
- ρ : Air density
- v_∞ : Free air velocity e.g. measured airspeed
- v : The velocity of air running through the sensor
- A_D : Cross-section area at the position of the outer pressure port
- A_d : Cross-section area at the position of internal pressure port

There is also should be noted that the sensor utilizing that principle is theoretically more sensitive (e.g. has a higher measurable pressure difference at the same airspeed) than the pitot-static tube (at the same air density) in the geometric configuration where the following equation(4) is valid

$$\frac{A_D}{A_d} > \sqrt{2} \quad [\text{IAS_sensitivity}] \quad (4)$$

The advantage of the higher sensitivity results in increased drag, but it should be negligible at low airspeeds. Therefore the best use case of the sensor is the integration of the sensing device into the relatively massive fuselage or other suitable airframe structure. In the case of TF-G2 autogyro, it is resolved by integration of the TFSLOT01 sensor directly to the rotor head, just below the rotor hub as could be seen in fig 4.9. Figure 4.10 shows details of the TFSLOT01 sensor.

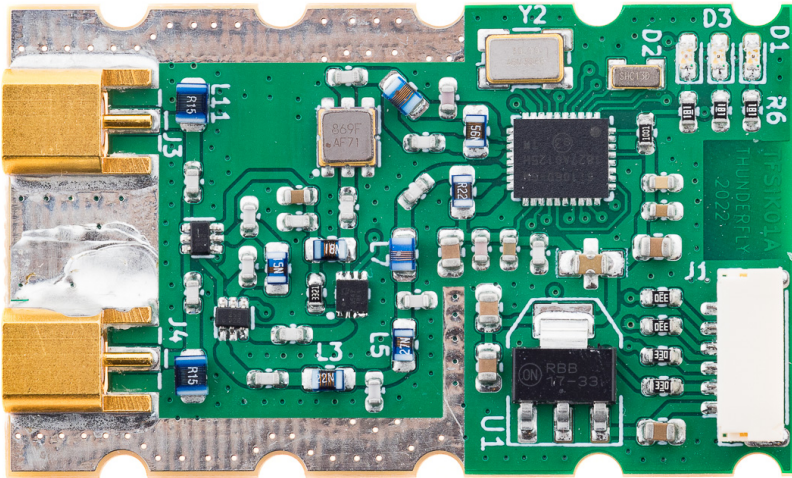


[TFSLOT01]

Figure 4.10. The photograph showcases a close-up of TFSLOT01, where the front part features the entry aperture AD. The narrow aperture Ad is slightly deeper into the structure. In the rear of the photo is visible the I2C cable, used to connect the sensor to the flight controller.

4.2.3 Telemetry system

The telemetry system used in the TF-G2 autogyro is significantly improved but still based on the technology previously tested on the stratospheric balloon's telemetry link. Unlike the one-way radio communication utilized in the balloon experiments, the TF-G2 employs a bidirectional half-duplex, TDM radio system. The modem still operates at a frequency of 433MHz, but with an improved RF front-end to ensure a more reliable communication link due to the demanding environmental conditions of the TF-G2 flight. The modem firmware is again based on modified SiK firmware, which incorporates integration to the new hardware capable of supporting antenna diversity, specifically a 2x2 MIMO configuration. This arrangement allows for the connection of two external antennas, each of which can be utilized for both transmitting and receiving signals. The optimal antenna is selected based on the RSSI metric on the received packet preamble before each transmission of the next packet. This dual-antenna setup significantly improves signal resilience against interference from multipath fading and is also robust against mechanical damage to one of the antennas—a critical improvement over the previous single-antenna modems used on balloon flights, where the damage actually happens (see Table 1 in appendix C). It is also quite a common failure mode of the antenna on UAVs, caused by prolonged exposure to vibrations during flights.



[TFSIK01]

Figure 4.11. TFSIK PCB without electromagnetic shielding and 3D printed housing. The RF input and output with impedance matching network, RF switch, band-pass filter, and LNA are on the left of the photo.

Furthermore, the improved system benefits from the versatility in antenna configurations at the ground station side, where a combination of the two antennas (directional and omnidirectional antenna) ensures optimal communication over varying distances. This dual-antenna approach at the ground station seamlessly switches between short-range and long-range communication modes without user intervention, offering a reliable link irrespective of the TF-G2's distance from the ground station.

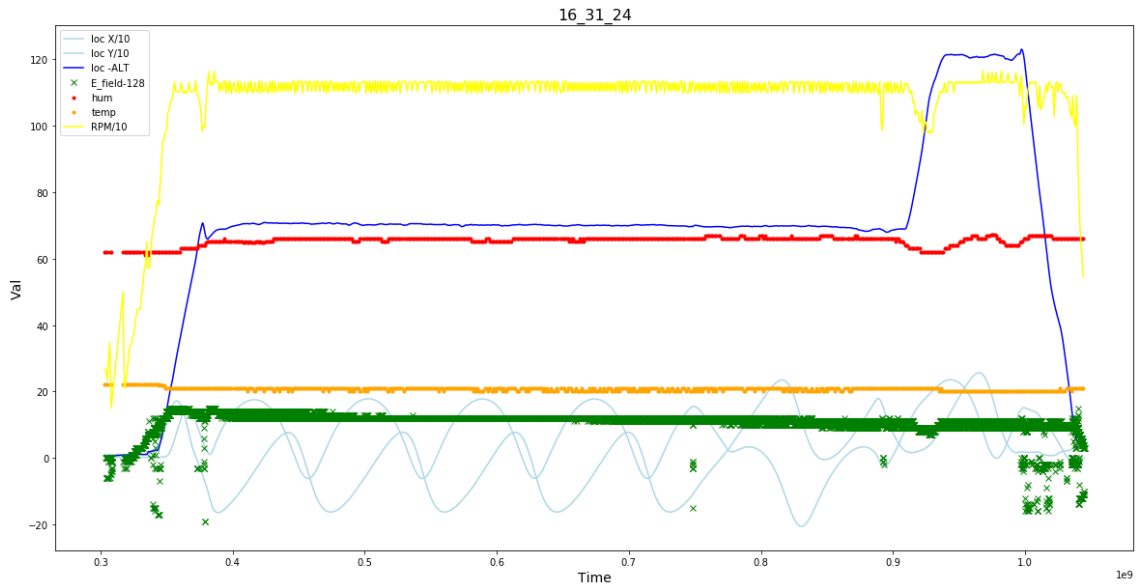
■ 4.2.4 Carried sensors

The key innovation in the TF-G2's design is the tight integration of specialized sensors for measuring electric fields and ionizing radiation. These sensors are mounted in a way to minimize interference from the airframe by maximizing the benefits of the autogyro construction. The placement of an electric field mill is directly under the rotor, exploiting the UAV rotor's characteristic of being unpowered, thus avoiding significant electromagnetic interaction with the measured values. See the figure 4.12. The only additional requirement on the airframe is that the rotary disk of EFM is electrically connected to the measuring electronics. That is achieved through a conductive connection of the rotor's bearing. For the detection of ionizing radiation, the UAV has been equipped with a semiconductor detector, AIRDOS03 (UAVDOS), previously tested during balloon flights. It is situated in the UAV's fuselage under a waterproof fabric cover and connected to the TF-ATMON system via serial link similarly as described in the 4.1 section. The avionics system manages sensor readout, synchronizing data collection with the TF-G2's flight path and with data from other sensors (EFM, humidity, etc.), see Fig. 4.13 for an example of that data. That onboard data processing together with the telemetry link enables real-time preliminary analysis, aiding in the assessment of collected data during the flight.



[E_mill_rotor]

Figure 4.12. Close up view of electric field mill (THUNDERMILL01) mounted into the autogyro rotor head. The sensing electrodes are below the rotating grounded disk. Part of one sensing electrode is visible in the left side of the E-mill's rotor disk opening.



[E_mill_data]

Figure 4.13. Electric field measurement data along with environmental humidity and temperature, aligned with flight parameters during a flight in fair weather.

■ 4.2.5 Takeoff technique

Since the unmanned autogyro TF-G2 (like other autogyros) requires the rotor to be spun up to a flight RPM value to allow its operation during the flight, it is necessary to inject rotational energy into the rotor before takeoff (in the case of TF-G2 the required energy

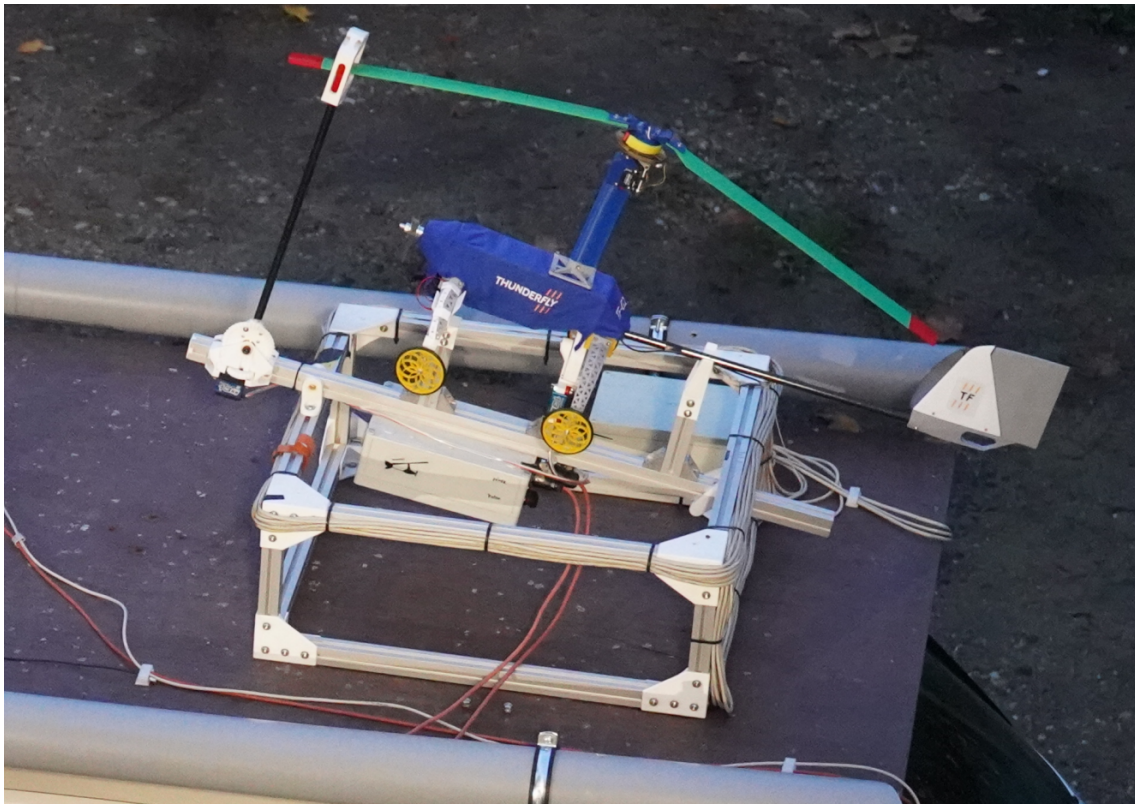
range is something between 100 to 200 J, depending on the actual weight and rotor configuration). One of the simplest ways to achieve this spin-up is by ensuring airflow through the rotor, which is firstly pre-spun to a minimum RPM by directly applying a rotation force to the rotor. Subsequently, these rotations increase to flight speed through forward motion. The required minimum forward speed needed to increase RPM to flight value is in the range of a few meters per second. In the case of those conditions, the autogyro becomes airborne within a few tens of meters, after that the internal autopilot is able to automatically climb to a stable flight. To ensure this procedure is feasible during approaching thunderstorms, it was necessary to develop a range of supportive devices, such as a launch platform and visualization of the gyrocopter's status on the car roof. The takeoff from the car roof platform is an advantage for safety and time-saving. The resulting design of the takeoff platform is visible in Figure 4.15, where the autogyro is secured in an inclined launch position, allowing to increase in the airflow through the rotor. In this position, the gyrocopter's rotor is locked by a mechanism contained in the platform until takeoff. At the beginning of this assisted takeoff, the platform unlocks the rotor, which is then spun to minimum speed by weights connected to the rotor by pulleys. At this minimum RPM speed, aerodynamic forces enable further rotor acceleration due to the incoming airflow. However, since the launch platform is mounted on the roof of the vehicle, the crew in the vehicle (pilot and driver) cannot directly see the procedure. Therefore, it is mandatory for the vehicle's crew to receive adequate and high-quality data to semi-automatically carry out the launch procedure. The TF-G2's autopilot is programmed to automatically transition between the different phases of takeoff once predefined criteria are met. Therefore the crew only needs to monitor key decision variables such as IAS and rotor RPM, to be able to respond adequately to a non-standard situation. These values are therefore required to be displayed with low latency and in a format that enables the car driver to determine whether to speed up, slow down, or maintain the current speed. This is facilitated by a set of displays, as seen in Figure 4.14, which have been added to the measurement vehicle. Additionally, the overall status is visible through an analog camera, which provides both the driver and the operator a view of the autogyro, mounted in the takeoff platform. However, this display is limited by the camera's frame rate and the resolution of the analog camera (a digital camera cannot be used due to typically high latency in the image encoder and decoder). The driver and operator also have access to auditory and visual signals indicating the platform and takeoff status via a shared handheld controller, which can be used to abort the takeoff procedure in the event of an unforeseen issue.



[takeoff_display]

Figure 4.14. Measuring CAR2 was equipped with special instruments required to operate the unmanned autogyro TF-G2. In the center is an autogyro status display with rotor RPM and IAS indicators, the bottom is video from the roof camera and on the right, there is a UAV operator's laptop.

The takeoff platform device is removably integrated into the assembly of magnetic VLF receiving antennas, as seen in Figure 4.15. This platform is connected to the ground control station mounted inside the trunk of the car and is controlled by the autogyro's autopilot states via previously described TFSIK01 telemetry modems. The platform's firmware responds to commands sent by the TF-G2 using the commands on the MAVLink 2 protocol. The mentioned handheld controller for the driver and operator is directly connected to the microcontroller managing the platform, allowing the platform's internal state to be overridden despite commands from the TF-G2. That takeoff solution is designed primarily to achieve overall safety before and during the thunderstorm measurement attempt.



`ro_takeoff_platform]`

Figure 4.15. Measuring CAR2 was equipped with a roof platform used to carry the TF-G2 autogyro to the thunderstorm site. The rotor fixing is the black arm on the left. The gray tubes are oriented vertically during actual takeoff and housing the weights used to prerotate the rotor to minimum RPMs.

4.2.6 Test flights

Throughout the development phase of the unmanned autogyro, extensive test flights were conducted to evaluate various modifications and enhancements to the UAV design, the firmware of the autopilot, and the ground equipment adjustments. One of these could be seen in the figure 4.16. Among these development verification, there were tests on detectors in certain scenarios. These are experiments usually conducted outside of the main thunderstorm session.



[lift_drag]

Figure 4.16. Measuring CAR2 was equipped with a roof lift and drag measuring platform used to carry on-ground testing procedures.

Two notable supportive experiments emerged from these testing flights. The first significant experiment involved testing the UAV's flight capabilities under strong wind conditions alongside measuring floating dust concentrations (Floating dust is associated with the development of storm activity and the electrification of cloudiness [94]). For this experiment, New Year's Eve fireworks were used as a modeling source of floating dust. The measurements were significant, as expected because the instrument convincingly detected at least a two-fold increase in the concentrations of floating dust in hours following the fireworks display. The second experiment was focused on verifying the directional homogeneity of the signal received by a Quadrifilar Helix (QFH) antenna (see figure 3.8). Leveraging the close frequency proximity of the telemetry transmission band from the UAV (433 MHz) to the observational band for lightning discharges, this experiment was conducted by having the UAV fly in circles around a measuring vehicle. The signal level was manually monitored on the receiver. This experiment was used for verification of the QFH antenna's effectiveness in maintaining homogenous sensitivity. In addition to the mentioned experiments, numerous routine flights and experiments were conducted near storm clouds. These experiments were carried out simultaneously with ground measurements, which were the primary focus. The success of these attempts varied greatly; however, system failures often occurred, preventing the intended use of the collected data.

4.3 Ground level measurements

Within the context of the CRREAT project, the term *ground level measurements* encompasses a broader scope, including measurements based on passive and stationary high-altitude observatories. My involvement in these stationary measurements was minimal, primarily relating to some aspects of electronics design. However, I consider it

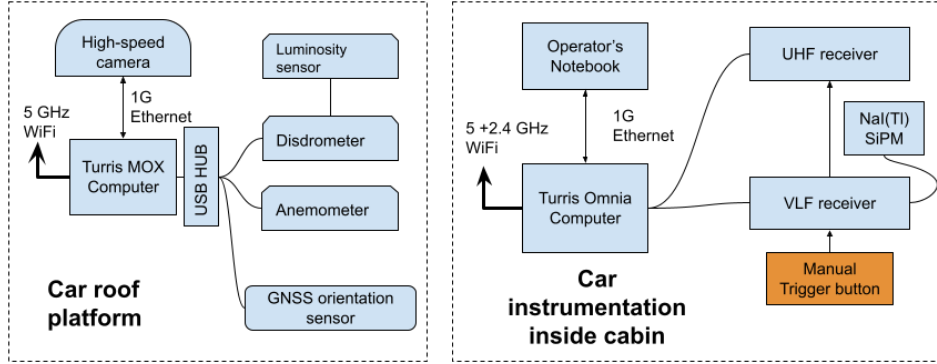
useful to mention the existence of these measurements here, as theirs uses similar, or identical equipment, which allows for the extrapolation of findings from the stationary observation's data to active ground measurements conducted near thunderclouds with vehicles, on where my primary work was focused.

The summer storm measurement campaigns employing vehicles equipped with detection devices represent a culmination of all experiments described in previous sections. The deployment of vehicles equipped with specialized detection devices is based on exhaustive preparatory work, where each component's function and reliability are evaluated by previously mentioned experiments performed occasionally out of the main thunderstorm session e.g. in winter. Given that the components and devices were often tested separately to prevent their failure during critical moments of storm activity. The average duration of monitoring a single storm's development is approximately half an hour, offering minimal opportunity for adjustments or repairs. The presence of an error on a single of three cars usually fails in a thunderstorm observation attempt. This constraint illustrates the importance of reliability, precise calibration, and software stability of the instruments used in the described research. Throughout the campaign, the reliability of the instruments, the methods of their calibration (for example dark frame and flat-field of cameras), and the challenges posed by software errors were gradually identified as the critical barriers to conducting the research. Each of these elements significantly influenced the outcome of the measurements and, in turn, the insights that could be collected from storm activity. This reality unexpectedly highlights the intrinsic complexity of atmospheric measurements, when attempting to capture the transient nature of thunderstorm phenomena. Recognizing these challenges, during the multiple summer storm seasons, many measuring expeditions were carried out in the Czech Republic and Slovakia with the equipment described. This allowed the measurement of electrostatic, magnetic, electromagnetic, and optical manifestations of storms, including monitoring ionizing radiation. By comparing the different obtained lightning recordings with each other, individual phases of lightning can be reconstructed.

Observations were carried out with a gradually improving strategy to get the measuring car (especially the ones equipped with radiation detectors) as close to the storm cell or under the cell as possible. The position of the storm cell was monitored by services using data from third-party networks [95, 66].

4.3.1 Measuring Cars Infrastructure

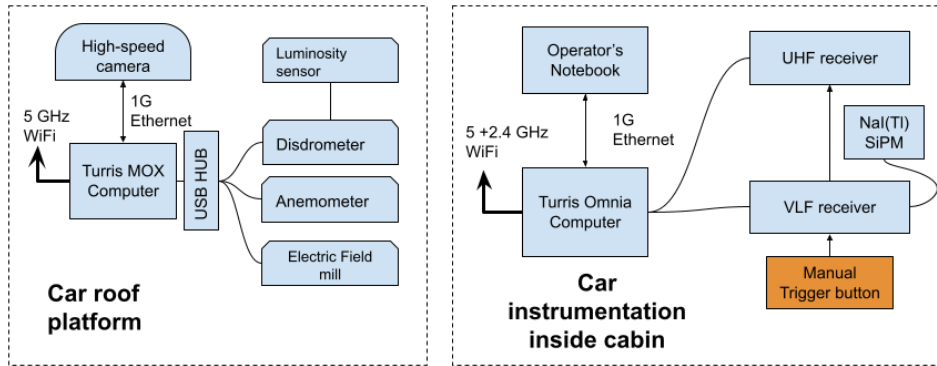
The position of the measuring car was stationary during the period of thunderstorms. Moreover, in the case of radiation detectors, an extended static position time interval is required to capture the before and after storm activity in order to be able to record the development of radiation change including the local parameters of the radiation background.



CRREAT_CAR0_diagram]

Figure 4.17. CRREAT CAR0 instrumentation schematic diagram. This car differs with a four-element UHF antenna array receiver and GNSS orientation tracking sensor.

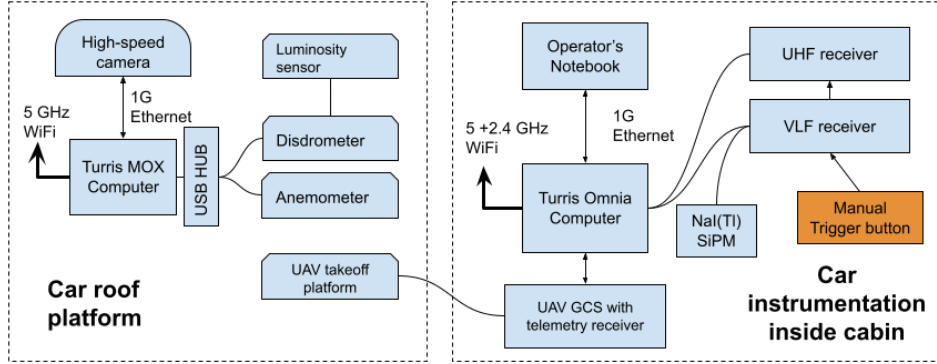
During the measuring campaigns, the method of data recording developed as well. The first campaigns were trying to make fully automatic recordings based on observed electromagnetic signals using the described LIGHTNING01 module. Please refer to the section 2.1 for details. This system however had a lot of imperfections leading to its abandonment in the measuring car CAR0, where it was replaced by solely manual activation of recording until the trigger was implemented directly into the VLF receiver's FPGA. See the fig. 4.17 for overview. The manual activation of the recording was based on the visual perception of the operator observing the lightning activity. In contrast to CAR0, CAR1 was left with a semi-automatic method of activating the recording to compare the efficiency of both trigger methods. Car CAR1 thus had for a long time recorded triggers based on using a loop antenna and oscilloscope that generated triggers for other devices. See fig. CRREAT CAR1. After the successful test of manual triggers that option was implemented in all three cars.



CRREAT_CAR1_diagram]

Figure 4.18. CRREAT CAR1 instrumentation schematic diagram. This car has the electric Field mill sensor installed.

The trigger signal was initially distributed to the camera via the Ethernet network, a solution common to both measuring cars, but at the end of the campaign this method was abandoned and replaced with a direct trigger signal connected to the high-speed all-sky camera input because ethernet has unknown latency on processing the trigger packet from network and also in thunderstorm conditions, there sometimes happens that trigger packet is not derived to the camera correctly.



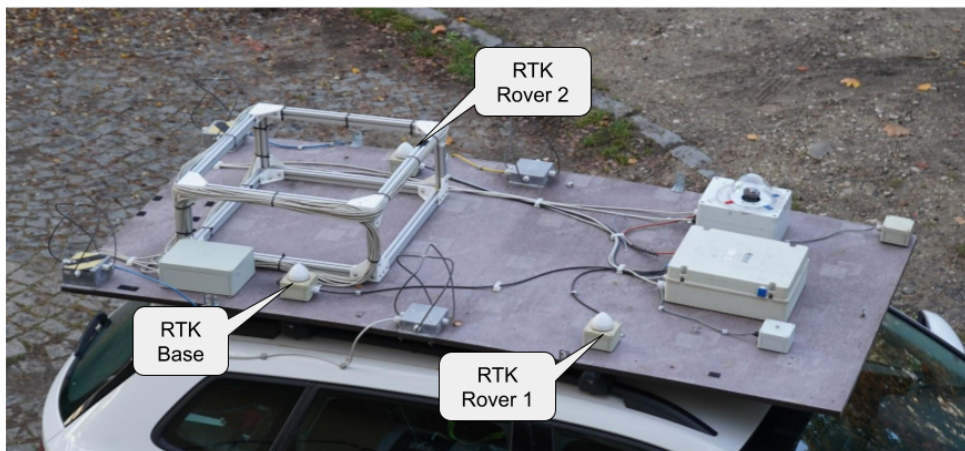
CRREAT_CAR2_diagram]

Figure 4.19. CRREAT CAR2 instrumentation schematic diagram. This car has special equipment for takeoff and command and control of the UAV (unmanned autogyro).

A significant challenge was caused by the time needed to record the data measured by individual detectors resulting from the long time interval needed to store the recording from the operational memory of devices. The dead time was gradually reduced by optimizing the settings and improving software and firmware, but it still remains the main limit preventing the gathering of data from more lightning events in case of successful expeditions.

For high-quality data collection on storm activity, most of the described instruments require accurate information about time and position to compare the recorded data with external data sources. GNSS receivers were mainly used for this purpose. The evolution of position tracking for the vehicle initially utilized a simple solution with a GPS receiver for coordinate logging and a manually targeted compass to determine car orientation. However, this method proved imprecise and unfeasible in the context of various operational tasks, as it was often neglected or not performed accurately. Therefore, it was necessary to explore other methods that ideally would not depend on manual recording of the car orientation. This led to the adoption of radio navigation, enabling real-time tracking of orientation. For this purpose, the three MLAB GNSS modules GPS02 equipped with a uBlox NEO-M8P receiver capable of Real-Time Kinematic (RTK) navigation were used. That module at the same time supports moving baseline configurations, allowing each receiver to be used both as a rover and a base station. The moving baseline in the context of uBlox means that position is measured in local NED coordinates relative to the base. Therefore baseline and three position angles could be estimated. This feature of the receiver not only enabled precise positioning but was particularly beneficial for applications like UAV following or

potential future implementation of landing back on the car's roof. Utilizing this for the car's platform orientation across three axes partially replaced the manually operated compass but faced challenges in signal quality due to onboard equipment interference. Additionally, such a solution is very sensitive to interruptions in the signal phase, as when the car passes under a highway bridge or driving on a road covered by trees, both can easily disrupt the signal phase and result in incorrect orientation measurements. The usability of this innovation was thus primarily hindered by the implementation in the selected receiver, which was unable to reliably indicate when the provided moving baseline coordinates were invalid.



`RTK_moving_baseline]`

Figure 4.20. This image shows the locations of the RTK (Real-Time Kinematic) antennas mounted on a vehicle for positioning using the moving baseline method.

It was initially assumed that the suboptimal results (even below the manufacturer's specifications) were due to poor-quality GNSS antennas. Basic patch active antennas were used, all oriented in the same direction according to the application note, to prevent phase shifts from different directions. However, changing the antenna type to a QFH antenna, which has significantly better parameters compared to the patch antenna, did not result in any noticeable improvement in the receiver's performance and ability to correctly mark invalid data.

To obtain precise system time for all onboard instruments in the measuring car, GNSS receivers were utilized. Initially, this was achieved by combining the relative PPS signal (as described in the chapter on the 3.2.2) with the absolute time from the internet, synchronized with the operating system time using *ntp-wait*. However, this method had drawbacks, it required a stable internet connection and took a long time to synchronize. Internet connectivity was provided via LTE, which was unreliable in some regions and during thunderstorms, leading to complications in initializing the measurement system

and difficulty in restarting the instrumentation after power outages, such as when the car's diesel engine was restarted. The latest solution involved connecting an additional GNSS receiver to the onboard router, Turris Omnia, which provided basic positioning and precise time information. This router then served as the accurate time source for the onboard ethernet network, significantly improving the reliability of the entire setup.

Inter-car communication

From the beginning of utilizing cars for atmospheric measurements, challenges were faced in how to effectively share information between drivers or operators of the measuring vehicles. Initially, with only two vehicles, the crew included an operator besides the driver to manage navigation, search for suitable observation spots, respond to the actual storm developments, and assist with instrument operation. However, this approach became impractical with the addition of a third vehicle due to the demand for a high number of personnel. The first attempt at solving this issue involved using PMR radios for inter-vehicle communication, which quickly proved ineffective for drivers and did not support the inclusion of a coordinating team member. Expanding PMR radios with chat and location sharing via standard communication apps also fell short in practicality.

Thus, HabHub technology, previously tested in balloon flights (see the chapter 4.1), was transitioned to, enabling vehicle location sharing on a unified map on the webpage. This service, augmented with Jitsi⁶ for voice communication, offered a more functional solution. However, challenges persisted, in the form of poor audio quality from laptop microphones and unresolved integration of vehicle hands-free systems with measuring notebooks connected to the internet via onboard modems, because the connection interfered with connecting the driver's regular smartphone used for navigation.

4.3.2 Data capturing procedure

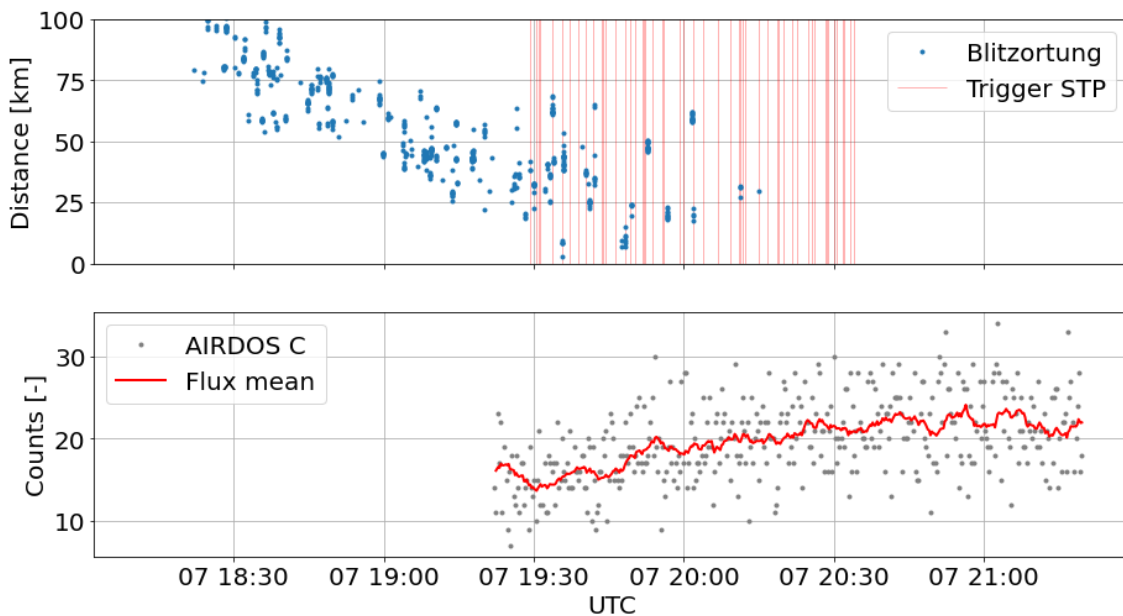
Before each expedition, selecting the right time and location for observation was essential for the experiment. This process involved a decision-making sequence that began with long-term weather forecasts to identify potential stormy days, followed by ECMWF model results tens of hours in advance. On the measurement day, satellite images revealing cumulonimbus cloud formation and, subsequently, radar data were used to pinpoint the precise location suitable for measurements. Communication between cars, aside from coordinating measurements and positioning to ensure a non-linear arrangement of cars, is aimed at maintaining a strategic positioning relative to the highway for rapid relocation in response to storm development. Ensuring geometrically advantageous positioning of the vehicles relative to storm clouds proved challenging due to the linear nature of highways. Sometimes, opposing exits allowed for symmetrical positioning around the highway without straying too far. In other cases, exits before, within, and after highway curves were utilized. Quick communication was also essential for confirming data records, as the lengthy recording time necessitated verification that all vehicles recorded data simultaneously (otherwise the data recording should be omitted), a task managed manually through verbal communication, highlighting the need for automation in future stationary measurement station setups.

4.3.3 Ionizing radiation measurements

Figure 4.21 shows an example of ionizing radiation measurement using the gamma spectrometer AIRDOS-C. In the upper graph, a storm approaching a parked measuring car is displayed using data from the Blitzortung.org network. The vertical red lines mark

⁶ <https://meet.jit.si/>

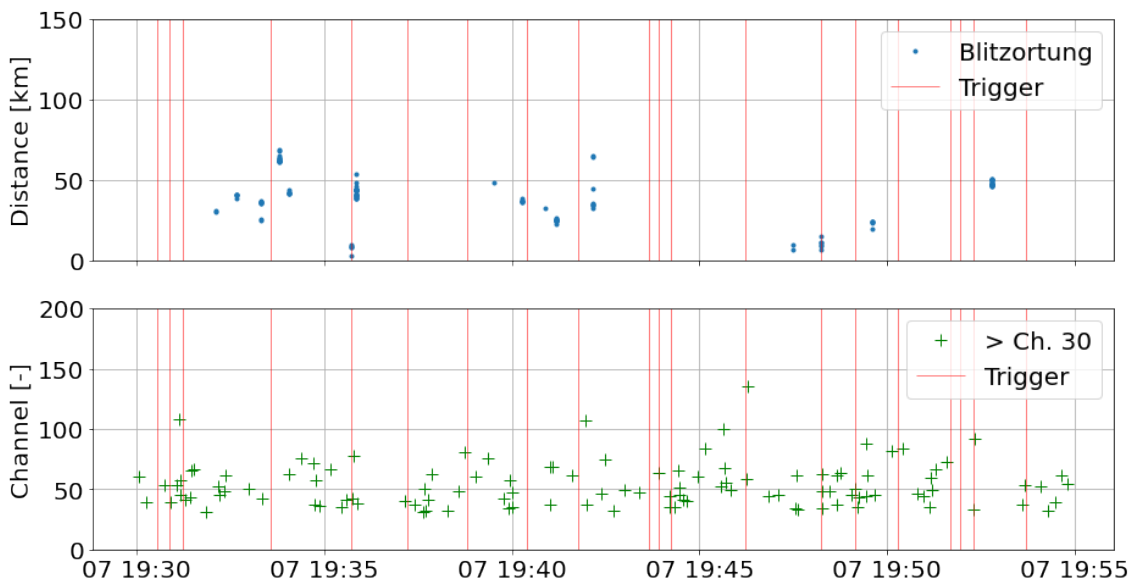
the times when lightning was registered by the STP antenna. The lower graph shows the number of particles registered by the ionizing radiation detector every 15 seconds. In this particular example, the lightning activity ceased just after 20:30. The graph shows an increase in ionizing radiation flux by approximately 30 %. This increase is related to a radon progenies washout from the atmosphere caused by rain that started at 19:45.



[figur_radon]

Figure 4.21. Measuring ionizing radiation using a car compared to lightning registered by antennas. The beginning of measurements using AIRDOS-C and STP antennas corresponds to switching on the devices after parking the car on a spot at 19:15. The measurement ended at 21:25 by switching off the devices and leaving the observation spot.

Figure 4.22 shows a detail of ionizing radiation measurement at the time when the storm was closest to the car. Individual particles of ionizing radiation registered versus detected lightning are shown. Only particles that have passed on energies higher than 2.4 MeV to the detector are displayed.



[fig_gamma]

Figure 4.22. Lightning detected by Blitzortung.org and triggers from STP antenna plotted together with individual registered particles of ionizing radiation above channel 30 of gamma spectrometer.

■ 4.3.4 Visual Camera measurements

Because lightning discharges often happen inside clouds and lightning channels are not directly visible, the videos of recorded lightning are converted to luminosity over time. The integral values of illumination are calculated from the video recordings of high-speed cameras using a script. The calculation is carried out over the entire image area by summing up the values of all pixels on each frame. These results are referred to as luminosity curves. The example can be seen on the graphs in Figure 4.24, depicting the course of light flux over time.

To maintain clarity, luminosity curves are added to videos, which are converted from BW recordings captured by cameras to false colors to make details of lightning (that have high luminosity dynamics) visible.

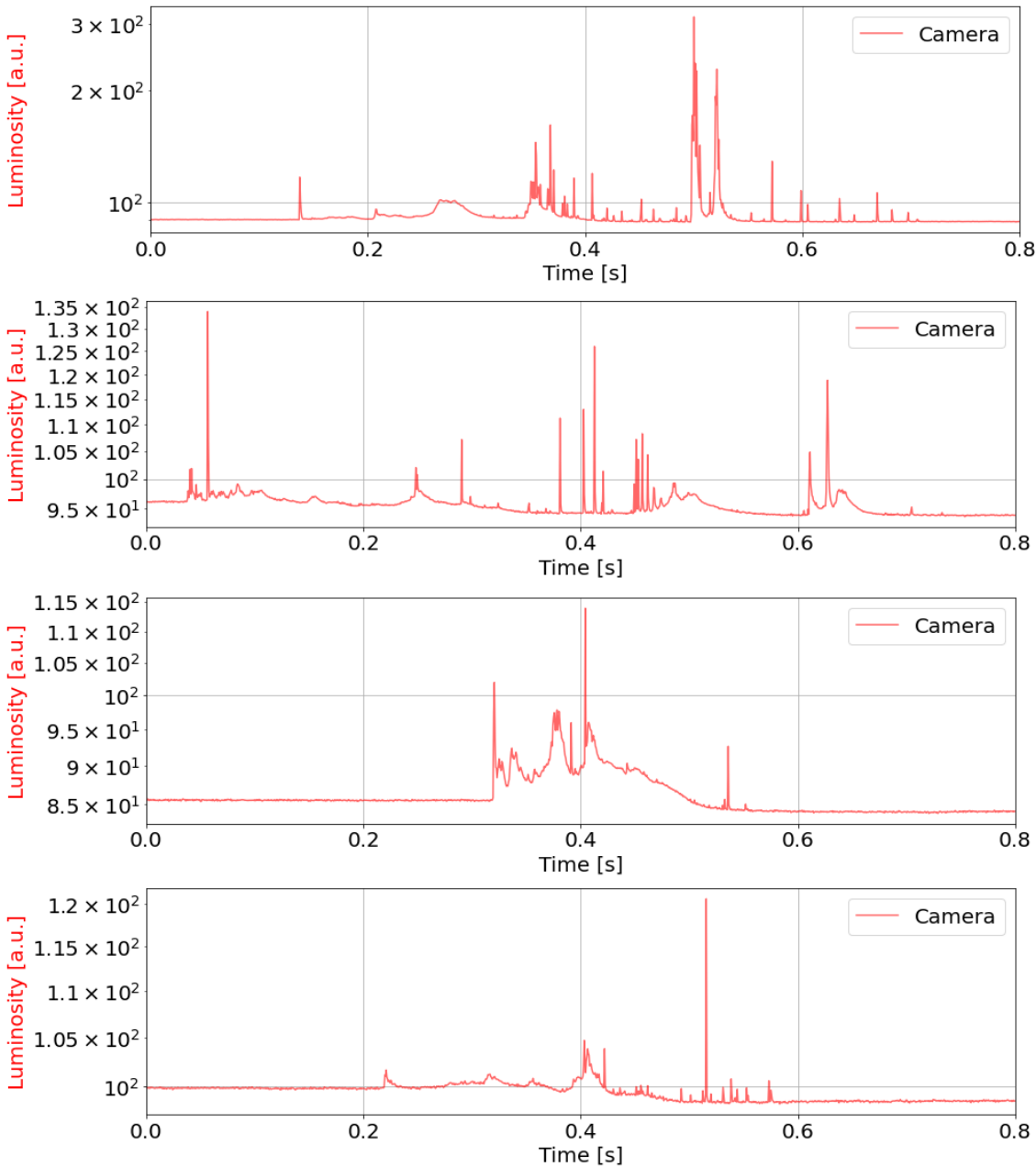
The following enclosed video [1627302288.9546976.mp4] shows lightning together with leaders and recoil leaders. During the observation, the camera is pointed towards the zenith and its lens allows capture of the entire sky from horizon to horizon. For the illustration of the camera view a plain camera frame is shown in Fig. 4.23. During the thunderstorm recording, the camera shutter time is decreased to capture lightning that has high brightness dynamics. As a result, lightning is not visible on the camera together with details of clouds and surrounding terrain. The processed video has the position of the horizon marked with a green circle with an inscribed designation of the cardinal directions. In the upper part of the video, there is a white graph showing a luminosity curve with a green pointer marking the current position of the displayed frame on the time axis. On the right, the used color range is visible, corresponding to the brightness recorded by each camera pixel with a depth of 8 bits. The bottom line shows the number of the current frame over the total number of frames recorded. The next is Sg=1/1 (information on which part of the camera's internal memory was used for recording) and the time of the current frame 'T=' in seconds relative to trigger time.



[figur_horizon]

Figure 4.23. A still image example from the all-sky camera showing horizon and fish-eye lens distortion.

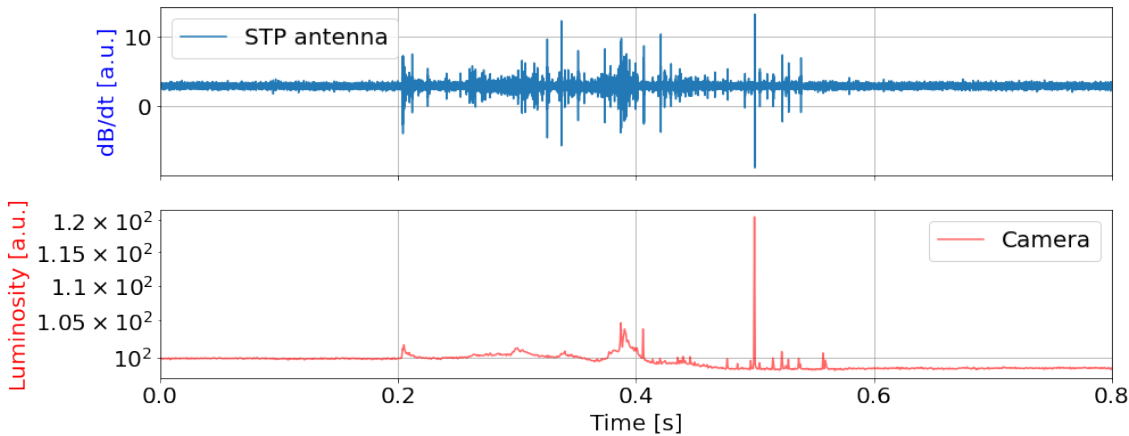
The resulting luminosity curves contain morphological signatures, such as sharp peaks or slow changes in luminosity. Thanks to this, video recordings with similar luminosity curve progressions can be compared, and from several recordings, those parts can be chosen that have similar luminosity curves and a visible lightning channel (not covered by clouds). Such a process helps to reveal what lightning looks like.

**Figure 4.24.** An example of luminosity curves for a few lightning.

4.3.5 Radio signal measurements

The advantage of using magnetic loop antennas to measure lightning is that observations are not disrupted by optically opaque clouds or daylight scattered in the atmosphere during daytime storms. However, when measuring the magnetic component of the electric field with a coil, only changes over time, specifically changes in the current flowing through the lightning channel, can be detected. A constant current in the lightning channel cannot be detected by a magnetic loop antenna. Figure 4.25 shows an example of lightning recorded simultaneously by an STP antenna and a camera. The camera recording clearly shows a change in luminosity, with the sky being brighter before the lightning than after it occurred. Slow changes in brightness, indicating slow changes in current, are not visible in the antenna recording. Instead, clusters of fast

pulses are observed, suggesting details about the development of lightning channels that are not visible in the camera recordings, likely because they are obscured by light from a constant current in the main channel. Pulses visible in both camera and antenna recordings are recoil leaders, and the most prominent short impulse is the CG return stroke.



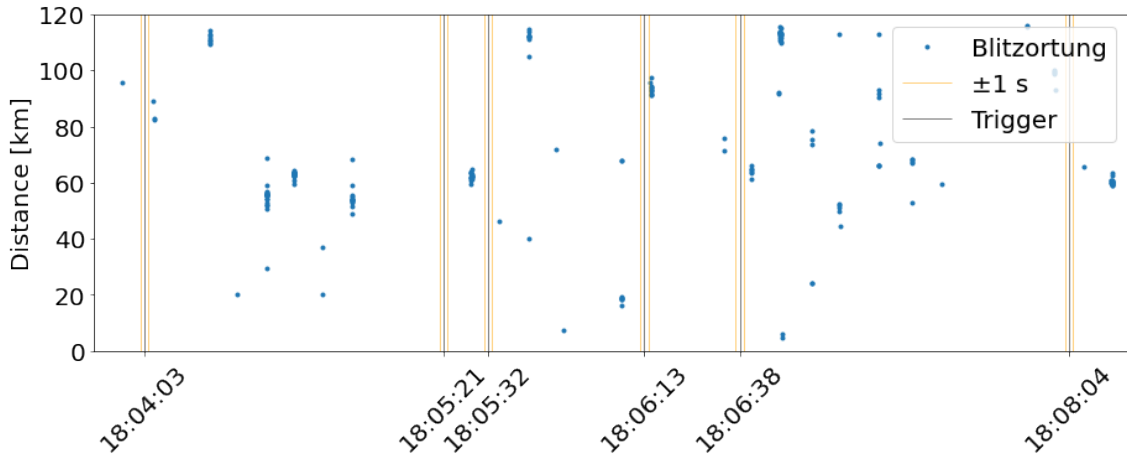
[figur_capture]

Figure 4.25. Example of data from STP antenna with the comparison to camera data.

4.3.6 Correlation of measured lightning with lightning detection network

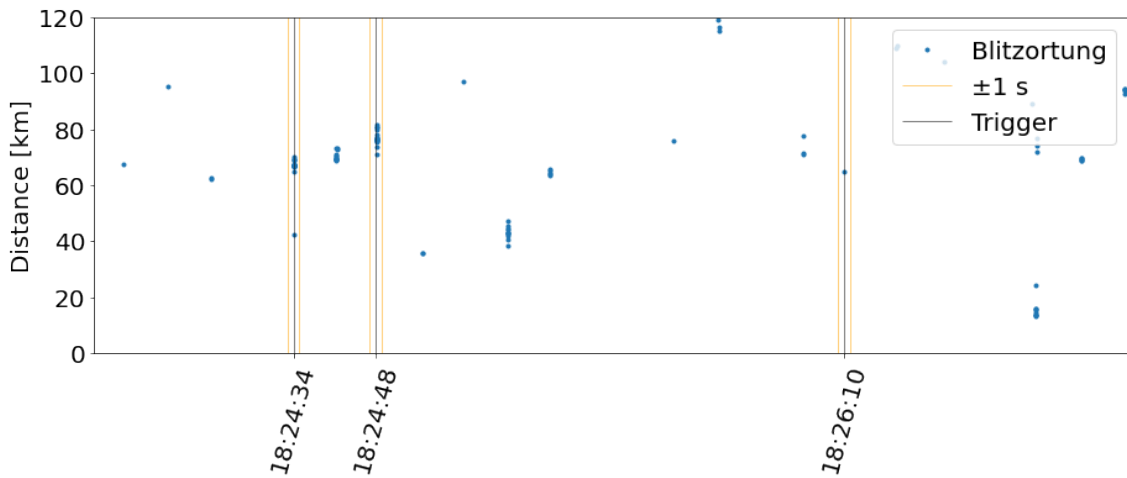
The detection of lightning using the STP antenna has been compared with its detection using the Blitzortung.org network. It's important to note that not every lightning strike detected by the STP antenna is also detected by the Blitzortung.org network. Figure 4.26 shows that when the storm was closest to the car according to Blitzortung.org, the STP antenna detected lightning at different times or at distances of more than 120 km. Conversely, as shown in Figure 4.27, when the storm was located tens of kilometers away from the observation site according to Blitzortung.org, there is perfect conformity with the data from the STP antenna. In both figures, an interval of ± 1 second is marked around the vertical lines corresponding to the detection times.

Lightning at 18:24:48 was detected by a high-speed camera, see video [1627302288.9546976.mp4]. According to the video, one of the lightning channels occurred almost directly above the measurement car, but the nearest lightning detected by Blitzortung.org was at least 70 km away. The positioning accuracy in the case of the Blitzortung.org network is in the order of kilometers. Blitzortung.org detected discharges at a distance of 70 to 80 km simultaneously. This allows the deduction that this lightning was more than 80 km long or that a synchronous discharge occurred 80 km away.



[`figur_blitz2`]

Figure 4.26. Correlation with “nearby” (less than 20 km) lightning detection.

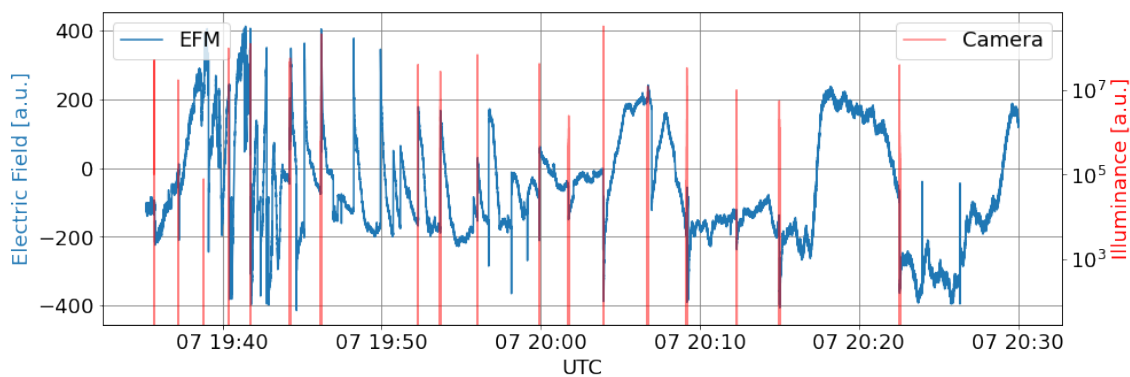


[`figur_blitz1`]

Figure 4.27. Correlation with “distant” (more than 40 km) lightning detection.

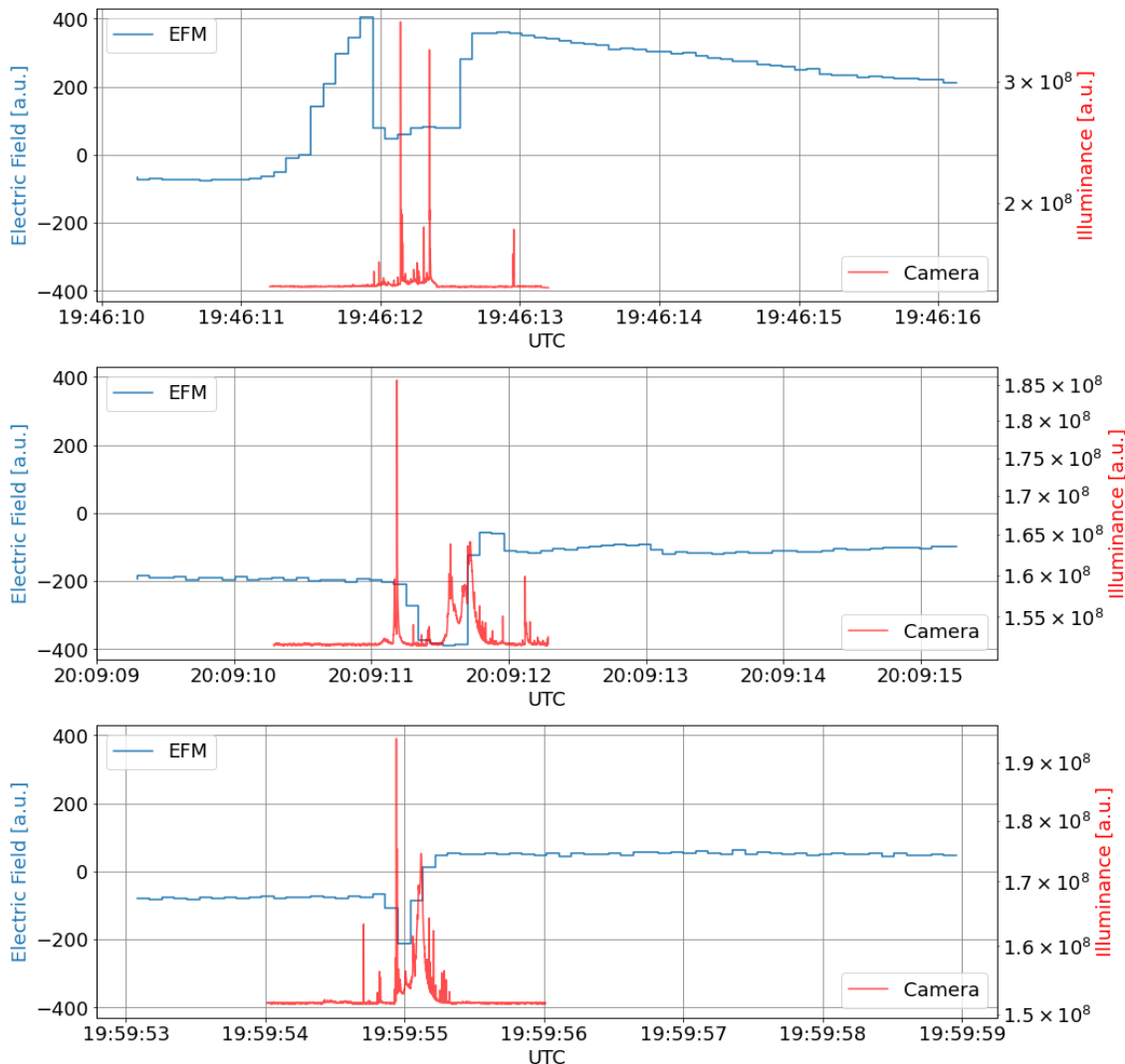
■ 4.3.7 Electric field measurements

Figures 4.28 and 4.29 compare vertical electric field measurements at the car’s measuring site with camera recordings. The Kleinwächter EFM 115 on the car is not grounded, so it measures the gradient of electric potential between the sensor and the car body. As shown in Figure 4.28, electric discharges occur during times of significant electric field changes. However, as detailed in Figure 4.29, changes in the electric field do not directly correspond to individual discharges recorded by the camera. It’s important to note that the EFM measures the vertical component of the electric field, which integrates over a large area of the cloud and is also affected by the presence of the car.



```
[figur_efmdata]
```

Figure 4.28. Example of measurement with EFM compared with records of lightning captured on the camera.



```
[figur_efmdatadetail]
```

Figure 4.29. Detail of EFM data with a comparison with camera data.

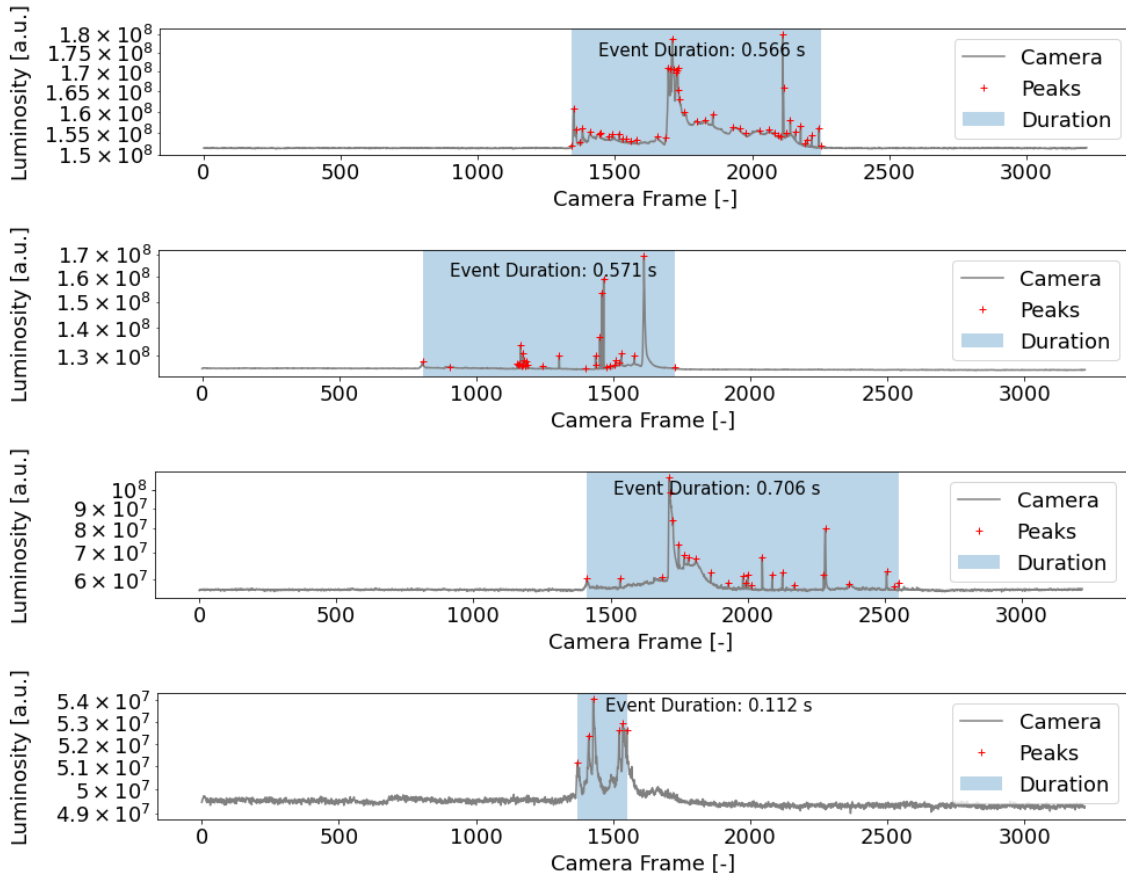
Chapter 5

Summary of results

The chapter is based on the published article: <https://amt.copernicus.org/articles/16/547/2023/> The discussed video content is also included in article assets. The following text highlights the main findings and results achieved from the date of publication.

5.1 Lightning duration

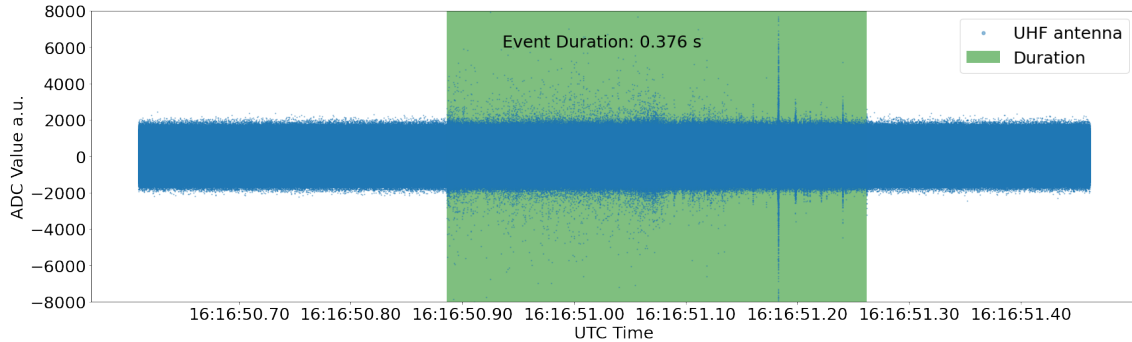
The duration of the lightning event was determined by identifying local maxima of illumination on the camera chip over time from peaks that had a prominence higher than twice the noise level. The first and last maxima were used to identify the first and last frame, and the lightning duration was calculated from the framerate. The first ten frames of the camera recording were omitted to avoid potential artifacts from video data compression. The noise amplitude was established from the first 100 frames (from frame 10 to frame 110). Examples of duration determination for some lightning events are shown in Figure 5.1. The histogram of lightning event durations, shown in Figure 5.3, includes 107 lightning events measured during 12 thunderstorms.



`_lightning_duration]`

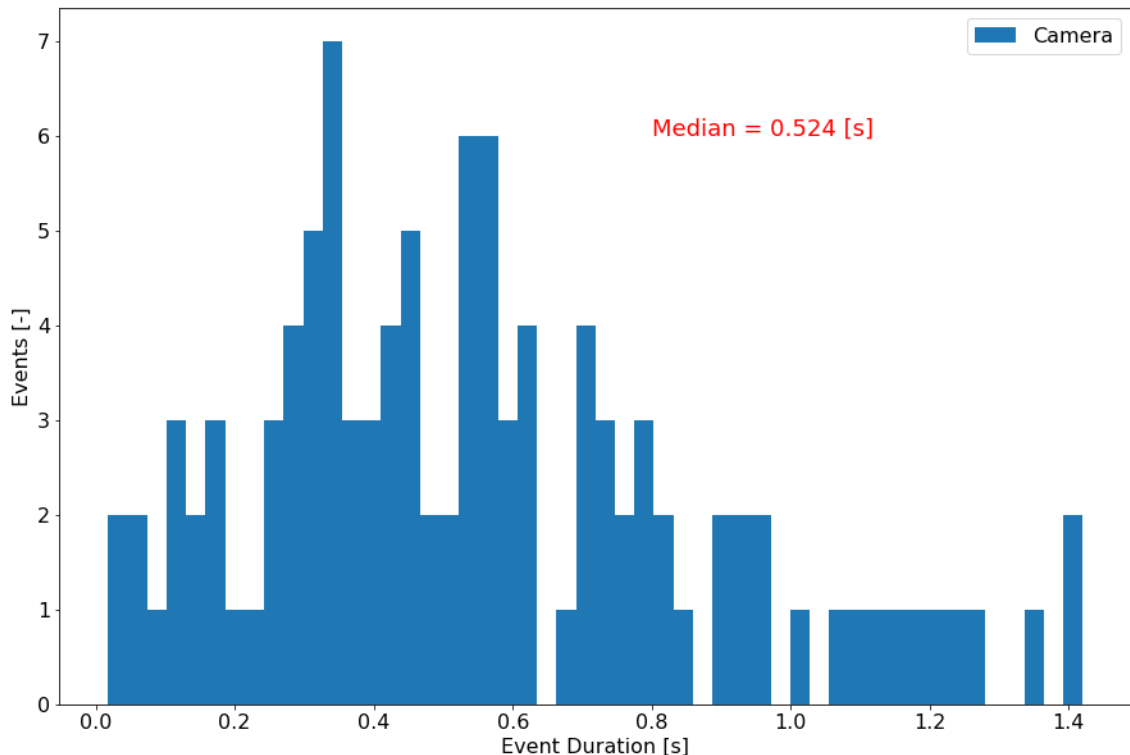
Figure 5.1. Examples of detection of lightning events duration. Red crosses are detected peaks in signals generated by lightning processes. The determined length of lightning duration is highlighted. The duration of the camera frame is 620 μ s.

To calculate the total length of a lightning event from a radio signal (see Fig. 5.2), a similar methodology was used, where a signal greater than 4σ , calculated from a moving window of 10 ms, marks the beginning of the lightning discharge. This algorithm is applied symmetrically from both ends of the recorded signal. For detecting the lightning start, the process begins from the first sample of the signal, and for detecting the lightning end, the process begins from the last sample of the recorded signal.



`_lightning_duration]`

Figure 5.2. Example of lightning duration measurement based on radio signal captured by the UHF receiver. The time duration of lightning is marked by the green overlay.



`[duration_histogram]`

Figure 5.3. Histogram of the observed duration of lightning events. The histogram is based on data captured by high-speed cameras.

The measured durations are usually in the order of hundreds of milliseconds, only exceptionally there are shorter lightning events. The median duration of lightning

events is 524 ms. This result is significantly higher than was mentioned in previous studies 200-300 ms [43] and 350 ms [96].

The processing of lightning recordings differs for day and night storm observations as they require different settings of high-speed cameras, in particular, the setting of exposition length and analog gain varies. This difference could affect the exact measurements of the total length of a discharge, resulting however only in a shortening of the estimated time duration. Because of sunlight scattered in the atmosphere during the daytime, the weak discharges might have been omitted. Therefore the extracted time durations of lightning events could be possibly underestimated. From the subsequent analysis of the lightning duration, two thunderstorms were excluded where it was not possible to distinguish individual lightning events, meaning there was no delay of at least 500 ms between the individual detected discharges. Lightning is considered to be an event where the time between the individual discharges does not exceed 100 ms.

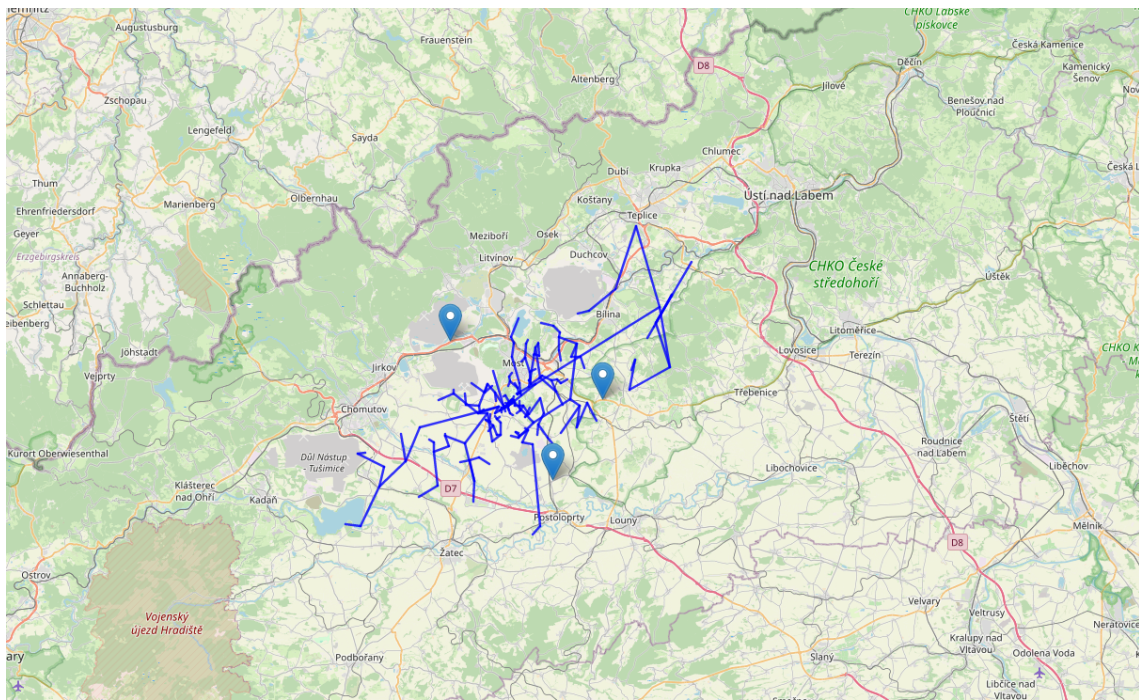
5.2 Lightning development/characterization

Data from the cameras reveal similar phases of lightning development. Examples of video recordings with individual phases visible and not obscured by clouds are provided. Video [1627302745.846055.mp4] captures (from $T=+0.27$ s (1:11) to $T=+0.40$ s (1:22)) a positive side of the leader. When the current flowing through the leader begins to weaken, recoil leaders start to appear at its end ($T=+0.38$ s (1:21)). The term recoil leader was taken from literature [97]. Based on the described observations, however, it is not confirmed that all the visible recoil leaders reuse an exactly already established ionized channel.

Video [2021-08-15-20-07-35.912167-lightning.mp4] captures an invisible positive leader, only blurred recoil leaders are visible. From $T=+0.07$ s (1:36) a negative side of the leader is visible. Negative leader branches abundantly, its propagation is faster than the positive leader and contains hot luminous ends. The second visible negative leader starts at $T=+0.25$ s (1:51). The negative leaders do not generate recoil leaders.

Based on the experience from recordings where some parts of lightning are visible, cloud-obscured lightning events can be characterized. There is an example of the luminosity curve compared to the STP antenna signal data shown in Figure 4.25. At the very beginning, the lightning usually starts with a faint peak with a fast-rising edge (at time 0.2 s). Then there is an optically dark phase with low luminosity. This dark period is not quiet in the radio signal. It is a phase of developing a leader. As the leader in the cloud connects to more and more charged regions it becomes brighter, sometimes slowly and sometimes abruptly. During and after a decrease in the current in the positive leader the recoil leaders are appearing (after time 0.4 s). Some recoil leaders have high luminosity when they connect to the main channel. In the radio spectrum, simultaneous peaks are observed that correspond to short, intense brightenings. In some cases the lightning results in CG discharge, which is accompanied by high-intensity flash (at time 0.5 s). However, this phenomenon does not occur very often. Using the described equipment, CG return strokes were registered in less than 10% of cases. The described findings have direct implications, for example, on the way lightning discharge events should be displayed and localized. Given the typical dimensions and time scales on which discharges occur, it follows that even receivers operating on the VLF principle can provide meaningful descriptions of lightning discharge structures. At the same time, for the same reason, it is misleading to display lightning discharges on maps as points, which are intuitively interpreted as CG lightning strikes hitting the

ground at approximately the position of the map mark. In reality, most of those points correspond to CC lightning discharges, given the actual incidence of their occurrence over CG lightning. A better representation that considers this fact is attempted in Fig. 5.4, which shows a calculated approximate visualization of the lightning structure. The representation is based on VLF data obtained from only three measuring stations placed on cars, so it contains many simplifications. For example, the lightning structure is depicted in a 2D plane positioned at a fixed height above the ground. Additionally, it is important to note that lightning discharges do not radiate at branching points, but primarily at the locations of two-thirds recoil leaders. The drawn connections do not reflect this fact, as the depiction is currently an illustrative algorithm that, despite its limitations, is a closer description of the physical principle of lightning discharges than the widely used depiction of points in a map.



[VLF_lightning_map]

Figure 5.4. An illustrative visualization of the structure of lightning discharges based on VLF data obtained from three measuring stations mounted on vehicles. The representation depicts the lightning structure in a 2D plane at a fixed height above the ground, capturing the approximate spatial distribution and progression of the lightning channels. The depiction emphasizes the complexity of the lightning and provides a closer representation of the physical nature of lightning discharges.

The algorithm used for computing and visualizing lightning uses VLF recordings obtained simultaneously from three measurement vehicles by the described equipment. These recordings are aligned based on absolute time marks. The data fragments are normalized and their offsets are removed. The prepared recordings are then divided into a predetermined number of segments. Segment length is not constant but is chosen so that each contains a similar amount of energy. The energy level and segmentation are algorithmically determined based on the total energy of the weakest signal. This ensures that each segment divided from the lightning signal fragment has enough significant morphological features that enable the calculation of signal shifts. TDoA values are then calculated by cross-correlating pairs of signals across the three stations. The localization algorithm utilizes segments with at least two TDoA values that match physical constraints (e.g., time shifts cannot exceed the physical distance between stations).

The navigation solution is then obtained by numerically solving the TDoA localization problem within an area situated above the plane where the stations are placed, at the expected cloud base altitude. The fragment signal processing method is selected due to the aforementioned results. Additionally, the use of cross-correlation over signal segments provides significant advantages when one of the signals (in this case, CAR1) is heavily interfered with by uncorrelated noise absent from other stations. That is a feature that cannot be applied on conventional lightning detection networks, where only individually recorded pulses are processed. The visualization is achieved through a graph algorithm that progressively adds points to the graph in a way that satisfies the geometric conditions related to lightning propagation, like utilizing adjacent lightning channels. This approach effectively eliminates the need for clustering algorithms commonly used [98] to determine the lightning strike area, as the connection between individual parts of lightning is not lost in the process. The described algorithm could be significantly improved by implementing an algorithmic estimation of the optimal number of segments based on pre-analysis of the lightning development in the signal fragment, which could be probably done by some form of identification of lightning phases in the signal. In other words, the creation of a lightning signal model which should be then matched to the real signals from different stations.

5.3 Conclusions

During multiple summer storm seasons, data on more than 100 lightning events were collected using the described measuring apparatus and methodology, which includes multiple innovations to which I contributed, namely the instrument triggering method and new sensors. Initially, the apparatus was designed to detect and localize lightning events within a spatial range of a few kilometers. However, it was discovered that the spatial extent of these phenomena (based on lightning observations) is likely tens of kilometers, rendering the initially designed apparatus inadequate. Observations made using the proposed apparatus (cameras, radio detectors) revealed that the data from all-sky high-speed cameras and magnetic or electromagnetic antennas provide comparable results in terms of lightning duration measurement. The median duration of lightning measured was significantly longer than previously stated in the literature. Furthermore, stationary ground-based electric field measurements (using field mills) did not correlate well with the manifestation of lightning discharges and provided limited information about the development of lightning, indicating that such measurements should be performed *in situ* using UAVs. The research faced significant challenges due to the primarily horizontal propagation of lightning. This suggested that the electric field and resultant RREA would also radiate horizontally, rather than vertically. This finding was supported by the failure to detect ionizing radiation from below storm clouds, while stationary detectors on elevated locations detected it even in the absence of nearby lightning. Additionally, optical and radio observations of lightning discharges demonstrated that the initiation of lightning discharges could not be confined to a short time interval around the return stroke but developed over several seconds. The return stroke, often considered a key phase, appeared to be just one of several possible phases and occasionally did not occur at all. The situation necessitated the expansion of measuring instruments to include a broader range of devices. These included stationary detectors on elevated sites and *in-situ* measurements (of electric fields and ionizing radiation) using UAVs. Initial tests with stratospheric balloons showed promise, leading to efforts to use the autogyro for controlled *in-situ* measurements, as balloons are im-

practical for stormy conditions. This required the design of a new electric field mill and a semiconductor diode-based ionizing radiation detector suitable for UAVs. The extended experiments revealed that the initiation of lightning discharges likely occurs far from where the visible discharge is observed. Despite capturing one video potentially showing the initiation phase, it has not been directly used due to the complexities in interpreting it due to missing contextual data from other instruments. Consequently, a simple correlation between ionizing radiation detection and lightning discharge is insufficient to determine causality, as the required experiment is significantly more complex and demands a much larger instrumentation coverage area or an invention of method, which allows to focus solely on the initiation phase of lightning. The current implementation of radio detection networks for lightning has proven inadequate. These networks process lightning as clusters of impulses, losing significant information in the process, and present data as **crosses on a map**, often misinterpreting them as return strokes, which were rarely actual ground strikes. The research suggests a better representation of lightning discharges, avoiding graphics that imply ground strikes and considering the physical development of lightning, especially the creation of VLF radio signals primarily emitted at segments where ionized channels reconnect (recoil leaders). Although this representation is still simplified and requires further work, it is a significant improvement over current implementations.

5.4 Future Work

Future research needs to be focused on in-situ measurements. UAVs, despite their limited success in the currently described work, appear to be ideal for this purpose. It is necessary to measure the electric field in space (ideally as a 3D vector), which an autogyro, with its rotating rotor, could facilitate. That type of in-situ measurement should also include ionizing radiation detection. The deployment of these approaches in subsequent studies is expected to yield substantial results, possibly confirming the direct detection of RREA and the directional structure of thunderstorm ionizing radiation sources. That knowledge is essential to interpret the measured ionizing radiation and lightning event data to explain lightning initiation or eventually predict lightning occurrence. The application of the TF-G2 autogyro in the described study has highlighted the potential and challenges of leveraging UAV technology for atmospheric research. The issues primarily stemmed from the software's maturity, which significantly impeded the ability to conduct successful measurements during storm activity. This aspect of technology, while a limitation in the current study, offers a critical area for improvement and optimization in future work. Enhancing the stability and reliability of UAV-related code will undoubtedly augment higher capability to collect high-fidelity atmospheric data from nearby or within storms, thereby enriching the understanding of thunderstorm dynamics, improving weather prediction models, and contributing to climate studies. Therefore continuous development and field testing of the unmanned autogyro and related technologies are required.

Appendix A

Index

ball lightning 6
cloud-to-cloud flash 7
cloud-to-ground flash 7
compact intracloud discharge 7
elves, 6
gigantic jets 6
intra-cloud discharge 6
ionizing radiation 5
K-changes, 7
lighting 4
lightning mapping 6
radio pulses 7
return stroke 7
Sferics 7
sprites, 6
terrestrial gamma-ray flash (TGF) 6
TF-ATMON 55
TF-G2 60
thunderstorm 5
— ground enhancement (TGE) 6

Appendix B

Dictionary

ADC	■ Analog-to-digital converter
CC	■ cloud-to-cloud flash
CFAR	■ Constant false alarm rate
CG	■ cloud-to-ground flash
CID	■ intracloud lightning discharge
CRREAT	■ Center of Cosmic Rays and Radiation Events in the Atmosphere
ECMWF	■ European Centre for Medium-Range Weather Forecasts
EFM	■ electric field mill
ESC	■ electronic speed control
GNSS	■ global navigation satellite system
GPS	■ Global Positioning System
I/Q	■ in-phase (I) and quadrature (Q) components
IAS	■ indicated airspeed
LCL	■ Lifting Condensation Level
LEO	■ low Earth orbit
LTE	■ long-term evolution
MIMO	■ multiple-input and multiple-output
MLAB	■ Modular Laboratory Open Hardware Project
NBE	■ Narrow Bipolar Events
PCB	■ Printed Circuits Board
PMR446	■ Private Mobile Radio, 446 MHz
PPS	■ Pulse-per-second signal
QFH	■ Quadrifilar Helix Antenna
RF	■ Radio Frequency
RPM	■ Revolutions Per Minute
RREA	■ relativistic runaway electron avalanche
RSSI	■ Received signal strength indicator
RTK	■ Real-Time Kinematic
STP	■ Shielded twisted pair
TDM	■ Time-division multiplexing
TDoA	■ Time difference of arrival
UAS	■ Unmanned Aerial Systems
UAV	■ Unmanned Aerial Vehicle
UHF	■ Ultra high frequency
VHF	■ Very high frequency
VLF	■ Very low frequency

Appendix C

FIK Flights Overview

Table 1: Table summarising success of used technologies, with colours representing a degree of reliability:

		Flight	FIK-1	FIK-2	FIK-3	FIK-4	FIK-5	FIK-6	Partial failure	Correct function
Location (year)		CZ (2015)	CZ (2017)	CZ (2018)	SE (2019)	CZ (2019)	CZ (2020)	CZ (2023)		
Payload	Candy detector, Web camera	Candy detector, Web camera	AIRDOS, 360 deg camera	AIRDOS-C CRY19, SPACEDOS, G-M, Socrat-R	AIRDOS-C CRY19, SPACEDOS, G-M, G-M, 360 deg camera	AIRDOS-C NaI(T), SPACEDOS, G-M, Ionmeter, 360 deg camera	AIRDOS-C NaI(T), SPACEDOS, G-M, Ionmeter, 360 deg camera	AIRDOS-C NaI(T), SPACEDOS, G-M, PITED, MiniPIX, TEHHD01		
Landing site	vineyard Austria	rapeseed field	Poland	swamp (Finland)		forest	railway corridor		Near high voltage substation	
Power source	Li-ion 18650 accu	Li-ion 18650 and li-pol accu	Lithium primary cells and li-pol accu SigFox, 868 MHz	Lithium primary cells	Lithium primary cells	Lithium 18650 accu	Lithium 18650 accu	Lithium 18650 accu		
Telemetry system	GSM	GSM	GSM, 868 MHz Proprietary Modem	Outsourced	Lora, SigFox, SK 433 MHz	2x LoRa, SK 433 MHz			868 MHz LoRa, SK 433 MHz	
Rescue beacon	433 MHz CW	433 MHz CW	433 MHz CW	Outsourced	433 MHz CW	433 MHz CW			433 MHz CW	
Flight control computer	Odroid-U2	Odroid-U2	Not used	Not used/ outsourced	PX4, FMU v5	PX4, FMU v5	PX4, FMU v5	PX4, FMU v5	PX4, FMU v5, TF-ATMION	

References

- [1] M. Urbani, J. Montanyà, O. A. van der Velde, J. A. López, M. Arcanjo, P. Fontanes, D. Romero, and J. A. Roncancio. High-Energy Radiation From Natural Lightning Observed in Coincidence With a VHF Broadband Interferometer. *Journal of Geophysical Research: Atmospheres*. 2021, 126 (7), e2020JD033745. DOI <https://doi.org/10.1029/2020JD033745>. e2020JD033745 2020JD033745.
- [2] Devendraa Siingh, and R. P. Singh. The role of cosmic rays in the Earth's atmospheric processes. *Pramana*. 2010, 74 (1), 153-168. DOI 10.1007/s12043-010-0017-8.
- [3] G. K. Parks, B. H. Mauk, R. Spiger, and J. Chin. X-ray enhancements detected during thunderstorm and lightning activities. *GRL*. 1981, 8 (11), 1176-1179. DOI <https://doi.org/10.1029/GL008i011p01176>.
- [4] M McCarthy, and G K Parks. Further observations of X-rays inside thunderstorms. *Geophysical Research Letters*. 1985 , 12 (6), 393-396.
- [5] Kenneth B. Eack, William H. Beasley, W. David Rust, Thomas C. Marshall, and Maribeth Stolzenburg. Initial results from simultaneous observation of X-rays and electric fields in a thunderstorm. *Journal of Geophysical Research: Atmospheres*. 1996, 101 (D23), 29637-29640. DOI <https://doi.org/10.1029/96JD01705>.
- [6] Tatsuo Torii, Minoru Takeishi, and Teruo Hosono. Observation of gamma-ray dose increase associated with winter thunderstorm and lightning activity. *Journal of Geophysical Research: Atmospheres*. 2002, 107 (D17), ACL 2-1-ACL 2-13. DOI <https://doi.org/10.1029/2001JD000938>.
- [7] Ashot Chilingarian, Ara Daryan, K. Arakelyan, A. Hovhannisanian, Bagrat Maiyan, L. Melkumyan, Gagik Hovsepyan, Suren Chilingaryan, Artur Reymers, and Levon Vanyan. Ground-based observations of thunderstorm-correlated fluxes of high-energy electrons, gamma rays, and neutrons. *Physical Review D*. 2010, 82 043009. DOI 10.1103/PhysRevD.82.043009.
- [8] Teruaki Enoto, Yuuki Wada, Yoshihiro Furuta, Kazuhiro Nakazawa, Takayuki Yuasa, Kazufumi Okuda, Kazuo Makishima, Mitsuteru Sato, Yousuke Sato, Toshio Nakano, Daigo Umemoto, and Harufumi Tsuchiya. *Photonuclear reactions triggered by lightning discharge*. 2017. <https://doi.org/10.1038/nature24630>.
- [9] Y. Wada, G. S. Bowers, T. Enoto, M. Kamogawa, Y. Nakamura, T. Morimoto, D. M. Smith, Y. Furuta, K. Nakazawa, T. Yuasa, A. Matsuki, M. Kubo, T. Tamagawa, K. Makishima, and H. Tsuchiya. Termination of Electron Acceleration in Thundercloud by Intracloud/Intercloud Discharge. *Geophysical Research Letters*. 2018, 45 (11), 5700-5707. DOI <https://doi.org/10.1029/2018GL077784>.
- [10] Ferran Fabrò, Joan Montanyà, Nicolau Pineda, Oriol Argemí, Oscar A. van der Velde, David Romero, and Serge Soula. Analysis of energetic radiation associated with thunderstorms in the Ebro delta region in Spain. *JGR*. 2016, 121 (16), 9879-9891. DOI <https://doi.org/10.1002/2015JD024573>.

- [Dwyer_2003]
- [11] J R Dwyer. A fundamental limit on electric fields in air. *Geophysical Research Letters*. 2003, 30 (20), DOI 10.1029/2003GL017781.
- [Roussel-Dupre_1992]
- [12] A V Gurevich, G M Milikh, and R Roussel-Dupre. Runaway electron mechanism of air breakdown and preconditioning during a thunderstorm. *Physics Letters A*. 1992, 165 (5–6), 463–468. DOI 10.1016/0375-9601(92)90348-P.
- [Fesas_et al._1994]
- [13] G J Fishman, P N Bhat, R Mallozzi, J M Horack, T Koshut, C Kouveliotou, G N Pendleton, C A Meegan, R B Wilson, W S Paciesas, S J Goodman, and H J Christian. Discovery of intense gamma-ray flashes of atmospheric origin.. *Science*. 1994, 264 (5163), 1313–1316. DOI 10.1126/science.264.5163.1313.
- [Chilingarian_2013]
- [14] Ashot Chilingarian. Thunderstorm Ground Enhancements (TGEs) – New High-Energy Phenomenon Originated in the Terrestrial Atmosphere. *Journal of Physics: Conference Series*. 2013, 409 (1), 012019. DOI 10.1088/1742-6596/409/1/012019.
- [Takeishi_Hosono_2002]
- [15] Tatsuo Torii, Minoru Takeishi, and Teruo Hosono. Observation of gamma-ray dose increase associated with winter thunderstorm and lightning activity. *Journal of Geophysical Research: Atmospheres*. 2002, 107 (D17), ACL 2-1-ACL 2-13. DOI 10.1029/2001JD000938.
- [Nakano_et al._2017]
- [16] Teruaki Enoto, Yuuki Wada, Yoshihiro Furuta, Kazuhiro Nakazawa, Takayuki Yuasa, Kazufumi Okuda, Kazuo Makishima, Mitsuteru Sato, Yousuke Sato, Toshio Nakano, Daigo Umemoto, and Harufumi Tsuchiya. Photonuclear reactions triggered by lightning discharge.. *Nature*. 2017, 551 (7681), 481–484. DOI 10.1038/nature24630.
- [inen_et al._2019]
- [17] N Østgaard, T Neubert, V Reglero, K Ullaland, S Yang, G Genov, M Marisaldi, A Mezentsev, P Kochkin, N Lehtinen, D Sarria, B H Qureshi, A Solberg, C Maionrana, K Albrechtsen, C Budtz-Jørgensen, I Kuvvetli, F Christiansen, O Chanrion, M Heumesser, and S Al-nussirat. First 10 months of TGF observations by ASIM. *Journal of Geophysical Research: Atmospheres*. 2019, 124 (24), 14024–14036. DOI 10.1029/2019JD031214.
- [Østgaard_2017]
- [18] Pavlo Kochkin, A P J van Deursen, M Marisaldi, A Ursi, A I de Boer, M Bardet, C Allasia, J F Boissin, F Flourens, and N Østgaard. In-Flight Observation of Gamma Ray Glows by ILDAS. *Journal of Geophysical Research: Atmospheres*. 2017, DOI 10.1002/2017JD027405.
- [McCarthy_Parks_1985]
- [19] M McCarthy, and G K Parks. Further observations of X-rays inside thunderstorms. *Geophysical Research Letters*. 1985, 12 (6), 393–396. DOI 10.1029/GL012i006p00393.
- [Spiger_Chin_1981]
- [20] G K Parks, B H Mauk, R Spiger, and J Chin. X-ray enhancements detected during thunderstorm and lightning activities. *Geophysical Research Letters*. 1981, 8 (11), 1176–1179. DOI 10.1029/GL008i011p01176.
- [Hovhannisyan_2011]
- [21] Ashot Chilingarian, Gagik Hovsepyan, and Armen Hovhannisyan. Particle bursts from thunderclouds: Natural particle accelerators above our heads. *Physical Review D*. 2011, 83 (6), 062001. DOI 10.1103/PhysRevD.83.062001.
- [Diendorfer_Rusz_2020]
- [22] J Chum, R Langer, J Baše, M Kollárik, I Strhárský, G Diendorfer, and J Rusz. Significant enhancements of secondary cosmic rays and electric field at the high mountain peak of Lomnický Štít in High Tatras during thunderstorms. *Earth, planets, and space : EPS*. 2020, 72 (1), 28. DOI 10.1186/s40623-020-01155-9.
- [Okano_et al._2009]
- [23] H Tsuchiya, T Enoto, T Torii, K Nakazawa, T Yuasa, S Torii, T Fukuyama, T Yamaguchi, H Kato, M Okano, M Takita, and K Makishima. Observation of

- [Michimoto_2007] [24] Koichiro Michimoto. Meteorological Aspects of Winter Thunderstorms along the Hokuriku Coast of Japan. *IEEJ Transactions on Power and Energy*. 2007, 127 (12), 1242–1246. DOI 10.1541/ieejpes.127.1242.
- [Hamlin_Harlin_1999] [25] W Rison, R J Thomas, P R Krehbiel, T Hamlin, and J Harlin. A GPS-based three-dimensional lightning mapping system: Initial observations in central New Mexico. *Geophysical Research Letters*. 1999, 26 (23), 3573–3576. DOI 10.1029/1999GL010856.
- [Wang_Takagi_2018] [26] Ting Wu, Daohong Wang, and Nobuyuki Takagi. Lightning mapping with an array of fast antennas. *Geophysical Research Letters*. 2018, 45 (8), 3698–3705. DOI 10.1002/2018GL077628.
- [Cheon_et al._2018] [27] R U Abbasi, T Abu-Zayyad, M Allen, E Barcikowski, J W Belz, D R Bergman, S A Blake, M Byrne, R Cady, B G Cheon, J Chiba, M Chikawa, T Fujii, M Fukushima, G Furlich, T Goto, W Hanlon, Y Hayashi, N Hayashida, K Hibino, and Z Zundel. Gamma ray showers observed at ground level in coincidence with downward lightning leaders. *Journal of Geophysical Research: Atmospheres*. 2018, 123 (13), 6864–6879. DOI 10.1029/2017JD027931.
- [2019JD031940] [28] J. W. Belz, P. R. Krehbiel, J. Remington, M. A. Stanley, R. U. Abbasi, R. LeVon, W. Rison, D. Rodeheffer, T. Abu-Zayyad, M. Allen, E. Barcikowski, D. R. Bergman, S. A. Blake, M. Byrne, R. Cady, B. G. Cheon, M. Chikawa, A. di Matteo, T. Fujii, K. Fujita, R. Fujiwara, M. Fukushima, G. Furlich, W. Hanlon, M. Hayashi, Y. Hayashi, N. Hayashida, K. Hibino, K. Honda, D. Ikeda, T. Inadomi, N. Inoue, T. Ishii, H. Ito, D. Ivanov, H. Iwakura, H. M. Jeong, S. Jeong, C. C. H. Jui, K. Kadota, F. Kakimoto, O. Kalashev, K. Kasahara, S. Kasami, H. Kawai, S. Kawakami, K. Kawata, E. Kido, H. B. Kim, J. H. Kim, J. H. Kim, V. Kuzmin†, M. Kuznetsov, Y. J. Kwon, K. H. Lee, B. Lubsandorzhiev, J. P. Lundquist, K. Machida, H. Matsumiya, J. N. Matthews, T. Matuyama, R. Mayta, M. Minamino, K. Mukai, I. Myers, S. Nagataki, K. Nakai, R. Nakamura, T. Nakamura, Y. Nakamura, T. Nonaka, H. Oda, S. Ogio, M. Ohnishi, H. Ohoka, Y. Oku, T. Okuda, Y. Omura, M. Ono, A. Oshima, S. Ozawa, I. H. Park, M. Potts, M. S. Pshirkov, D. C. Rodriguez, G. Rubtsov, D. Ryu, H. Sagawa, R. Sahara, K. Saito, Y. Saito, N. Sakaki, T. Sako, N. Sakurai, K. Sano, T. Seki, K. Sekino, F. Shibata, T. Shibata, H. Shimodaira, B. K. Shin, H. S. Shin, J. D. Smith, P. Sokolsky, N. Sone, B. T. Stokes, T. A. Stroman, Y. Takagi, Y. Takahashi, M. Takeda, R. Takeishi, A. Taketa, M. Takita, Y. Tameda, K. Tanaka, M. Tanaka, Y. Tanoue, S. B. Thomas, G. B. Thomson, P. Tinyakov, I. Tkachev, H. Tokuno, T. Tomida, S. Troitsky, Y. Tsunesada, Y. Uchihori, S. Udo, T. Uehama, F. Urban, M. Wallace, T. Wong, M. Yamamoto, H. Yamaoka, K. Yamazaki, K. Yashiro, M. Yosei, H. Yoshii, Y. Zhezher, and Z. Zundel. Observations of the Origin of Downward Terrestrial Gamma-Ray Flashes. *Journal of Geophysical Research: Atmospheres*. 2020, 125 (23), e2019JD031940. DOI <https://doi.org/10.1029/2019JD031940>. e2019JD031940 10.1029/2019JD031940.
- [2021JD036130] [29] I. Kereszy, V. A. Rakov, Z. Ding, and J. R. Dwyer. Ground-Based Observation of a TGF Occurring Between Opposite Polarity Strokes of a Bipolar Cloud-To-Ground Lightning Flash. *Journal of Geophysical Research: Atmospheres*. 2022, 127

- (9), e2021JD036130. DOI <https://doi.org/10.1029/2021JD036130>. e2021JD036130
 [2012JA017810] [30] J. R. Dwyer, M. M. Schaal, E. Cramer, S. Arabshahi, N. Liu, H. K. Rassoul, J. D. Hill, D. M. Jordan, and M. A. Uman. Observation of a gamma-ray flash at ground level in association with a cloud-to-ground lightning return stroke. *Journal of Geophysical Research: Space Physics*. 2012, 117 (A10), DOI <https://doi.org/10.1029/2012JA017810>.
- [123061103] [31] Y. Wada, T. Enoto, K. Nakazawa, Y. Furuta, T. Yuasa, Y. Nakamura, T. Morimoto, T. Matsumoto, K. Makishima, and H. Tsuchiya. Downward Terrestrial Gamma-Ray Flash Observed in a Winter Thunderstorm. *Phys. Rev. Lett.* 2019, 123 061103. DOI 10.1103/PhysRevLett.123.061103.
- [7180031] [32] Umran İnan. *Lightning-driven phenomena in near-earth space*. In: *2015 IEEE International Conference on Plasma Sciences (ICOPS)*. 2015. 1-1.
- [Rakov_2016] [33] Vladimir A. Rakov. *Types of lightning discharges and lightning terminology*. In: *Fundamentals of Lightning*. Cambridge University Press, 2016. 1–16.
- [mehranzamir2014] [34] Kamyar Mehranzamir, Zulkurnain Abdul-Malek, Behnam Salimi, and Noor Azlinda Ahmad. *Observation of Isolated Breakdown Lightning Flashes in a Tropical Region*. In: *Mechanical and Materials Engineering*. Trans Tech Publications Ltd, 2014. 583–587.
- 0780470030875.ch6] [35] Curious lightning phenomena. In: *Understanding Lightning and Lightning Protection*. John Wiley & Sons, Ltd, 2006. 6. ISBN 9780470030875.
<https://onlinelibrary.wiley.com/doi/abs/10.1002/9780470030875.ch6>.
- raud:hal-01386421] [36] J.-F Ribaud, Olivier Bousquet, and S Coquillat. Relationships between total lightning activity, microphysics and kinematics during the 24 September 2012 HyMeX bow-echo system. *Quarterly Journal of the Royal Meteorological Society*. 2016, 142 298 - 309. DOI 10.1002/qj.2756.
- /JC080i027p03801] [37] E. Philip Krider, George J. Radda, and R. Carl Noggle. Regular radiation field pulses produced by intracloud lightning discharges. *Journal of Geophysical Research (1896-1977)*. 1975, 80 (27), 3801-3804. DOI <https://doi.org/10.1029/JC080i027p03801>.
- [5184875] [38] Amitabh Nag, and Vladimir A. Rakov. Electromagnetic Pulses Produced by Bouncing-Wave-Type Lightning Discharges. *IEEE Transactions on Electromagnetic Compatibility*. 2009, 51 (3), 466-470. DOI 10.1109/TEMC.2009.2025495.
- 029/2003JD003936] [39] Abram R. Jacobson. How do the strongest radio pulses from thunderstorms relate to lightning flashes?. *Journal of Geophysical Research: Atmospheres*. 2003, 108 (D24), DOI <https://doi.org/10.1029/2003JD003936>.
- 029/1998RS900043] [40] Abram R. Jacobson, Stephen O. Knox, Robert Franz, and Donald C. Enemark. FORTE observations of lightning radio-frequency signatures: Capabilities and basic results. *Radio Science*. 1999, 34 (2), 337-354. DOI <https://doi.org/10.1029/1998RS900043>.
- [LeVine1978TheTS] [41] David M. LeVine. *The temporal structure of RF radiation from lightning*. In: 1978. <https://api.semanticscholar.org/CorpusID:108486298>.
- [Nanayakkara] [42] Sankha Nanayakkara, Mahendra Fernando, and Vernon Cooray. Features of K-Changes Observed in Sri Lanka in the Tropics. *Atmosphere*. 2019, 10 141. DOI 10.3390/atmos10030141.

- [rakov_uman_2003]
- [u2012DischargeH0]
- [Koochak]
- [npg-20-293-2013]
- [2021GeomagneticPB]
- [Hess:1912srp]
- [REGENER1935]
- [e09-da46857c3d48]
- [029/2006JD008187]
- [CHANG2020126867]
- [Fabry_2015]
- [029/2018JA025622]
- [2b264b47fd73da169]
- [Amman1970]
- [5173582]
- [43] Vladimir A. Rakov, and Martin A. Uman. *Lightning: Physics and Effects*. Cambridge University Press, 2003.
- [44] Ting Wu, Wan-sheng Dong, Yijun Zhang, Tsuyoshi Funaki, Satoru Yoshida, Takeshi Morimoto, Tomoo Ushio, and Zen-ichiro Kawasaki. Discharge height of lightning narrow bipolar events. *Journal of Geophysical Research*. 2012, 117
- [45] Zahra Koochak, and Antony Fraser-Smith. Single-Station Lightning Location Using Azimuth and Time of Arrival of Sferics. *Radio Science*. 2020, 55 DOI 10.1029/2018RS006627.
- [46] S. N. Artekha, and A. V. Belyan. On the role of electromagnetic phenomena in some atmospheric processes. *Nonlinear Processes in Geophysics*. 2013, 20 (3), 293–304. DOI 10.5194/npg-20-293-2013.
- [47] Vladimir A. Parkhomov, Aleksandr Mikhalev, and Konstantin Ratovskyi. Geomagnetic Pulsations, Blackout and Low-Latitude Aurorae Associated with Power Magnetic Storm. *System Analysis & Mathematical Modeling*. 2021,
- [48] Victor F. Hess. Über Beobachtungen der durchdringenden Strahlung bei sieben Freiballonfahrten. *Phys. Z.* 1912, 13 1084–1091.
- [49] ERICH REGENER, and GEORG PFOTZER. Vertical Intensity of Cosmic Rays by Threefold Coincidences in the Stratosphere. *Nature*. 1935, 136 (3444), 718-719. DOI 10.1038/136718a0.
- [50] Athelstan F. Spilhaus. Progress in Meteorological Instrumentation, 1920–1950. *Bulletin of the American Meteorological Society*. 1950, 31 (10), 358–364.
- [51] William W. Hager, Richard G. Sonnenfeld, Beyza Caliskan Aslan, Gaopeng Lu, William P. Winn, and William L. Boeck. Analysis of charge transport during lightning using balloon-borne electric field sensors and Lightning Mapping Array. *Journal of Geophysical Research: Atmospheres*. 2007, 112 (D18), DOI https://doi.org/10.1029/2006JD008187.
- [52] Chih-Chung Chang, Chih-Yuan Chang, Jia-Lin Wang, Xiang-Xu Pan, Yen-Chen Chen, and Yu-Jui Ho. An optimized multicopter UAV sounding technique (MUST) for probing comprehensive atmospheric variables. *Chemosphere*. 2020, 254 126867. DOI https://doi.org/10.1016/j.chemosphere.2020.126867.
- [53] Frédéric Fabry. *Meteorology and radar*. In: *Radar Meteorology: Principles and Practice*. Cambridge University Press, 2015. 1–7.
- [54] N. G. Mazur, E. N. Fedorov, V. A. Pilipenko, and V. V. Vakhnina. ULF Electromagnetic Field in the Upper Ionosphere Excited by Lightning. *Journal of Geophysical Research: Space Physics*. 2018, 123 (8), 6692-6702. DOI https://doi.org/10.1029/2018JA025622.
- [55] Gia Trinh, Olaf Scholten, Stijn Builtink, Antonio Bonardi, Arthur Corstanje, Ute Ebert, Emilo Enriquez, Heino Falcke, Jörg Hörandel, Pragati Mitra, Katie Mulrey, Anna Nelles, Jörg Rachen, Laura Rossetto, Casper Rutjes, Pim Schellart, Satyendra Thoudam, Sander ter Veen, and Tobias Winchen. A non-intrusive method to determine atmospheric electric fields under thunderstorm conditions.. *EGU General Assembly*. 2017, 19 5013. 19th EGU General Assembly, EGU2017 ; Conference date: 23-04-2017 Through 28-04-2017.
- [56] Ernest A. Amman. *THE PROBLEM OF LIGHTNING AND STATIC ELECTRICITY AT THE KENNEDY SPACE CENTER*. SAE International.
- [57] Kenneth L. Cummins, and Martin J. Murphy. An Overview of Lightning Locating Systems: History, Techniques, and Data Uses, With an In-Depth Look at the

- 002/2016JD025159] U.S. NLDN. *IEEE Transactions on Electromagnetic Compatibility*. 2009, 51 (3), 499-518. DOI 10.1109/TEMC.2009.2023450.
- [58] Vanna C. Chmielewski, and Eric C. Bruning. Lightning Mapping Array flash detection performance with variable receiver thresholds. *Journal of Geophysical Research: Atmospheres*. 2016, 121 (14), 8600-8614. DOI <https://doi.org/10.1002/2016JD025159>.
- 002/2018GL077628] [59] Ting Wu, Daohong Wang, and Nobuyuki Takagi. Lightning Mapping With an Array of Fast Antennas. *Geophysical Research Letters*. 2018, 45 (8), 3698-3705. DOI <https://doi.org/10.1002/2018GL077628>.
- [Blitzortung.org] [60] Egon Wanke. *Blitzortung.org - A low cost Time of Arrival Lightning Detection and Lightning Location Network*. 2011. Accessed 19 February 2022, https://www.blitzortung.org/Documents/TOA_Blitzortung.pdf.
- 002/2017JD028132] [61] B. M. Hare, O. Scholten, A. Bonardi, S. Buitink, A. Corstanje, U. Ebert, H. Falcke, J. R. Hörandel, H. Leijnse, P. Mitra, K. Mulrey, A. Nelles, J. P. Rachen, L. Rossetto, C. Rutjes, P. Schellart, S. Thoudam, T. N. G. Trinh, S. ter Veen, and T. Winchen. LOFAR Lightning Imaging: Mapping Lightning With Nanosecond Precision. *Journal of Geophysical Research: Atmospheres*. 2018, 123 (5), 2861-2876. DOI <https://doi.org/10.1002/2017JD028132>.
- [vaisala] [62] Kenneth L. Cummins, Noriyasu Honma, Albert E. Pifer, Tim Rogers, and Masa-taka Tatsumi. Improved Detection of Winter Lightning in the Tohoku Region of Japan using Vaisala LS700x Technology. *IEEJ Transactions on Power and Energy*. 2012, 132 (6), 529-535. DOI 10.1541/ieejpes.132.529.
- 029/2021RS007293] [63] Abram R. Jacobson, Robert H. Holzworth, and James B. Brundell. Using the World Wide Lightning Location Network (WWLLN) to Study Very Low Frequency Transmission in the Earth-Ionosphere Waveguide: 1. Comparison With a Full-Wave Model. *Radio Science*. 2021, 56 (7), e2021RS007293. DOI <https://doi.org/10.1029/2021RS007293> e2021RS007293 2021RS007293.
- [Betz2009] [64] Hans D. Betz, Kersten Schmidt, and Wolf P. Oettinger. *LINET – An International VLF/LF Lightning Detection Network in Europe*. In: Hans Dieter Betz, Ulrich Schumann, and Pierre Laroche, eds. *Lightning: Principles, Instruments and Applications: Review of Modern Lightning Research*. Dordrecht: Springer Netherlands, 2009. 115–140. ISBN 978-1-4020-9079-0.
https://doi.org/10.1007/978-1-4020-9079-0_5.
- Nov2013AnalysisOB] [65] Ivana Kolmašová. *Analysis of Broadband Electric and Magnetic Signals Radiated from Lightning Discharges*. 2013.
https://dspace.cvut.cz/bitstream/handle/10467/20086/Disertace_Kolmasova_2013.pdf.
- [Blitzortung] [66] and Tobias Volgnandt Egon Wanke, Richo Andersen. *A World-Wide Low-Cost Community-Based Time-of-Arrival Lightning Detection and Lightning Location Network*. 2022. Accessed 19 February 2022,
https://docs.google.com/document/u/1/d/1KzPZJW0ErInFtfTCmhNhS2T0pg6N2bgZDyIxkh_DRVs/pub.
- [5689931] [67] Haiming Du, Hong Ma, and Yufeng Zhang. *A novel algorithm for real-time adaptive signal detection in lightning location system*. In: *The 2nd International Conference on Information Science and Engineering*. 2010. 1-4.
- [LIGHTNING01A] [68] MLAB.cz. *Coincidences calculation*. 2022. Accessed 19 February 2022,
<https://www.mlab.cz/module/LIGHTNING01A>.

- [as3935_datasheet] [69] ams AG. *AS3935 Franklin Lightning Sensor IC*. 2017. https://www.mouser.com/datasheet/2/588/AS3935_Datasheet_v4-1214699.pdf. Accessed: 2024-06-27.
- [DATALOGGER01A] [70] MLAB.cz. *DATALOGGER01A - Universal data logger to SDcard*. 2022. Accessed 19 February 2022, <https://www.mlab.cz/module/DATALOGGER01A>.
- [DIVISEK01] [71] Department of Radiation Dosimetry of the Nuclear Physics Institute of the Czech Academy of Sciences. *DIVISEK01A Lightning detector*. 2022. Accessed 19 February 2022, <https://github.com/ODZ-UJF-AV-CR/DIVISEK01>.
- [GPS01B] [72] MLAB.cz. *uBlox LEA-6 GNSS receiver module*. 2022. Accessed 19 February 2022, <https://www.mlab.cz/module/GPS01B>.
- [ALTIMET01A] [73] MLAB.cz. *Digital pressure and altimeter sensor*. 2022. Accessed 19 February 2022, <https://www.mlab.cz/module/ALTIMET01A>.
- [EarthGeometries] [74] W. J. Koshak, and R. J. Solakiewicz. *TOA Lightning Location Retrieval on Spherical and Oblate Spheroidal Earth Geometries*. 2001. https://journals.ametsoc.org/view/journals/atot/18/2/1520-0426_2001_018_0187_tllros_2_0_co_2.xml.
- [TOGA] [75] Richard L Dowden, James B Brundell, and Craig J Rodger. VLF lightning location by time of group arrival (TOGA) at multiple sites. *Journal of Atmospheric and Solar-Terrestrial Physics*. 2002, 64 (7), 817-830. DOI [https://doi.org/10.1016/S1364-6826\(02\)00085-8](https://doi.org/10.1016/S1364-6826(02)00085-8).
- [Coincidences] [76] Department of Radiation Dosimetry of the Nuclear Physics Institute of the Czech Academy of Sciences. *Coincidences calculation*. 2022. Accessed 19 February 2022, <https://github.com/ODZ-UJF-AV-CR/DIVISEK01/blob/DIVISEK01A/doc/publication/notebooks/coincidences.ipynb>.
- [Donges2016] [77] J. F. Donges, C.-F. Schleussner, J. F. Siegmund, and R. V. Donner. Event coincidence analysis for quantifying statistical interrelationships between event time series. *The European Physical Journal Special Topics*. 2016, 225 (3), 471-487. DOI [10.1140/epjst/e2015-50233-y](https://doi.org/10.1140/epjst/e2015-50233-y).
- [ortung_evaluation] [78] Adam Bergman. *Utvärdering av Blitzortung blixtnkaliseringssystem: En jämförande studie med SMHI som referenssystem*. 2017. Accessed 19 February 2022, <https://uu.diva-portal.org/smash/get/diva2:1109633/FULLTEXT01.pdf>.
- [AS3935_datasheet] [79] Austria Micro Systems. *AS3935 Datasheet Franklin Lightning Sensor IC*. 2022. Accessed 19 February 2022, <https://www.sciosense.com/wp-content/uploads/documents/AS3935-Data-Sheet.pdf>.
- [chronos_datasheet] [80] KronTechInc. *CHRONOS 1.4 DATASHEET*. 2021. Accessed 13 April 2022, <https://www.krontech.ca/wp-content/uploads/2021/09/FM-ENGR-50001-Chronos-1.4-Datasheet-Rev5.pdf>.
- [camera_lenses] [81] Fujifilm. *FE185 Series, Super wide-angle lenses*. 2021. Accessed 13 April 2022, <https://www.fujifilm.com/us/en/business/optical-devices/machine-vision-lens/fe185-series>.
- /JC086iC08p07451] [82] Craig O. Hayenga, and James W. Warwick. Two-dimensional interferometric positions of VHF lightning sources. *Journal of Geophysical Research: Oceans*. 1981, 86 (C8), 7451-7462. DOI <https://doi.org/10.1029/JC086iC08p07451>.

- [rs13224658] [83] Fengquan Li, Zhuling Sun, Mingyuan Liu, Shanfeng Yuan, Lei Wei, Chunfa Sun, Huimin Lyu, Kexin Zhu, and Guoying Tang. A New Hybrid Algorithm to Image Lightning Channels Combining the Time Difference of Arrival Technique and Electromagnetic Time Reversal Technique. *Remote Sensing*. 2021, 13 (22), DOI 10.3390/rs13224658.
- [9226420] [84] Ammar Alammari, Ammar Ahmed Alkahtani, Mohd Riduan Ahmad, Fuad M. Noman, Mona Riza Mohd Esa, Zen Kawasaki, and Sieh Kiong Tiong. Lightning Mapping: Techniques, Challenges, and Opportunities. *IEEE Access*. 2020, 8 190064-190082. DOI 10.1109/ACCESS.2020.3031810.
- [9226420] [85] Olena Velychko, Martin Kákona, Iva Ambrožová, and Ondřej Ploc. Characterization of AIRDOS-C detector for measurement of high-energy events in the atmosphere. 2021,
- [nals.rpd.a081837] [86] G. Reitz. Radiation Environment in the Stratosphere. *Radiation Protection Dosimetry*. 1993, 48 (1), 5-20. DOI 10.1093/oxfordjournals.rpd.a081837.
- [1093/rpd/ncac106] [87] Martin Kákona, Iva Ambrožová, Konstantin O Inozemtsev, Ondřej Ploc, Raisa V Tolocheck, Lembit Sihver, Olena Velychko, Jan Chroust, Hisashi Kitamura, Satoshi Kodaira, and Vyacheslav A Shurshakov. SPACEDOS: AN OPEN-SOURCE PIN DIODE DOSEMETER FOR APPLICATIONS IN SPACE. *Radiation Protection Dosimetry*. 2022, 198 (9-11), 611-616. DOI 10.1093/rpd/ncac106.
- [1093/rpd/ncac105] [88] Olena Velychko, Iva Ambrožová, Martin Kákona, and Ondřej Ploc. CHARACTERISATION OF AIRDOS-C DETECTOR FOR MEASUREMENT OF HIGH-ENERGY EVENTS IN THE ATMOSPHERE. *Radiation Protection Dosimetry*. 2022, 198 (9-11), 604-610. DOI 10.1093/rpd/ncac105.
- [atmosphere_1976] [89] National Oceanic and Atmospheric Administration and National Aeronautics and SpaceAdministration. *U.S. Standard Atmosphere, 1976*. . NASA.
- [029/2006JD007242] [90] Richard G. Sonnenfeld, John D. Battles, Gaopeng Lu, and William P. Winn. Comparing E field changes aloft to lightning mapping data. *Journal of Geophysical Research: Atmospheres*. 2006, 111 (D20), DOI <https://doi.org/10.1029/2006JD007242>.
- [htningExperiment] [91] Donald R. MacGorman, W. David Rust, Terry J. Schuur, Michael I. Biggerstaff, Jerry M. Straka, Conrad L. Ziegler, Edward R. Mansell, Eric C. Bruning, Kristin M. Kuhlman, Nicole R. Lund, Nicholas S. Biermann, Clark Payne, Larry D. Carey, Paul R. Krehbiel, William Rison, Kenneth B. Eack, and William H. Beasley. *TELEX The Thunderstorm Electrification and Lightning Experiment*. 2008. https://journals.ametsoc.org/view/journals/bams/89/7/2007bams2352_1.xml.
- [osphericResearch] [92] S. Businger, R. Johnson, and R. Talbot. *Scientific Insights from Four Generations of Lagrangian Smart Balloons in Atmospheric Research*. 2006. <https://journals.ametsoc.org/view/journals/bams/87/11/bams-87-11-1539.xml>.
- [ideThunderstorms] [93] Monte G. Bateman, W. David Rust, and Thomas C. Marshall. *A Balloon-Borne Instrument for Measuring the Charge and Size of Precipitation Particles inside Thunderstorms*. 1994. https://journals.ametsoc.org/view/journals/atot/11/1/1520-0426_1994_011_0161_abbfm_2_0_co_2.xml.
- [7735367] [94] Ilya E. Kuznetsov, Mikhail E. Semenov, Olesya I. Kanishcheva, and Peter A. Meleshenko. *On the interaction of electromagnetic waves with charged aerosol par-*

-
- ticles in atmosphere.* In: *2016 Progress in Electromagnetic Research Symposium (PIERS)*. 2016. 3542-3545.
- [windy] [95] SE Windyty. 2021. Accessed 13 April 2022,
<https://www.windy.com/>.
- [abró_Romero_2017] [96] Jesús A. López, Nicolau Pineda, Joan Montanyà, Oscar van der Velde, Ferran Fabró, and David Romero. Spatio-temporal dimension of lightning flashes based on three-dimensional Lightning Mapping Array. *Atmospheric research*. 2017, 197 255–264. DOI 10.1016/j.atmosres.2017.06.030.
- [MAZUR2013763] [97] Vladislav Mazur, Lothar H. Ruhnke, Tom. A. Warner, and Richard E. Orville. Recoil leader formation and development. *Journal of Electrostatics*. 2013, 71 (4), 763-768. DOI <https://doi.org/10.1016/j.elstat.2013.05.001>.
- [Sibolla2021] [98] Bolelang H. Sibolla, Terence Van Zyl, and Serena Coetzee. Determining Real-Time Patterns of Lightning Strikes from Sensor Observations. *Journal of Geovisualization and Spatial Analysis*. 2021, 5 (1), 4. DOI 10.1007/s41651-020-00070-7.

Requests for correction

- [rfc-1] Aktualizovat obrázek auta
- [rfc-2] TODO: vložit přílohu s blokovým schématem přijímače